

The Pennsylvania State University

The Graduate School

College of Engineering

**MICROFLUIDICS MEETS NANOMATERIALS SYNTHESIS**

A Dissertation in

Engineering Science and Mechanics

by

Mengqian Lu

© 2014 Mengqian Lu

Submitted in Partial Fulfillment  
of the Requirements  
for the Degree of

Doctor of Philosophy

May 2014

The dissertation of Mengqian Lu was reviewed and approved\* by the following:

Tony Jun Huang  
Professor of Engineering Science and Mechanics  
Dissertation Advisor  
Chair of Committee

Akhlesh Lakhtakia  
Charles Godfrey Binder Professor of Engineering Science and Mechanics

Jian Xu  
Associate Professor of Engineering Science & Mechanics and Adjunct Professor of  
Electrical Engineering

Iam-Choon Khoo  
William E. Leonhard Professor of Electrical Engineering

Judith A. Todd  
P. B. Breneman Head of the Department of Engineering Science and Mechanics

\*Signatures are on file in the Graduate School

## ABSTRACT

Nanomaterials and their applications have attracted great research interest in recent years. As the sizes of materials decrease to sub-micrometers, the intrinsic properties of the nanomaterials become different from those of bulk materials. Since the intrinsic properties of nanomaterials are strongly influenced by the elemental composition, size and shape, it is of great importance to synthesize nanomaterials with controlled reaction conditions (*e.g.*, pressure, temperature, reagent ratio) to achieve high uniformity and reproducibility of the synthesized nanomaterials.

It is difficult to achieve homogeneous chemical environment during the conventional chemical synthesis process, where the reagents are mixed at millimeter- or centimeter-scale. Microfluidic reactors, which confine the reaction volume to nanoliter or even picoliter size, have attracted a lot of research interests due to their potential in high-quality nanomaterials synthesis. However, broad distributions of the size and composition of the synthesized nanomaterials still exist within simple microfluidic reactors.

In this dissertation, the hypothesis is that diffusion-limit reactions occur within microfluidic reactors, and by improving the mixing efficiency within microfluidic reactors, the quality (*e.g.*, uniformity and performance) of the synthesized nanomaterials can be improved significantly. Furthermore, by controlling the mixing process precisely, the properties (*e.g.*, shape and size) of the synthesized nanomaterials can be finely tuned. To prove this hypothesis, I used microfluidic reactors with designs to improve mixing performance to synthesize polymer-DNA nanocomplexes (polyplexes) and organic-metal hybrid nanomaterials. One design is the acoustic-assisted bubble based microfluidic reactor, which can enhance the mixing performance by random advection within the whole microfluidic channel. The other design used here is the acoustic-assisted three-dimensional hydrodynamic focusing reactor, which can enhance mixing by reducing the

diffusion distance. Both of the designs can synthesize polyplexes with improved uniformity and biological performance compared to bulk mixing samples. Moreover, the three-dimensional hydrodynamic focusing method also shows ability to control over the local chemical ratio within the reaction zone. This property is demonstrated by the shape tunable synthesis of organic-metal hybrid nanomaterials.

## NONTECHNICAL ABSTRACT

Nanomaterials and their applications have attracted great research interest in recent years. As the sizes of materials decrease to sub-micrometers, the intrinsic properties of the nanomaterials become different from those of bulk materials. For example, the optical absorption properties of gold and silver nanomaterials depend on their sizes and shapes. The conductivity behavior of conductive nano organic polymers can be affected by the elemental composition and morphology of the polymer. Drug particles at the size of nanometers have shown better bioavailability compared to drug particles of larger sizes. Due to their special properties, nanomaterials have been applied to different fields. Inorganic nanomaterials, such as novel metal nanostructures, have been studied intensively due to their applications in imaging and sensing. Organic nanomaterials such as polymeric nanoparticles have been developed as safe and efficient carriers for gene delivery. Since the intrinsic properties of nanomaterials are strongly influenced by the elemental composition, size and shape, it is of great importance to synthesize nanomaterials with controlled reaction conditions (*e.g.*, pressure, temperature, reagent ratio) to achieve high uniformity, reproducibility and precise control over composition, size and shape.

There are two general approaches, the “top-down” and the “bottom-up” approaches, to synthesize nanomaterials. The “top-down” methods require high energy input and relatively large amount of raw materials, while the fabricated nanomaterials suffer from issues such as broad size distribution and contamination. The “bottom-up” methods provide better control during the synthesis process compared to the “top-down” method. However, it is still difficult to achieve homogeneous chemical environment during the conventional “bottom-up” synthesis process, due to the macro size of the reaction volumes. The macro sized reaction volume requires long mixing time, during which reaction already takes place. As a result, the reaction happens in heterogeneous

chemical environment, resulting in broad distribution and non-reproducibility of the synthesized products. Microfluidic reactors, which confine the reaction volume to nanoliter or even picoliter size, have attracted a lot of research interests due to their potential in high-quality nanomaterials synthesis. However, broad distributions of the size and composition of the synthesized nanomaterials still exist within simple microfluidic reactors consisting straight channels, probably due to the problem of slow mixing in laminar flow regime within microfluidic reactors.

In this dissertation, the hypothesis is that diffusion-limit reactions occur within microfluidic reactors, and by improving the mixing efficiency within microfluidic reactors, the quality (*e.g.*, uniformity and performance) of the synthesized nanomaterials can be improved significantly. Furthermore, by controlling the mixing process precisely, the properties (*e.g.*, shape and size) of the synthesized nanomaterials can be finely tuned. To prove the hypothesis, I used microfluidic reactors with designs to improve mixing performance to synthesize polymer-DNA nanocomplexes (polyplexes) and organic-metal hybrid nanomaterials. One design is the acoustic-assisted bubble based microfluidic mixer, which can enhance the mixing performance by random advection within the whole microfluidic channel. The other design used here is the acoustic-assisted three-dimensional hydrodynamic focusing device, which can enhance mixing by reducing the diffusion distance. Both designs can synthesize polyplexes with improved uniformity and biological performance compared to bulk mixing samples. Moreover, the three-dimensional hydrodynamic focusing method also shows ability to control over the local chemical ratio within the reaction zone. This property is demonstrated by the shape tunable synthesis of organic-metal hybrid nanomaterials.

## TABLE OF CONTENTS

List of Figures .....	x
List of Tables .....	xv
Acknowledgements.....	xvi
Chapter 1 Introduction .....	1
1.1 Nanomaterials .....	1
1.2 Fabrication of Nanomaterials.....	2
1.3 Microfluidic Reactors.....	3
1.4 Microfluidic Flows.....	4
1.4.1 Laminar Flow .....	4
1.4.2 Parabolic Velocity Distribution.....	5
1.5 Challenges for Microfluidics-Based Synthesis .....	6
1.6 Research Objective .....	6
1.7 Organization of Dissertation .....	8
References.....	9
Chapter 2 Microfluidic Mixers .....	11
2.1 Introduction.....	11
2.2 Overview of Microfluidic Mixing Strategies .....	12
2.2.1 Active Microfluidic Mixing .....	12
2.2.2 Passive Microfluidic Mixing .....	14
2.3 Designs of Microfluidic Reactors for Nanomaterials Synthesis .....	16
References.....	19
Chapter 3 An Acoustic-Assisted Bubble Based Microfluidic Reactor for Polyplex Synthesis .....	23
3.1 Introduction.....	23
3.2 Materials and Methods.....	26
3.2.1 Device Fabrication .....	26
3.2.2 Materials.....	27
3.2.3 Polyplexes Synthesis in the Microfluidic Reactor.....	28
3.2.4 Polyplexes Synthesis by Bulk Mixing Method .....	28
3.2.5 Cell Culture .....	28
3.2.6 Transfection.....	29
3.2.7 Characterization .....	29
3.3 Results and Discussion.....	30
3.3.1 Optimization of Operation Parameters.....	30
3.3.2 Size Distribution.....	31
3.3.3 Aggregation Kinetic Studies .....	32

3.3.4 Biological Performance of the Synthesized Polyplexes .....	33
3.4 Conclusion .....	35
References .....	37
Chapter 4 A Three-Dimensional Hydrodynamic Focusing Method for Polyplex Synthesis <sup>†</sup> .....	42
4.1 Introduction .....	42
4.2 Materials and Methods .....	45
4.2.1 Polyplexes Synthesis in the 3D-HF Microfluidic Reactor .....	45
4.2.2 Computational Simulation .....	46
4.3 Results and Discussion .....	46
4.3.1 Optimization of Operation Parameters .....	46
4.3.2 Reducing Polyplex Size by 3D-HF and Acoustic Perturbation .....	48
4.3.3 Aggregation Kinetic Studies .....	48
4.3.4 Estimation of Shear Rate and Temperature Increment .....	49
4.3.5 Biological Performance of the Synthesized Polyplexes .....	53
4.4 Conclusion .....	55
References .....	57
Chapter 5 Shape Tunable Synthesis of Hybrid Nanomaterials by Three Dimensional Hydrodynamic Focusing Method .....	61
5.1 Introduction .....	62
5.2 Materials and Methods .....	64
5.2.1 Materials .....	64
5.2.2 Synthesis of TTF-Au Hybrid Materials in 3D-HF Microfluidic Reactors .....	65
5.2.3 Synthesis of TTF-Au Hybrid Materials by Bulk Mixing Method .....	65
5.2.4 Computational Simulation .....	66
5.2.5 Characterization of the Synthesized Materials .....	66
5.3 Results and Discussion .....	66
5.3.1 Different Morphologies of TTF-Au Materials Prepared by 3D-HF method .....	66
5.3.2 Possible Mechanism of Morphology Variation .....	69
5.3.3 Mechanism of Structure Formation .....	72
5.3.4 Optical Properties of the Resultant Solutions .....	74
5.3.5 Examination of the Possible Mechanism of FRR Effect by Bulk Mixing Synthesis .....	76
5.4 Conclusion .....	83
References .....	84
Chapter 6 Conclusions and Future Research .....	89
6.1 Conclusion .....	89
6.2 Future Research .....	91
Appendix Single-Step Holographic Fabrication of Large-Area Patterned Corrugated Metal Films for Potential Application as Microfluidic Sensor <sup>†</sup> .....	92
A.1 Introduction .....	92

A.2 Experimental .....	96
A.3 Results and Discussion.....	99
A.4 Conclusion.....	106
References .....	107

## LIST OF FIGURES

Figure 1-1 Fluid velocity distribution in a microfluidic channel. The fluid velocity at the walls must be zero because of the no-slip boundary condition. Thus pressure driven flow shows parabolic velocity distribution. Therefore, a section of fluid with a flat edge experience different residence time, and the shape is deformed with time, indicated by the shape change of the red color region. As a result, the synthesized particles show broad size distribution. ....	6
Figure 2-1 Schematic of the pressure perturbation method. ....	13
Figure 2-2 Hydrodynamic focusing (HF) can improve the homogeneity of the synthesized particles. (a) Fluid velocity distribution in a microchannel. The fluid velocity at the walls must be zero because of the no-slip boundary conditions, resulting in parabolic velocity profile. Therefore, a section of fluid with a flat edge will experience different residence time, and the shape will be deformed. The synthesized particles will show broad size distribution. (b) During 2D-HF, the reaction is confined to a central plane. However, the velocity distribution still exists in the vertical direction. (c) During 3D HF, the reaction is limited in the central flow in both horizontal and vertical directions, where the fluid velocity is nearly uniform, resulting in improved homogeneity in synthesized particles.....	15
Figure 2-3 Schematic of the acoustic-assisted bubble based microfluidic reactor. ....	17
Figure 2-4 Schematic of the acoustic-assisted 3D-HF microfluidic mixer. ....	18
Figure 3-1 The Schematic of the acoustic-assisted bubble based microfluidic reactor for polyplex synthesis. ....	26
Figure 3-2 Comparison of polyplexes prepared by bulk mixing and bubble based microfluidic reactor. (a) The change of mixing index with the change in nitrogen pressure. (b) Intensity-based size distribution ( $Z_{ave,bubble} = 171.0\text{ nm}$ , $Z_{ave,bubble, acoustic} = 262.1\text{ nm}$ , $Z_{ave,bulk} = 419.1\text{ nm}$ ); (c) aggregation kinetics. ....	32
Figure 3-3 Microscopic observation of GFP transfection at 24 h post-transfection. Scale bar = 100 $\mu\text{m}$ . ....	33
Figure 3-4 Quantification of transfection efficiency and cytotoxicity. (a, b) The FSC/SSC plots suggest that the cells maintained comparable morphology after transfection with polyplexes prepared in both cases. (c, d) Bivariate plots showing the fluorescence of PI and Annexin V-Cy5 staining. The polyplexes prepared by acoustic-assisted bubble based microfluidic reactor induced less cell death and apoptosis. (e) Quantification of GFP expression level ( $n = 3$ ). $*p < 0.0445$ . (f) Quantification of cell viability. ( $n = 3$ ). $**p < 0.0013$ . (Unpaired $t$ test, CI 95%, two-tailed $p$ -value). ....	34
Figure 3-5 Quantification of Luciferase Assay ( $n = 3$ ). $***p < 0.0036$ . (Unpaired $t$ test, CI 95%, two-tailed $p$ -value). ....	35

Figure 4-1 Schematic of the microfluidic device for polyplex synthesis by 3D-HF. The DNA solution is injected through inlet A, while the polymer solution is injected from the inlet B, C, and D. ....	44
Figure 4-2 The DNA concentration distribution in cross-section areas at location 1, 2, 3, and 4 in Figure 1 at different flow rates. The total flow rate is (a) 90 $\mu\text{L}/\text{min}$ , (b) 120 $\mu\text{L}/\text{min}$ , (c) 180 $\mu\text{L}/\text{min}$ , (d) 270 $\mu\text{L}/\text{min}$ , and (e) 360 $\mu\text{L}/\text{min}$ . ....	47
Figure 4-3 Comparison of polyplexes prepared by bulk mixing and 3D-HF. (a) Size of polyplexes as a function of flow rate. (b) Intensity-based size distribution ( $Z_{ave,3D,acoustic} = 200.0 \text{ nm}$ , $Z_{ave,3D} = 263.0 \text{ nm}$ , $Z_{ave,bulk} = 419.1 \text{ nm}$ ; $PDI_{3D,acoustic} = 0.067$ , $PDI_{3D} = 0.131$ , $PDI_{bulk} = 0.142$ ); (c) aggregation kinetics. ....	48
Figure 4-4 Aggregation kinetics over 4 hours after synthesis. ....	49
Figure 4-5 (a) The velocity distribution of fluid velocity in a cross-section at a total flow rate of 360 $\mu\text{L}/\text{min}$ . (b) The velocity distribution at the center line in the cross-section in (a). ....	51
Figure 4-7 Microscopic observation of GFP transfection. At 24 h post-transfection, the human embryonic kidney (HEK293T) cells transfected by turbofect polyplexes were examined by fluorescence microscopy. Visually, the cells show comparable transfection efficiency in all cases. Scale bar = 100 $\mu\text{m}$ . ....	53
Figure 4-8 Quantification of transfection efficiency and cytotoxicity. (a-c) The FSC/SSC plots of the cells after transfected with polyplexes synthesized by bulk mixing method, and 3D-HF method without and with acoustic perturbation. (d-f) Bivariate plots to quantitatively evaluate cytotoxicity of polyplexes synthesized by bulk mixing method, and 3D-HF method without and with acoustic perturbation. (g) Quantification of GFP expression level ( $n = 3$ ). $*p < 0.026$ . (h) Quantification of cell viability. ( $n = 3$ ). $**p < 0.0042$ (i) Quantification of luciferase assay ( $n = 3$ ). $***p < 0.0004$ . (Unpaired $t$ test, CI 95%, two-tailed $p$ -value). ....	55
Figure 5-1 Schematic of the microfluidic device for hybrid nanomaterials synthesis by 3D-HF. The iso-curve shows the focusing of reagent A and the slices show the concentration distribution of reagent B. While keeping the flow rate of reagent A and B the same and changing the flow rate of buffer C and D, nanomaterials with different shapes can be synthesized. ....	64
Figure 5-2 SEM images of nanomaterials prepared while using 1.1 mM TTF solution as reagent A and 0.27 mM $\text{HAuCl}_4$ solution as reagent B. The flow rates were set to 30 $\mu\text{L}/\text{min}$ for TTF solution and 370 $\mu\text{L}/\text{min}$ for $\text{HAuCl}_4$ solution, while the flow rate of buffer (ACN) was changed. As the $\text{FRR} = (\text{A}+\text{B}):(\text{C}+\text{D})$ decreased, the morphologies of the synthesized nanomaterials experienced changes through (a) branching aggregates consisting of irregularly aligned polyhedral crystals, (b) triangle or hexagonal shape, (c) multi-layered structures consisting of thin and flat layers, (d) two dimensional dendritic nanostructures, (e) flower-like aggregates consisting of thin, flat petals and (f) coral-like aggregates consisting of fibers. ....	68

Figure 5-3 SEM images of nanomaterials prepared while using 0.27 mM H<sub>AuCl<sub>4</sub></sub> solution as reagent A and 1.1 mM TTF solution as reagent B. The flow rates were set to 30 μL/min for H<sub>AuCl<sub>4</sub></sub> solution and 370 μL/min for TTF solution, while the flow rate of buffer (ACN) was changed. As the FRR = (A+B):(C+D) increased, the morphologies of the synthesized nanomaterials experienced changes through (a) diamond shapes with apex angle of 58°, (b) long and hollow wires of several tens of micro meters, (c) wires of ~10 micrometers and (d) wires of 3-5 micrometers.....68

Figure 5-4 The concentration distribution of reagent A and B in cross-section at the location just after the inlets of buffer. The flow rate of reagent A and B are kept as 30 μL/min and 370 μL/min, respectively, and the flow rate of buffer C and D are changed. The reaction zone (at the interface between reagent A and B) are of interest. As the flow rate ratio (A+B):(C+D) decreases, the concentration of reagent A at the reaction zone almost stayed the same, while the concentration of reagent B at the reaction zone decreases. As a result, as the FRR = (A+B):(C+D) decreases, the molar ratio of A:B at the reaction zone increases. ....71

Figure 5-5 Schemes illustrating (a) the oxidation of TTF and (b) the 1D crystallization through the interaction between the neutral and oxidized TTF.....72

Figure 5-6 Absorption spectra of the solution collected from the outlet of the microfluidic channel. Two evident absorption bands derived from the π-π\* transition of the TTF<sup>+</sup> appear at 442 and 587 nm in all the cases, indicating the electron-transfer reaction and formation of TTF<sup>+</sup>. For the group of samples using TTF solution as reagent A and H<sub>AuCl<sub>4</sub></sub> solution as reagent B, as the flow rate ratio of (A+B):(C+D) increases, the absorption at wavelength around 406 nm and 510 nm increases. The absorption at 510 nm indicates the formation of gold nanoparticles. This absorption band is significantly damped because of small particle size and the organic capping by TTF. The absorption at 406 nm may be due to the coupling effect between gold nanoparticles and the TTF<sup>2+</sup> .....75

Figure 5-7 SEM images of nanomaterials prepared using bulk mixing method. As the feed molar ratio TTF/H<sub>AuCl<sub>4</sub></sub> increases, the morphologies of the synthesized nanomaterials experience changes through (a) branching aggregates consisting of irregularly aligned polyhedral crystals, (b) triangle or hexagonal shapes, (c) multi-layered structures consisting of thin and flat layers, (d) two dimensional dendritic nanostructures, (e) flower-like aggregates consisting of thin, flat petals and (f) coral-like aggregates consisting of fibers. ....77

Figure 5-8 SEM images of nanomaterials prepared using bulk mixing method. As the feed molar ratio of TTF/H<sub>AuCl<sub>4</sub></sub> increases, the morphologies of the synthesized nanomaterials experience changes through (a) diamond shape with apex angle of 58°, (b) long and hollow wires of several tens of micro meters, (c) short wires of several micro meters and (d) nano-sized needles. ....78

Figure 5-9 Absorption spectra of the solution after bulk mixing. When the feed molar ratio TTF/H<sub>AuCl<sub>4</sub></sub> ≤ 0.171, the absorption band at 510 nm increases as the TTF/H<sub>AuCl<sub>4</sub></sub> increases, indicating formation of more gold nanoparticles. The absorption bands at 442 nm and 587 nm are weak, indicating almost no formation of

TTF<sup>+</sup>. When the feed molar ratio TTF/HAuCl<sub>4</sub> ≥ 0.43, the absorption band at 510 nm decreases as the TTF/HAuCl<sub>4</sub> increases, indicating less gold nanoparticle formation. The strong bands at 442 nm and 587 nm show the presence of TTF<sup>+</sup>. In the case of TTF/HAuCl<sub>4</sub> = 0.43, the absorption band at 406 nm appears, may be due to the coupling effect between gold nanoparticles and the TTF<sup>2+</sup> .....79

Figure 5-10 The XRD pattern of the samples synthesized by bulk mixing method. The samples can be divided into 4 groups. (1) When the feed molar ratio TTF/HAuCl<sub>4</sub> ≤ 0.18, the samples show a primary peak corresponding to the face-centered cubic (fcc) structure of metallic gold with the (111) diffraction intensified considerably. (2) When TTF/HAuCl<sub>4</sub> = 0.43, the (313) structure of (TTF)Cl<sub>2</sub> appears, indicating the presence of TTF<sup>2+</sup>. (3) When TTF/HAuCl<sub>4</sub> = 0.87, no obvious peaks can be observed. (4) When TTF/HAuCl<sub>4</sub> ≥ 1.09, multiple peaks showing the crystal structures of ordered mixed valence salt, indicating the presence of both TTF<sup>+</sup> and TTF. When 1.09 ≤ TTF/HAuCl<sub>4</sub> ≤ 1.64, the (101) plane is the major crystal structure. With the further increase in TTF/HAuCl<sub>4</sub>, the (102) plane becomes the primary structure.....82

Figure 5-11 Size distribution of selected TTF-Au hybrid structures synthesized by 3D-HF and bulk mixing method. ....83

Figure A-1 Schematics of the experiment setup for fabrication of (a) 1D and (b) 2D patterned corrugated silver films. The incident laser beam from the bottom of the prism is split at the prism surface to form interference patterns on the reservoir containing Ag(NH<sub>3</sub>)<sub>2</sub><sup>+</sup> and glucose mixture. A visualization of the interference patterns are shown in the glass slides. Silver is generated faster at positions with high light intensity, resulting in a silver film with surface profile that mimics the interference pattern. (c) and (d) are the AFM images showing the surface profile of the 1D and 2D patterned corrugated silver film, respectively. Both (e) 1D and (f) 2D patterned corrugated silver films show diffraction colors under illumination with white light. ....97

Figure A-2 The relative first-order transmitted diffraction efficiency of the one dimensional patterned corrugated silver films as a function of incident angle of a 633 nm laser. The fabrication parameters of 157 mW laser power and 20 min exposure time were chosen to maximize the diffraction efficiency. ....98

Figure A-3 The diffraction color of the one dimensional patterned corrugated silver films. Incident angle of the UV-vis light source was changed while the detection angle was fixed at around 10°. The wavelength of the diffraction light red-shifted as the incident angle increased. ....100

Figure A-4 Experimental transmission intensity of the 1D patterned corrugated silver film as a function of wavelength and incident angle α, with theoretical calculations for the surface plasmons at silver/air interface (dashed line) and silver/glass interface (dashed dotted line). The inset shows the geometry of the experiment. ....101

Figure A-5 (a) At normal incidence, the transmission spectra of the 1D patterned corrugate silver film immersed into air, DI water, and several solutions of CaCl<sub>2</sub> at

different concentrations. The spectra have been displaced along the ordinate for clarity and corresponding materials information is indicated by the side of each curve. (b) Dependence of the lowest transmission wavelength and the RI of surrounding materials and the figure of merit (FoM) calculated from (a). The inset shows the data point when the surrounding material is air. .... 103

Figure A-6 The absorbance of the mixture of  $\text{Ag}(\text{NH}_3)_2^+$  and glucose solution (a) without and (b) with 514 nm laser exposure. The insets show the schematic of the experimental setup. (c) The peak position and (d) the peak intensity of the absorbance of the mixture as a function of time without and with laser exposure. The data of (c) and (d) are extracted from (a) and (b)..... 104

## LIST OF TABLES

Table 5-1 Unit Cell Data for the TTF-Chlorides .....	80
--	----

## ACKNOWLEDGEMENTS

I would like to take this opportunity to thank my dissertation advisor, Prof. Tony Jun Huang for his guidance and support throughout my Ph.D. program. He has opened the opportunity for me to reach out to collaborators from different fields and explore the potential of my research. I would also like to thank Prof. Kam Leong from Duke University, who was of great help during most of my research projects.

I am also grateful to the members of my thesis committee, Prof. Akhlesh Lakhtakia, Prof. Jian Xu, and Prof. Iam-Choon Khoo for giving me important feedback and guidance to improve this thesis.

I thank my lab member who helped me immensely during my personal and professional time at Penn State. To an international student far away from home as me, the lab members have been like my family members. Many thanks go to Dr. Yanjun Liu, Dr. Michael Ian Lapsley and Dr. Jinjie Shi, who have continuously encouraged me and given me useful suggestions. I would also like to thank Dr. Daniel Ahmed, who has been always creative and inspired me a lot. I would also like to thank my collaborators, Dr. Yi-Ping Ho and Christopher L. Grigsby, without whom half of my research would have been impossible.

I am greatly indebted to my husband, Dr. Bala Krishna Juluri, for giving me guidance and important inputs to help me start my initial research work, and for always supporting me.

Finally, I would like to convey my deepest thanks and love to my parents, Zhijian Lu and Sukun Li, who always encouraged me to follow my heart and never lose faith in me.

## **Chapter 1 Introduction**

### **1.1 Nanomaterials**

Nanomaterials are materials with at least one dimension in the range of 1 to 1000 nanometers. At such small scale, nanomaterials show special properties that distinguish them from bulk materials. For example, gold and silver nanoparticles show fascinating optical properties which enable their applications in imaging and sensing [1]. Metal and oxide nanoparticles show superior catalysis than their bulk counterpart. In pharmaceutical field, drugs with low therapeutic values in bulk size can gain enhanced therapeutic activities by being transformed in to nanosized compounds. Such properties have attracted great research interests and nanomaterials have been utilized in physical, chemical and biomedical applications. [2–7].

The unique properties of nanomaterials result from their nanosized structures, high surface-to-volume ratio, and structure-dependent electronic configurations. Variation in composition, size or shape can greatly affect the properties of nanomaterials. Therefore, it is important to maintain uniformity and reproducibility during fabrication process to obtain high-performance nanomaterials.

Besides of uniformity and reproducibility, there are also other specific requirements on fabrication process, depending on the types of applications. For industrial applications, high-throughput and continuous fabrication process is required. For biomedical applications, on-site and on-demand fabrication is necessary due to the

short shelf life of many nanomedicines. For pharmaceutical applications, *in-situ* analysis and dynamic control during the fabrication process are important to minimize the use of expensive materials during optimization process.

## 1.2 Fabrication of Nanomaterials

Two general approaches to fabricate nanomaterials are the “top-down” and “bottom-up” approaches. The “top-down” methods involve mechanical attrition of large raw materials into nanometer-size particles. “Top-down” technologies, such as media milling and high-pressure homogenization, require high energy input and relatively large amount of raw materials. Meanwhile, the fabricated nanomaterials suffer from issues such as broad size distribution and contamination. In contrast with “top-down” methods, “bottom-up” methods arrange smaller components into nanometer-size assemblies. Chemical synthesis is a generally used “bottom-up” method.

Conventional chemical synthesis process, called batch processes or bulk mixing processes, involve mixing reagents through convection, stirring, or shaking at millimetre- or centimetre-scale [8]. In such macro-scale volume, the mixing time (the time required to reach complete mixing) is determined by the reactor size and turbulence diffusivity [9]. Depending on the flow conditions (*e.g.*, viscosity and velocity), the mixing time can range from tens to hundreds of milliseconds. Meanwhile, chemical reactions take place as soon as the reagents are added into the reactor. Generally, reactions occur rapidly. For example, the second-order-reaction rate constant for metal colloidal synthesis varies between  $1 \times 10^{-2} \text{ M}^{-1} \cdot \text{s}^{-1}$  to  $1 \times 10^2 \text{ M}^{-1} \cdot \text{s}^{-1}$  [10]. DNA condensation time is of hundreds of

milliseconds [11]. Fast protein folding/unfolding reactions only take a few milliseconds. Therefore, the amount of reactions that occur during the mixing time is non-negligible. The reactions occur in unequilibrated chemical environment before the completion of mixing process result in heterogeneity of the product and batch-to-batch variability, which hinders the translation of nanomaterials research to practical applications. As a result, in spite of the intensive research effort, only very few of the nanomaterials have received approval from the US Food and Drug Administration (FDA) [12].

### **1.3 Microfluidic Reactors**

Microfluidic reactors, which confine reagents in micro-scale channels, can be considered as potential solutions to the aforementioned challenge. Compared with conventional bulk mixing techniques, microfluidic reactors offer many potential advantages such as continuous synthesis, superior reaction control and safer operational environment. Microfluidic reactors manipulates small amount of fluids at nanoliter- or even picoliter-scale in a continuous manner. The flow velocity, pressure, and chemical molar ratio between reagents can be precisely controlled via flow rate controllers (syringe pumps or pressure pumps). The option of real-time control enables the adjustment of reaction parameters as soon as small amount of products are formed and tested, in order to reduce the use of expensive and precious materials during optimization process. Due to the small volume of fluids within microfluidic reactors, the surface/volume ratio is tremendously large. Thus heat diffusion becomes highly efficient within microfluidic reactors, which minimizes the overheating due to chemical reactions and enables efficient temperature control by on-chip heaters/coolers. Microfluidic reactors are also amendable

to automation, which can reduce the human factors during the synthesis process to improve the reproducibility. Even though the throughput in a single microfluidic reactors is low, the ability to operate multiple microfluidic reactors in parallel offers the potential of high-throughput microfluidic synthesis.

## **1.4 Microfluidic Flows**

In micro-scale, the impact of surface forces, electrical effects, van der Waals interaction, and viscous forces becomes significant. Thus the flow conditions in microfluidic reactors are quite different from that in macro-scale reactors.

### **1.4.1 Laminar Flow**

Depending on the ratio between inertial to viscous forces, the fluid flow can be laminar or turbulent. The ratio is characterized by Reynolds number,  $Re$ , which can be calculated by the following equation.

$$Re = \rho vL/\mu . \quad (1-1)$$

The Reynolds number is determined by the density ( $\rho$ ) and viscosity ( $\mu$ ) of the fluid, the velocity of the flow ( $v$ ) and the diameter of the channel ( $L$ ). In microfluidic reactors, the channel diameter is at the range of tens to hundreds of micrometers. As a result, the Reynolds number in microfluidic reactors is normally less than 100, indicating the laminar flow situation.

Due to the laminar flow condition in microfluidic reactors, no turbulence is present. Mixing between two adjacent flows occurs through slow molecular diffusion

only [13–15]. The time required for the reagents to be fully mixed can be calculated as follows:

$$t = \frac{L^2}{D}. \quad (1-2)$$

The diffusion coefficient is denoted by  $D$ . Within a simple straight channel, it can take up to seconds for coflowing reagents to be fully mixed. During this slow mixing process, a chemical gradient is developed within the channel, resulting in heterogeneous chemical environment. The chemical gradient can be predicted by Fick's second law.

$$\partial\phi/\partial t = D\left(\frac{\partial^2\phi}{\partial x^2}\right). \quad (1-3)$$

The chemical concentration is  $\phi$  and the position is  $x$ . With proper design, this predictable chemical concentration distribution can be used to measure fast chemical reaction rate accurately [16]. However, during nanomaterials synthesis process, this heterogeneous chemical environment generally causes variation in size and element composition of the synthesized product.

#### **1.4.2 Parabolic Velocity Distribution**

Another feature of flow motion in microfluidic reactor is the parabolic velocity distribution. Due to the large surface-to-volume ratio, the boundary effect becomes dominant in micro-scale. The non-slip boundary condition causes parabolic flow velocity distribution in pressure driven flow, as shown in Fig. 1-1. The fluid near the boundaries shows slower velocity, while the fluid at the center of the channel shows higher velocity.

This velocity distribution results in resident time distribution, and broadens the size distribution of the synthesized product.

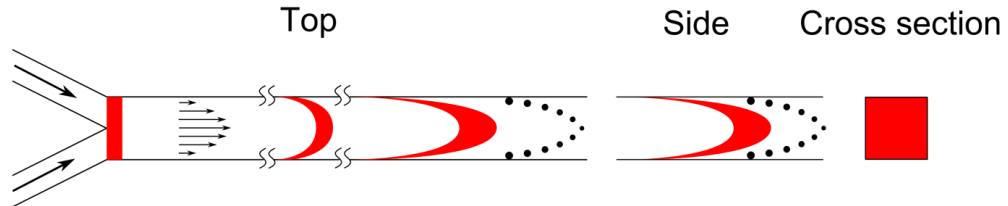


Figure 1-1 Fluid velocity distribution in a microfluidic channel. The fluid velocity at the walls must be zero because of the no-slip boundary condition. Thus pressure driven flow shows parabolic velocity distribution. Therefore, a section of fluid with a flat edge experience different residence time, and the shape is deformed with time, indicated by the shape change of the red color region. As a result, the synthesized particles show broad size distribution.

### 1.5 Challenges for Microfluidics-Based Synthesis

Due to the intrinsic properties of microfluidics discussed in Sec 1.4, it is difficult to obtain homogeneous chemical environment and resident time within simple microfluidic channels. In spite of all the aforementioned advantages of microfluidic reactors, the challenges still remain for high-uniformity and high-quality nanomaterials synthesis [17].

### 1.6 Research Objective

The chemical reactions within microfluidic reactors may be considered as diffusion-limit reactions, during which the formation of products is faster than the

diffusion of reagents. Thus the reaction rate is governed by diffusion efficiency, or molecular collision frequency. As a result, within microfluidic reactors, the mixing conditions determine the chemical concentration distributions, which further determine the reaction processes. Based on the assumption of diffusion-limit reactions, hypothesis can be made that enhanced mixing can improve the uniformity of the synthesized nanomaterials. Furthermore, by changing the mixing process precisely, the properties of the synthesized products can be finely tuned.

The aim of the research conducted for this dissertation was to examine the aforementioned hypothesis, and to push the microfluidic reactors towards practical applications by developing microfluidic reactors suitable for mass fabrication and miniaturization. Four key tasks were conducted for this aim.

The first task was to develop miniaturized microfluidic reactors suitable for mass fabrication for potential industrial and biomedical applications. Based on comparisons between existing microfluidic mixing strategies, I designed two microfluidic reactors. The second task was to examine the hypothesis that the uniformity of products can be improved by enhanced mixing. The microfluidic reactors designed during the first task were used. The third task was to evaluate the performance of the synthesized products, in order to examine if the microfluidic reactors can effectively improve the performance of the nanomaterials. The fourth task was to study the influence of mixing conditions on the diffusion-limit reactions, in order to achieve dynamic control of the nanomaterials properties by controlling the mixing conditions.

## **1.7 Organization of Dissertation**

Chapter 2 compares between existing microfluidic mixing strategies. Two microfluidic reactors designed based the comparison are presented. Chapter 3 and 4 describe polyplexes synthesis by these two designs, respectively. These two chapters discuss how the uniformity of the polyplexes can be improved by mixing enhancement through these two different approaches. The improvements in the physical properties and biological performance of the synthesized polyplexes are also presented. Chapter 5 presents organic-metal hybrid materials synthesis with different mixing conditions. These organic-metal hybrid materials are sensitive to chemical molar ratio, so they can be used to indicate the local changes in chemical molar ratio. The synthesized products show different morphologies depending on the mixing conditions. The formation mechanism is discussed. Chapter 6 presents the overall conclusion and discusses possible directions for future work. At the end, Appendix A introduces a new and simple method to fabricate corrugated silver thin films with surface plasmon resonance (SPR) properties, which have the potential applications as on-chip sensors for integrated microfluidic devices.

## References

- [1] Hu, M., Chen, J., Li, Z.-Y., Au, L., Hartland, G.V., Li, X., Marquez, M. and Xia, Y., "*Gold nanostructures: engineering their plasmonic properties for biomedical applications*," *Chemical Society Reviews*, **35**, 1084–1094 (2006)
- [2] Cheng, W., Capretto, L., Hill, M. and Zhang, X., "*Organic nanoparticles using microfluidic technology for drug-delivery applications*," in: *Nanotechnologies for the Life Sciences*, Wiley-VCH, Weinheim, Germany (2011)
- [3] Zhao, C.-X., He, L., Qiao, S.Z. and Middelberg, A.P.J., "*Nanoparticle synthesis in microreactors*," *Chemical Engineering Science*, **66**, 1463–1479 (2011)
- [4] Köstler, S. and Ribitsch, V., "*Synthetic approaches to organic nanoparticles*," in: *Nanotechnologies for the Life Sciences*, Wiley-VCH, Weinheim, Germany (2011).
- [5] Schmid, G., *Nanoparticles: from theory to application*, Wiley-VCH, Weinheim, Germany (2004)
- [6] Valencia, P.M., Farokhzad, O.C., Karnik, R. and Langer, R., "*Microfluidic technologies for accelerating the clinical translation of nanoparticles*," *Nature Nanotechnology*, **7**, 623–629 (2012)
- [7] Pumera, M., "*Nanomaterials meet microfluidics*," *Chemical Communications*, **47**, 5671–5680 (2011)
- [8] Ozin, G.A. and Arsenault, A. C., *Nanochemistry: A Chemical Approach to Nanomaterials*, The Royal Society of Chemistry, Cambridge, UK (2005)
- [9] Marchisio, D.L., Rivautella, L. and Barresi, A.A., "*Design and scale-up of chemical reactors for nanoparticle precipitation*," *AIChE Journal*, **52**, 1877–1887 (2006)
- [10] Henry, M.C., Hsueh, C.-C., Timko, B.P. and Freund, M.S., "*Reaction of pyrrole and chlorauric acid: a new route to composite colloids*," *Journal of the Electrochemical Society*, **148**, D155-D162 (2001)
- [11] Porschke, D., "*Dynamics of DNA condensation*," *Biochemistry*, **23**, 4821-4828 (1984)
- [12] Zhang, Y., Chan, H.F. and Leong, K.W., "*Advanced materials and processing for drug delivery: the past and the future*," *Advanced Drug Delivery Reviews*, **65**, 104-120 (2013)

- [13] Fraikin, J.-L., Teesalu, T., McKenney, C.M., Ruoslahti, E. and Cleland, A.N., "A *high-throughput label-free nanoparticle analyser*," Nature Nanotechnology, **6**, 308–313 (2011)
- [14] Birnbaumer, G., Küpcü, S., Jungreuthmayer, C., Richter, L., Vorauer-Uhl, K., Wagner, A., Valenta, C., Sleytr, U. and Ertl, P., "*Rapid liposome quality assessment using a lab-on-a-chip*," Lab on a Chip, **11**, 2753-2762 (2011)
- [15] Whitesides, G.M., "*The origins and the future of microfluidics*," Nature, **442**, 368–373 (2006)
- [16] Kamholz, A.E., Weigl, B.H., Finlayson, B.A. and Yager, P., "*Quantitative analysis of molecular interaction in a microfluidic channel: the T-sensor*," Analytical Chemistry, **71**, 5340–5347 (1999)
- [17] Marre, S., Park, J., Rempel, J., Guan, J., Bawendi, M.G. and Jensen, K.F., "*Supercritical continuous-microflow synthesis of narrow size distribution quantum dots*," Advanced Materials, **20**, 4830–4834 (2008)

## Chapter 2 Microfluidic Mixers

Due to the intrinsic properties of microfluidics, it is difficult to obtain homogenous chemical environment within simple microfluidic channels. Thus, different strategies have been used to enhance mixing within microfluidic channels. Based on the comparisons between these strategies by considering the mixing efficiency, ease of mass fabrication and portability, two types of microfluidic reactors were designed for nanomaterials synthesis.

### 2.1 Introduction

Due to the laminar flow condition, mixing within microfluidic channels occurs through slow molecular diffusion only. Thus different microfluidic mixing strategies have been used to achieve fast mixing within microfluidic channels. Microfluidic reactors with fast mixing performance show great potential for applications such as on-chip biomedical diagnostics, drug development, and material synthesis.

There are two general approaches to enhance mixing in microfluidic channels. One approach is increasing the contact area between reagent streams. The other approach is decreasing the length that molecules have to pass to reach complete mixing state (diffusion distance). Microfluidic mixing strategies can be cataloged into two schemes, active mixing scheme and passive mixing scheme. Active mixing scheme uses external forces to perturb the fluid inside microfluidic channels. As a result, turbulence can occur even in microfluidic channel, which can be proved by vortex formation. The turbulent

flow can increase the contact area between reagent streams and accelerate the mixing significantly. In contrast to active mixing scheme, passive mixing scheme does not require external energy sources, but relies on special designed microchannel configurations, droplet/bubble formation or flow focusing to enhance mixing efficiency. The flow motion induced by microchannel configuration and droplet/bubble formation can increase the contact area between reagent streams to enhance the mixing performance. Differently, flow focusing methods enhance the mixing efficiency by reducing the diffusion distance. The active and passive mixing schemes can be integrated together to further enhance the mixing efficiency.

## **2.2 Overview of Microfluidic Mixing Strategies**

### **2.2.1 Active Microfluidic Mixing**

Active microfluidic mixing strategies use external energies, including acoustic/ultrasonic actuation [1,2], pressure perturbation [3], dielectrophoretic force actuation [4], electrokinetic time-pulsed actuation [5], magnetic field [6], thermal actuation [7], *etc.*

Acoustic/ultrasonic actuation technique applies oscillatory perturbation from a piezoelectric disk attached to the substrate. This perturbation can induce the oscillation of channel walls, specially designed features (*e.g.*, pillars and sharp edges), or gas bubbles within microfluidic channels. As a result, fluid current (known as acoustic streaming) can

be induced near the oscillating area to enhance mixing. Acoustic/ultrasonic actuation techniques require only simple setups and can be applied for all types of fluid.

Pressure perturbation methods use periodic pressure change in the side channels to “stretch and fold” the fluid within the main channel, as shown in Fig. 2-1. Though the working mechanism is very simple, the multiple inlets and additional pressure controls make it difficult to miniaturize the device, or run multiple devices in parallel.

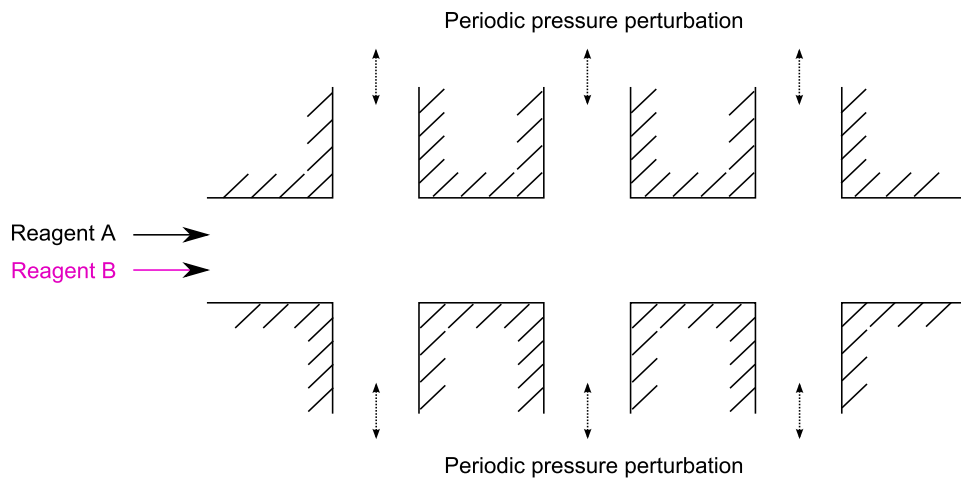


Figure 2-1 Schematic of the pressure perturbation method.

The working mechanisms of dielectrophoretic force actuation, electrokinetic time-pulsed actuation and magnetic field actuation are similar. Fluid or particles with certain dielectric or magnetic properties can be actuated by these external fields, resulting in periodic oscillation. These methods require certain physical properties of fluids or need to introduce foreign particles. Thus the choice of reagents is limited and products may be contaminated.

Thermal actuation method generates bubbles by heat to induce a wavy liquid interface to accelerate the mixing process. The high temperature requirement for bubble generation hinders the synthesis of temperature sensitive bio-nanomaterials.

### **2.2.2 Passive Microfluidic Mixing**

Passive microfluidic mixing strategies require no external energy input other than the pressure which drives the flows. Three methods are generally used for passive microfluidic mixing, including specially-designed channel configuration, droplet/bubble based small fluid volume confinement, and flow focusing method.

Specially-designed channel configurations include intersecting channels, zigzag channels, embedded barriers, slanted wells, twisted channels, 3D-serpentine structure and grooved staggered herringbones [8–18]. The fluid experiences “stretch-and-fold” after passing through these configurations. As a result, the contact area between the reagent streams increases, and mixing efficiency is enhanced. However, the enhancement in mixing efficiency by simple 2D configurations is limited. 3D configurations can be used for faster mixing, but the complicated fabrication processes make them difficult to be massively produced.

Droplet/bubble based mixing methods have also been proposed [19,20]. Due to the boundary effect at the liquid/liquid or air/liquid interface, the fluid volumes confined in droplets or between bubbles experience circulation motion. Therefore, the contact area between reagents is increased and mixing efficiency is enhanced. The droplet/bubble based mixing methods use simple channel designs which are easy to be massively

produced. During droplet generation, the use of surfactant and oil may introduce contamination into the synthesized products. Compared with droplet based mixing, bubble based mixing method are more suitable for biomedical nanomaterials synthesis due to less risk of contamination.

Flow focusing method uses sheath flow to compress the reagent streams, in order to reduce diffusion distance and enhance the mixing efficiency. At the same time, since the reagents are confined in a narrow stream by sheath flow, the resident time distribution due to the velocity distribution is narrowed, resulting in products with improved uniformity, as shown in Fig. 2-2. Two-dimensional hydrodynamic focusing (2D-HF) method only focus the reagent streams horizontally, while 3D-HF method can achieve the focusing in both horizontal and vertical directions. Therefore, 3D-HF method can provide better enhancement in mixing efficiency.

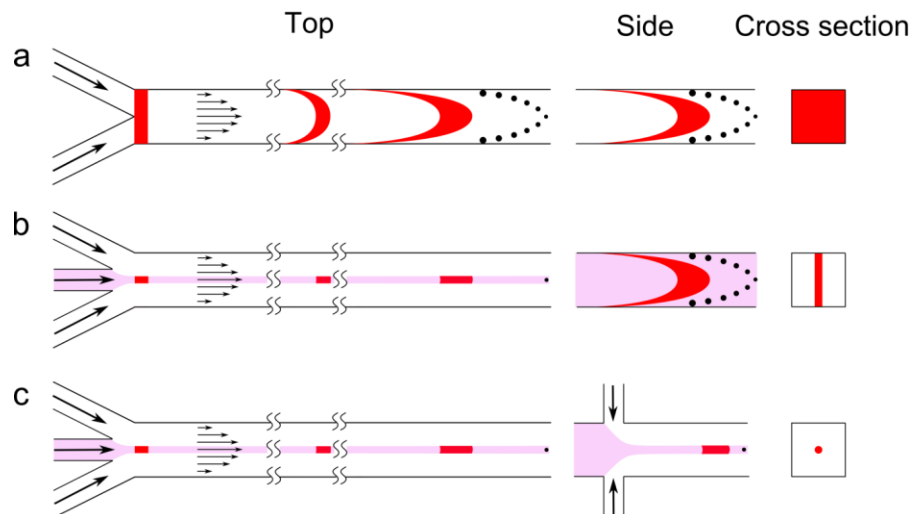


Figure 2-2 Hydrodynamic focusing (HF) can improve the homogeneity of the synthesized particles. (a) Fluid velocity distribution in a microchannel. The fluid velocity at the walls must be zero because of the no-slip boundary conditions, resulting in parabolic velocity profile. Therefore, a section of fluid with a flat edge will experience different residence time, and the shape will be

deformed. The synthesized particles will show broad size distribution. (b) During 2D-HF, the reaction is confined to a central plane. However, the velocity distribution still exists in the vertical direction. (c) During 3D HF, the reaction is limited in the central flow in both horizontal and vertical directions, where the fluid velocity is nearly uniform, resulting in improved homogeneity in synthesized particles.

Due to the intrinsic planar property of the on-chip devices, it is more difficult to achieve on-chip 3D-HF than 2D-HF. One straightforward method is to use multi-layer configurations to achieve on-chip 3D-HF [21–26]. Complicated patterns on channel walls can also induce 3D flow motion to achieve 3D-HF. However, both of multi-layer configurations and patterns on channel wall require complicated fabrication process including multiple steps of soft-lithography and alignment. Laser milling can simplify the fabrication process, but it is difficult to be applied in practical applications due to low throughput.

Within microfluidic channels with curved structure or variation in width, fluid experience migration due to inertial effect [25,27–30]. This phenomenon can be used to achieve single-layer on-chip 3D-HF. These devices meet the requirement of good focusing effect and ease of massive fabrication [25,27–33]. Therefore, inertial based 3D-HF devices are more suitable for practical applications.

### **2.3 Designs of Microfluidic Reactors for Nanomaterials Synthesis**

Based on the above discussion, acoustic/ultrasonic actuation method, bubble based mixing method and 3D-HF method are suitable for nanomaterials synthesis due to the simple setups, ease of mass fabrication, and low risk of contamination. In addition, the acoustic/ultrasonic actuation method can be integrated with the other two methods to

achieve better mixing performance. Accordingly, two microfluidic reactors are designed for the following studies on nanomaterials synthesis.

The first design is acoustic-assisted bubble based microfluidic reactor, as shown in Fig. 2-3. Bubbles are generated as nitrogen gas is injected through one of the inlets. As bubbles pass through the mixing area with chambers, they oscillate “up and down” due to the instability of motion induced by previous bubbles. This oscillation can “stretch-and fold” the fluid to enhance mixing. Later the serpentine channels further enhance the mixing performance by introducing circulation motion within fluid volumes confined between bubbles. Additionally, a piezoelectric transducer is attached by the side of the channel to supply external perturbation.

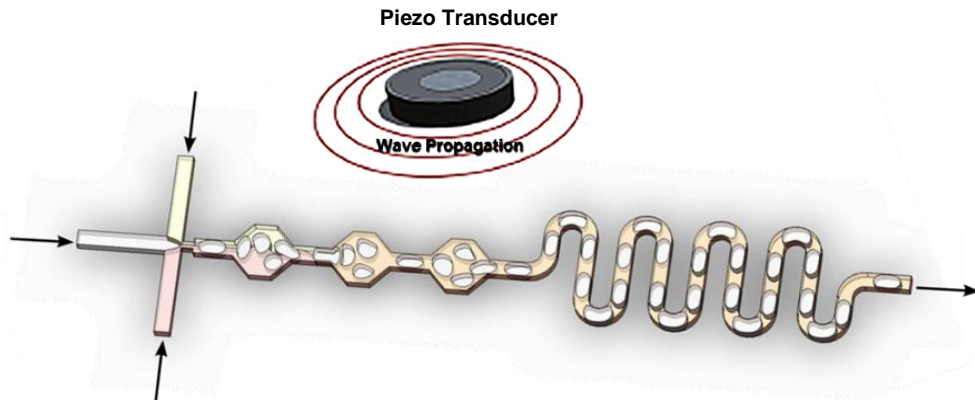


Figure 2-3 Schematic of the acoustic-assisted bubble based microfluidic reactor.

The second design is acoustic-assisted 3D-HF microfluidic reactor, as shown in Fig. 2-4. The reagent injected through inlet A can be focused in horizontal and vertical directions by flows from inlet B, C and D. As the diffusion distance is decreased by flow

focusing, mixing is enhanced. Similar to the first design, a piezoelectric transducer is attached to the substrate to supply external perturbation.

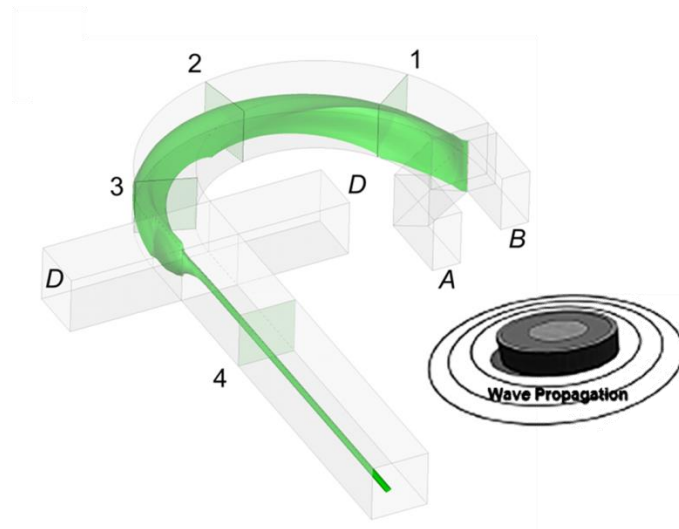


Figure 2-4 Schematic of the acoustic-assisted 3D-HF microfluidic mixer.

## References

- [1] Liu, R.H., Lenigk, R., Druyor-Sanchez, R.L., Yang, J. and Grodzinski, P., "*Hybridization enhancement using cavitation microstreaming*," Analytical Chemistry, **75**, 1911–1917 (2003)
- [2] Yaralioglu, G.G., Wygant, I.O., Marentis, T.C. and Khuri-Yakub, B.T., "*Ultrasonic mixing in microfluidic channels using integrated transducers*," Analytical Chemistry, **76**, 3694–3698 (2004)
- [3] Niu, X. and Lee, Y.-K., "*Efficient spatial-temporal chaotic mixing in microchannels*," Journal of Micromechanics and Microengineering, **13**, 454-462 (2003)
- [4] Zhao, C. and Yang, C., "*AC field induced-charge electroosmosis over leaky dielectric blocks embedded in a microchannel*," Electrophoresis, **32**, 629–637 (2011)
- [5] Yan, D., Yang, C., Miao, J., Lam, Y. and Huang, X., "*Enhancement of electrokinetically driven microfluidic Timixer using frequency modulated electric field and channel geometry effects*," Electrophoresis, **30**, 3144–3152 (2009)
- [6] Wen, C., Yeh, C., Tsai, C. and Fu, L., "*Rapid magnetic microfluidic mixer utilizing AC electromagnetic field*," Electrophoresis, **30**, 4179–4186 (2009)
- [7] Tsai, J.-H. and Lin, L., "*Active microfluidic mixer and gas bubble filter driven by thermal bubble micropump*," Sensors and Actuators A: Physical, **97**, 665–671 (2002)
- [8] Lee, C.-Y., Chang, C.-L., Wang, Y.-N. and Fu, L.-M., "*Microfluidic mixing: a review*," International Journal of Molecular Sciences, **12**, 3263–3287 (2011)
- [9] Ottino, J.M., *The Kinematics of Mixing: Stretching, Chaos, and Transport*, Cambridge University Press, Cambridge, UK (1989)
- [10] Stroock, A.D., Dertinger, S.K.W., Ajdari, A., Mezić, I., Stone, H.A. and Whitesides, G.M., "*Chaotic mixer for microchannels*," Science, **295**, 647–651 (2002)
- [11] Yang, J.-T., Huang, K.-J. and Lin, Y.-C., "*Geometric effects on fluid mixing in passive grooved micromixers*," Lab on a Chip, **5**, 1140–1147 (2005)

- [12] Floyd-Smith, T.M., Golden, J.P., Howell, P.B. and Ligler, F.S., "*Characterization of passive microfluidic mixers fabricated using soft lithography*," *Microfluidics and Nanofluidics*, **2**, 180–183 (2006)
- [13] Kang, T.G., Singh, M.K., Kwon, T.H. and Anderson, P.D., "*Chaotic mixing using periodic and aperiodic sequences of mixing protocols in a micromixer*," *Microfluidics and Nanofluidics*, **4**, 589–599 (2008)
- [14] Liu, R.H., Stremmer, M.A., Sharp, K. V, Olsen, M.G., Santiago, J.G., Adrian, R.J., Aref, H. and Beebe, D.J., "*Passive mixing in a three-dimensional serpentine microchannel*," *Microelectromechanical Systems*, **9**, 190–197 (2000)
- [15] Therriault, D., White, S.R. and Lewis, J.A., "*Chaotic mixing in three-dimensional microvascular networks fabricated by direct-write assembly*," *Nature Materials*, **2**, 265–271 (2003)
- [16] Schönfeld, F., Hessel, V. and Hofmann, C., "*An optimised split-and-recombine micro-mixer with uniform 'chaotic' mixing*," *Lab on a Chip*, **4**, 65–69 (2004)
- [17] Song, H. and Ismagilov, R.F., "*Millisecond kinetics on a microfluidic chip using nanoliters of reagents*," *Journal of the American Chemical Society*, **125**, 14613–14619 (2003)
- [18] Song, H., Bringer, M.R., Tice, J.D., Gerds, C.J. and Ismagilov, R.F., "*Experimental test of scaling of mixing by chaotic advection in droplets moving through microfluidic channels*," *Applied Physics Letters*, **83**, 4664–4666 (2003)
- [19] DeMello, A.J., "*Control and detection of chemical reactions in microfluidic systems*," *Nature*, **442**, 394–402 (2006)
- [20] Mao, X., Juluri, B.K., Lapsley, M.I., Stratton, Z.S. and Huang, T.J., "*Milliseconds microfluidic chaotic bubble mixer*," *Microfluidics and Nanofluidics*, **8**, 139–144 (2010)
- [21] Sundararajan, N., Pio, M.S., Lee, L.P. and Berlin, A.A., "*Three-dimensional hydrodynamic focusing in polydimethylsiloxane (PDMS) microchannels*," *Microelectromechanical Systems*, **13**, 559–567 (2004)
- [22] G. S. Zhuang J. P. Kutter, T.G.J., "*Three-dimensional hydrodynamic focusing over a wide reynolds number range using a two-layer microfluidic design*," *Proceedings of the 12th International Conference on Miniaturized Systems for Chemistry and Life Sciences*, Oct 12-16, San Diego, USA, 1357–1359 (2008)

- [23] Y. Shirasaki, H. Sugino, T. Arakawa, D. Yoon, J. Mizuno, S. Shoji, T. Funatsu, O. Ohara, M.G., "A microfluidic mammalian cell sorter with thermal gelation polymer solution," Proceedings of the 14th International Conference on Miniaturized Systems for Chemistry and Life Sciences, Oct 3 – 7, Groningen, Netherlands, 1571–1573 (2010)
- [24] Gambin, Y., Simonnet, C., VanDelinder, V., Deniz, A. and Groisman, A., "Ultrafast microfluidic mixer with three-dimensional flow focusing for studies of biochemical kinetics," *Lab on a Chip*, **10**, 598–609 (2010)
- [25] Mao, X., Lin, S.-C.S., Dong, C. and Huang, T.J., "Single-layer planar on-chip flow cytometer using microfluidic drifting based three-dimensional (3D) hydrodynamic focusing," *Lab on a Chip*, **9**, 1583–1589 (2009)
- [26] Kennedy, M.J., Ladouceur, H.D., Moeller, T., Kirui, D. and Batt, C.A., "Analysis of a laminar-flow diffusional mixer for directed self-assembly of liposomes," *Biomicrofluidics*, **6**, 044119 (2012)
- [27] Mao, X., Waldeisen, J.R. and Huang, T.J., "'Microfluidic drifting'—implementing three-dimensional hydrodynamic focusing with a single-layer planar microfluidic device," *Lab on a Chip*, **7**, 1260–1262 (2007)
- [28] Lee, M.G., Choi, S. and Park, J.K., "Three-dimensional hydrodynamic focusing with a single sheath flow in a single-layer microfluidic device," *Lab on a Chip*, **9**, 3155–3160 (2007)
- [29] Kim, Y., Chung, L.B., Ma, M., Mulder, W.J.M., Fayad, Z.A., Farokhzad, O.C. and Langer, R., "Mass production and size control of lipid-polymer hybrid nanoparticles through controlled microvortices," *Nano Letters*, **12**, 3587–3591 (2012)
- [30] Kim, Y., Joshi, S.D., Davidson, L.A., LeDuc, P.R. and Messner, W.C., "Dynamic control of 3D chemical profiles with a single 2D microfluidic platform," *Lab on a Chip*, **11**, 2182–2188 (2011)
- [31] Rosenauer, M., Buchegger, W., Finoulst, I., Verhaert, P. and Vellekoop, M., "Miniaturized flow cytometer with 3D hydrodynamic particle focusing and integrated optical elements applying silicon photodiodes," *Microfluidics and Nanofluidics*, **10**, 761–771 (2011)
- [32] Nieuwenhuis, J.H., Bastemeijer, J., Sarro, P.M. and Vellekoop, M.J., "Integrated flow-cells for novel adjustable sheath flows," *Lab on a Chip*, **3**, 56–61 (2003)

- [33] Rhee, M., Valencia, P.M., Rodriguez, M.I., Langer, R., Farokhzad, O.C. and Karnik, R., "*Synthesis of size-tunable polymeric nanoparticles enabled by 3D hydrodynamic flow focusing in single-layer microchannels,*" *Advanced Materials*, **23**, H79–H83 (2011)

## **Chapter 3 An Acoustic-Assisted Bubble Based Microfluidic Reactor for Polyplex Synthesis**

This chapter presents polyplexes synthesis by an acoustic-assisted bubble based microfluidic reactor. This bubble based microfluidic reactor can enhance mixing without acoustic perturbation, but the mixing efficiency is not high enough to synthesize high-quality polyplexes. With the acoustic perturbation, the synthesized polyplexes show higher uniformity and better biological performance compared to the ones synthesized by bulk mixing method.

### **3.1 Introduction**

Gene therapy has shown significant promise in the treatment of many acquired and inherited diseases. To effectively delivery genes into cells, intensive research efforts have been made to develop safe and efficient carriers. While viral carriers show very high efficiency, they also associate with high risk of infection. Nonviral gene carriers, on the other hand, are much safer, but cannot deliver genes as efficiently as viral carriers [1].

Great amount of noviral gene carriers have been designed and synthesized in order to enhance the gene delivery efficiency [2–5]. However, there have been few research interests on optimization of the physical process of DNA-polymer nanocomplexes (polyplexes) formation.

Currently, polyplexes are prepared by adding a polymer solution to a DNA solution, followed by vigorous pipetting or vortex mixing of the resulting solution in a centrifuge tube. The polyplexes form spontaneously following the introduction of

polymer and DNA solutions due to electrostatic interaction between the cationic polymer and the negatively charged nucleic acid. Although rapid vortexing or repeated pipetting can accelerate mixing, but mixing time in macro-scale reactors is still comparable with the DNA condensation time, as discussed previously in Chapter 1. Additionally, the operator's experience, or even the sequence in which reagents is added, can also greatly alter the physical properties of the resulting polyplexes [6–8]. Thus polyplexes prepared by such bulk mixing produces often suffer from poor uniformity, batch-to-batch variability, as well as subsequent aggregation. As a result, polyplexes prepared by bulk mixing processes show poor biological performance and reproducibility [9,10].

Microfluidic devices [11–13] amenable to automated operation have attracted increasing interest due to their ability to minimize human factors and synthesize uniform products [14–27]. The reaction conditions (*e.g.*, reagent ratio, flow rate, ionic concentration) can be finely tuned, leading to highly controllable parameterization throughout the complexation process [27–29]. However, due to the intrinsic properties of flow in microfluidic channel, efficient mixing is difficult to achieve.

Fast and efficient mixing is particularly important for reactions of fast kinetics, such as charge neutralization of polyelectrolytes [30]. Towards this end, microfluidic fast mixing strategies have been used to enhance mixing and provide homogenous parameters [31]. A wide variety of designs for fast mixing in microfluidic devices have been proposed. However, most of the designs require complex configuration and fabrication of 3D microfluidic channels. The complication fabrication processes are not suitable for mass production. Therefore, designs with complex configurations have limited potential

in practical applications [32–39]. Ho *et al.* showed that the self-assembly of polyplexes through simple microfluidics-assisted confinement (MAC) in picoliter droplets produces more homogenous and compact polyplexes [5,8]. Although promising, the MAC approach requires the use of oil and surfactant to generate and stabilize water-in-oil emulsion [5,8,40], which may introduce contamination into the synthesized polyplexes.

In Chapter 2, two designs of microfluidic reactors were presented. Here, the first design, the acoustic-assisted bubble-based microfluidic reactor, is used for polyplexes synthesis. The device includes one inlet for gas (middle) and two inlets for polymer (cationic carrier) solution and DNA solution, as well as a series of hexagonal expansion chambers to enhance mixing (Fig. 3-1). The serpentine channel following the expansion chambers can induce circulation within fluid volumes. Finally, to further enhance the mixing performance, a disc transducer is glued to the side of the microfluidic channel to supply acoustic perturbation. This single-layer microfluidic device requires no alignment or complicated fabrication process.

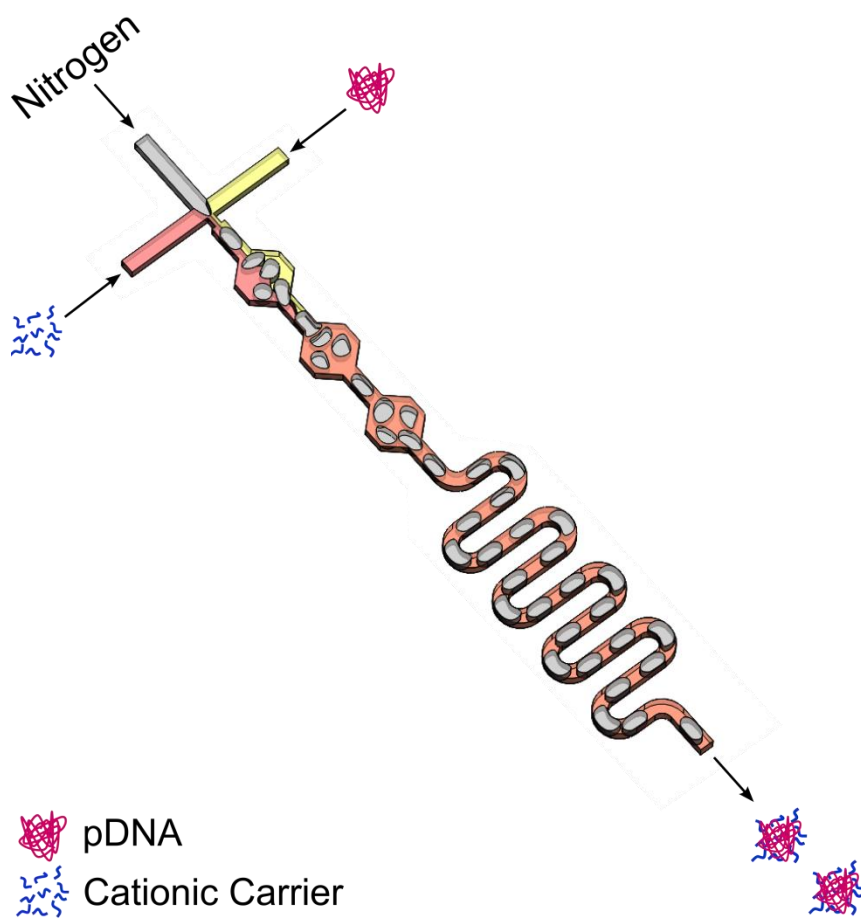


Figure 3-1 The Schematic of the acoustic-assisted bubble based microfluidic reactor for polyplex synthesis.

### 3.2 Materials and Methods

#### 3.2.1 Device Fabrication

The bubble based microfluidic reactor is a single-layer polydimethylsiloxane (PDMS) microchannel fabricated using soft lithography techniques [41,42]. Firstly, the mold was patterned on a silicon wafer with photoresist (SU8-2050). The surface of the

mold was modified to render hydrophobicity by coating it with 1H,1H,2H,2H-perfluorooctyl-trichlorosilane. The PDMS mixture was prepared by mixing the base and curing agent (Sylgard 184 Silicone Elastomer from Dow Corning) at the weight ratio of 10:1. Then the PDMS mixture was poured onto the mold, degassed in a vacuum chamber, and later cured at 65 °C for 30 min. Subsequently, the half-baked PDMS channel was removed from the mold and inlets and outlets were drilled with a Harris Uni-Core puncher. The half-baked PDMS channel was then treated with oxygen plasma, bonded to a micro cover glass slide, and further cured at 65 °C overnight. Finally, a piezoelectric transducer was attached to the side of the microfluidic device using. Before polyplexes synthesis, the channel was washed with 70% ethanol in water, rinsed with water, and then exposed to UV light for 1 h.

### **3.2.2 Materials**

Two reporter DNA vectors were used. The first reporter DNA vector is pmax-GFP (Amara, Cologne, Germany), which encodes with green fluorescent protein (GFP). The other reporter DNA vector used here is VR1255C (Vical, San Diego, CA), which encodes firefly luciferase (Luc). These two reporter DNA vectors are generally used to quantify the transfection efficiency.

The polymer used here is turbofect (poly(2-hydroxypropyleneimine), pHP) transfection reagent (Thermo Scientific).

All materials were used directly without any further treatment.

### **3.2.3 Polyplexes Synthesis in the Microfluidic Reactor**

The microfluidic reactor was connected to syringes *via* tubing, and the flow rate was controlled by a neMESYS syringe pump system (Cetoni GmbH). DNA stock solution was diluted to 13.2  $\mu\text{g}/\text{mL}$  in Opti-MEM reduced-serum medium. Turbofect transfection reagent was also diluted to 26.4  $\mu\text{L}/\text{mL}$  in Opti-MEM reduced-serum medium. The DNA solution and turbofect solution were co-injected at the same flow rate of 50  $\mu\text{L}/\text{min}$  into the microfluidic reactor. Meanwhile, nitrogen gas was injected from the central inlet, as demonstrated in Fig. 3-1.

### **3.2.4 Polyplexes Synthesis by Bulk Mixing Method**

The concentrations of DNA and turbofect solutions were kept the same as the ones used in microfluidic experiments. In a 2 mL centrifuge tube, 1 mL of the turbofect solution was added to 1 mL DNA solution, followed by vigorous pipetting for 1 min.

### **3.2.5 Cell Culture**

The cell type used here is the human embryonic kidney (HEK293T) cell line. The HEK293T cells were cultured in culture medium at 37 °C with 5% CO<sub>2</sub> in the incubator. The culture medium is Eagle's Minimum Essential Medium (EMEM) containing 10% heat-inactivated fetal bovine serum and 1% Penicillin/Streptomycin medium.

### 3.2.6 Transfection

Before transfection, HEK293T cells were seeded in 12-well plates at a density of  $1 \times 10^5$  cells/well, with 1 mL/well of cell culture medium. Then the HEK293T cells were cultured at 37 °C with 5% CO<sub>2</sub> in the incubator for 24 hours.

During transfection, the cell culture medium in each well was replaced by 400 µL Opti-MEM solution containing polyplexes. The polyplexes used in each well contained 1.5 µg of DNA. The cells were then incubated for 4 hours. After that, Opti-MEM solution with polyplexes was replaced by cell culture medium. Finally, the cells were incubated for 24 hours when using pGFP and 36 hours when using pLuc before characterization.

### 3.2.7 Characterization

The polyplex size ( $Z$  average diameter,  $Z_{ave}$ ) and polydispersity index (PDI) were directly measured using the Zetasizer NanoS system (Malvern Instruments). All measurements were carried out at 25 °C, using the refractive index (1.330) and viscosity (0.8872 cP) of water for data analysis. Each sample was measured at three minute intervals for a total time of one hour. The reported standard deviation was calculated as  $\sigma^2 = \text{PDI} \times (Z_{ave})^2$  with the assumption of a Gaussian distribution [8].

For the pGFP transfection study, the transfected cells were characterized by using fluorescence microscopy and flow cytometry. The apoptosis assay was carried out through flow cytometry after Annexin-V (AV) and Propidium Iodide (PI) staining [43].

For the pLuc transfection study, the transfected cells were lysed in 400  $\mu\text{L}$  of Glo Lysis Buffer (Promega). Then the lysate was transferred to a 96-well plate and mixed with equal amount of Steady-Glo Assay Reagent (Promega). After 20 minutes, the luminescence intensity was measured through the Fluoroskan Ascent FL.

### 3.3 Results and Discussion

#### 3.3.1 Optimization of Operation Parameters

The flow rates of DNA and polymer solutions were fixed at 50  $\mu\text{L}/\text{min}$ , while the pressure of the nitrogen was undetermined. The optimization of nitrogen pressure value was based on the mixing efficiency. Water and ink were co-injected at the same flow rate of 50  $\mu\text{L}/\text{min}$ . Then the mixing performance was measured by the mixing index ( $M$ ) of fluids near the outlet channel [44,45]

$$M = \sqrt{\frac{1}{n} \sum_{i=1}^n \left( \frac{I_i - I_m}{I_m} \right)^2}, \quad (3-1)$$

where  $I_i$  is the gray scale value at the measured point along the width of the channel. The average gray scale of all the measured points is  $I_m$ , and the total number of measured points is  $n$ . A mixing index value of 1.0 indicates complete separated solutions and a mixing index of 0.0 indicates completely mixed solutions. The mixing index near the outlet channel with different pressure of nitrogen is shown in Fig. 3-2 a, indicating that the mixing performance is improved with the increase of pressure. The best mixing

performance was obtained with 20 psi of pressure. Since further increase in pressure may cause leakage in microfluidic reactors, 20 psi was used as the optimized pressure.

### 3.3.2 Size Distribution

At the optimized pressure, polyplexes prepared by bubble based microfluidic reactor without acoustic perturbation show smaller size compared to those prepared by bulk mixing ( $Z_{ave,bubble} = 171.0 \text{ nm}$  versus  $Z_{ave,bulk} = 419.1 \text{ nm}$ ). However, the size distribution of the polyplexes synthesized by the bubble based mixer without acoustic is broad, as shown in Fig. 3-2 b.

To improve the size distribution, acoustic perturbation was applied. The acoustic oscillation of the microfluidic channel and the bubbles can cause liquid motion or vortices known as acoustic streaming [46]. Even at micrometer scale, turbulence can still be induced actively by acoustic oscillation, resulting in fast mixing. Fig. 3-2 b show the size distribution of polyplexes prepared by bulk mixing, the bubble based microfluidic reactor with and without acoustic perturbation. As expected, introduction of acoustic perturbation helps in generating particles with smaller size compared to bulk mixing sample ( $Z_{ave,bubble, acoustic} = 262.1 \text{ nm}$ ), and lowest polydispersity in all cases.

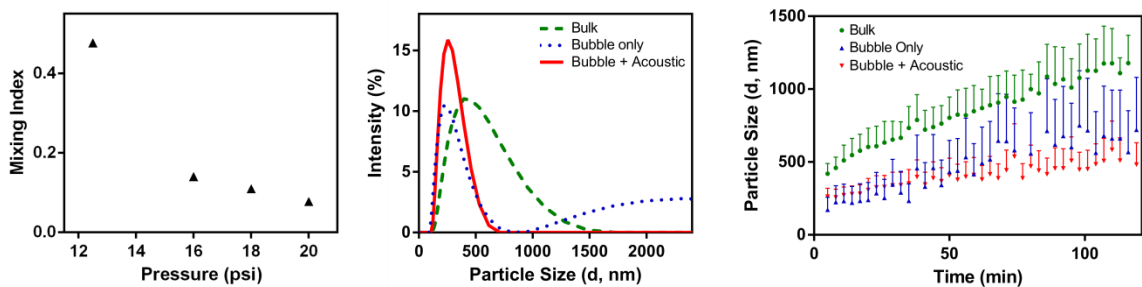


Figure 3-2 Comparison of polyplexes prepared by bulk mixing and bubble based microfluidic reactor. (a) The change of mixing index with the change in nitrogen pressure. (b) Intensity-based size distribution ( $Z_{ave,bubble} = 171.0 \text{ nm}$ ,  $Z_{ave,bubble,acoustic} = 262.1 \text{ nm}$ ,  $Z_{ave,bulk} = 419.1 \text{ nm}$ ); (c) aggregation kinetics.

### 3.3.3 Aggregation Kinetic Studies

Aside from the heterogeneity, significant aggregation is also observed in polyplexes prepared by bulk mixing method, presumably due to a corona of excess polycation and an uneven surface coverage [47]. As shown in Fig. 3-2 c, comparison of the aggregation kinetics of polyplexes prepared by bulk mixing and bubble based microfluidic reactor without and with acoustic perturbation suggests that the latest produces more stable particles without any treatment, such as PEGylation or addition of anti-caking agent. The improved size uniformity and slower aggregation rate exhibited by polyplexes prepared with bubble based microfluidic reactor, especially with acoustic perturbation, is most likely due to the enhanced mixing, which in turn led to a more uniform surface property of the synthesized polyplexes. Thereby the aggregation or flocculation that typically occurs in solution is reduced.

### 3.3.4 Biological Performance of the Synthesized Polyplexes

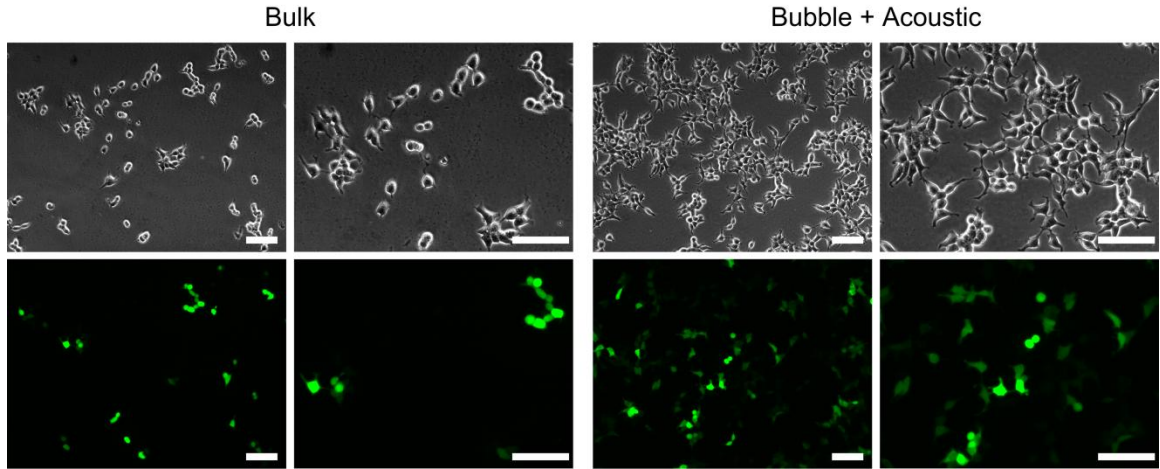


Figure 3-3 Microscopic observation of GFP transfection at 24 h post-transfection. Scale bar = 100  $\mu\text{m}$ .

Fig. 3-3 to Fig. 3-5 show the comparison of the biological performance between the polyplexes prepared by bulk mixing and acoustic-assisted bubble based microfluidic reactor. The reporter DNA vectors pmax-GFP encoding green fluorescent protein (GFP) was used for polyplexes synthesis. Qualitatively, the cells in the case of acoustic-assisted bubble based microfluidic reactor show healthier morphologies and higher transfection efficiency (Fig. 3-3). Quantitatively, acoustic-assisted bubble based microfluidic reactor prepared polyplexes achieve ~75% transfection, which is about 10% increase compared to the 65% in the case of bulk mixing (Fig. 3-4 e).

Similar distributions in forward scatter/side scatter (FSC/SSC) plots (Fig. 2-4 a, b) suggest that the cells maintained comparable morphologies after transfection with polyplexes prepared in both cases. Further investigation show that polyplexes prepared by acoustic-assisted bubble based microfluidic reactor induced less cell death (PI+) and

apoptosis (PI-, Annexin V+) [43] than those prepared by the bulk mixing method (Fig. 3-4 c, d). The percentages of viable cells are shown Fig. 3-4 f.

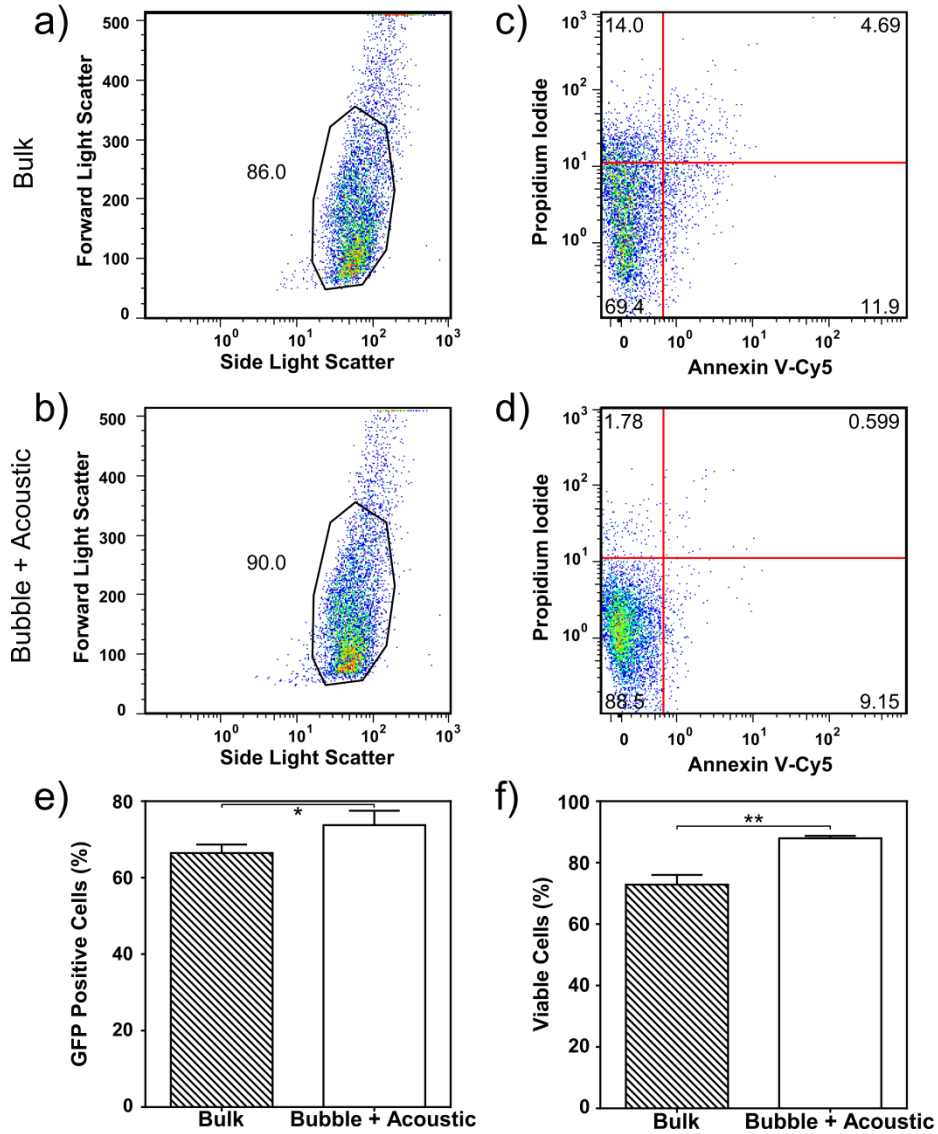


Figure 3-4 Quantification of transfection efficiency and cytotoxicity. (a, b) The FSC/SSC plots suggest that the cells maintained comparable morphology after transfection with polyplexes prepared in both cases. (c, d) Bivariate plots showing the fluorescence of PI and Annexin V-Cy5 staining. The polyplexes prepared by acoustic-assisted bubble based microfluidic reactor induced less cell death and apoptosis. (e) Quantification of GFP expression level ( $n = 3$ ).  $*p < 0.0445$ . (f) Quantification of cell viability. ( $n = 3$ ).  $**p < 0.0013$ . (Unpaired  $t$  test, CI 95%, two-tailed  $p$ -value).

To complement the transfection parameter of percent cells transfected, I also measured the total gene expression level using the firefly luciferase (pLuc) reporter gene. The results are shown in Fig. 3-5. Consistent with the GFP-transfection results, polyplexes prepared by acoustic-assisted bubble based microfluidic reactors showed greater luminescence intensity when compared to the bulk mixing case.

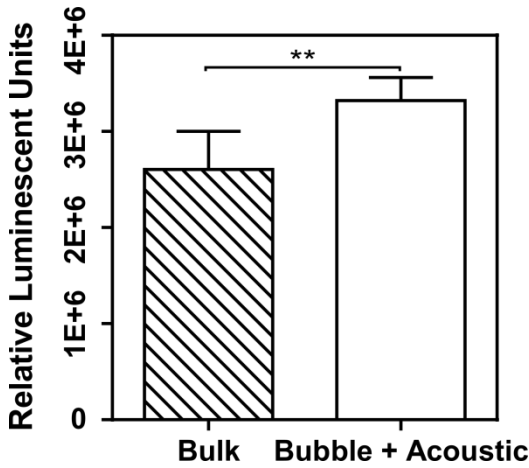


Figure 3-5 Quantification of Luciferase Assay ( $n = 3$ ). \*\*\* $p < 0.0036$ . (Unpaired  $t$  test, CI 95%, two-tailed  $p$ -value).

### 3.4 Conclusion

In this chapter, the polyplex synthesis using an acoustic-assisted bubble based microfluidic reactor is demonstrated. Firstly, the mixing enhancement by this acoustic-assisted bubble based microfluidic reactor is proved by experiments using ink and water. Later, the polyplexes prepared by this reactor show smaller size, slower aggregation rate, higher transfection efficiency, and lower cytotoxicity compared to those prepared by the

bulk mixing method. The acoustic-assisted bubble based microfluidic reactor can produce high-quality polyplexes in an operator-independent, simple, and scalable manner. The improved reproducibility and efficacy derived from this acoustic-assisted bubble based microfluidic reactor may contribute to the future development of translational nucleic acid therapeutics.

## References

- [1] Thomas, M. and Klibanov, A.M., "*Non-viral gene therapy: polycation-mediated DNA delivery*," Applied Microbiology and Biotechnology, **62**, 27–34 (2003)
- [2] Parhamifar, L., Larsen, A.K., Hunter, A.C., Andresen, T.L. and Moghimi, S.M., "*Polycation cytotoxicity: a delicate matter for nucleic acid therapy-focus on polyethylenimine*," Soft Matter, **6**, 4001–4009 (2010)
- [3] Grigsby, C.L. and Leong, K.W., "*Balancing protection and release of DNA: tools to address a bottleneck of non-viral gene delivery*," Journal of The Royal Society Interface, **7**, S67–S82 (2010)
- [4] Jiang, X., Zheng, Y., Chen, H.H., Leong, K.W., Wang, T.-H. and Mao, H.-Q., "*Dual-sensitive micellar nanoparticles regulate DNA unpacking and enhance gene-delivery efficiency*," Advanced Materials, **22**, 2556–2560 (2010)
- [5] Grigsby, C.L., Ho, Y.-P., Lin, C., Engbersen, J.F.J. and Leong, K.W., "*Microfluidic preparation of polymer-nucleic acid nanocomplexes improves nonviral gene transfer*," Scientific Reports, **3**, 3155 (2013)
- [6] Boussif, O., Lezoualch, F., Zanta, M.A., Mergny, M.D., Scherman, D., Demeneix, B. and Behr, J.P., "*A versatile vector for gene and oligonucleotide transfer into cells in culture and in-vivo - polyethylenimine*," Proceedings of the National Academy of Sciences of the United States of America, **92**, 7297–7301 (1995)
- [7] Boussif, O., Zanta, M.A., and Behr, J.P., "*Optimized galenics improve in vitro gene transfer with cationic molecules up to 1000-fold*," Gene Therapy, **3**, 1074-1080 (1996)
- [8] Ho, Y.-P., Grigsby, C.L., Zhao, F. and Leong, K.W., "*Tuning physical properties of nanocomplexes through microfluidics-assisted confinement*," Nano Letters, **11**, 2178–2182 (2011)
- [9] Sharma, V.K., Thomas, M. and Klibanov, A.M., "*Mechanistic studies on aggregation of polyethylenimine-DNA complexes and its prevention*," Biotechnology and Bioengineering, **90**, 614–620 (2005)
- [10] Xu, Y.H., Hui, S.W., Frederik, P. and Szoka, F.C., "*Physicochemical characterization and purification of cationic lipoplexes*," Biophysical Journal, **77**, 341–353 (1999)

- [11] Whitesides, G.M., "The origins and the future of microfluidics," *Nature*, **442**, 368–373 (2006)
- [12] Mao, X. and Huang, T.J., "Microfluidic diagnostics for the developing world," *Lab on a Chip*, **12**, 1412–1416 (2012)
- [13] Neuži, P., Giselbrecht, S., Länge, K., Huang, T.J. and Manz, A., "Revisiting lab-on-a-chip technology for drug discovery," *Nature Reviews Drug Discovery*, **11**, 620–632 (2012)
- [14] Vladislavljević, G.T., Henry, J. V, Duncanson, W.J., Shum, H.C. and Weitz, D.A., "Fabrication of biodegradable poly (lactic acid) particles in flow-focusing glass capillary devices," *Progress in Colloid and Polymer Science*, **139**, 111–114 (2012)
- [15] Abate, A.R., Romanowsky, M.B., Agresti, J.J. and Weitz, D.A., "Valve-based flow focusing for drop formation," *Applied Physics Letters*, **94**, 23503 (2009)
- [16] Valencia, P.M., Farokhzad, O.C., Karnik, R. and Langer, R., "Microfluidic technologies for accelerating the clinical translation of nanoparticles," *Nature Nanotechnology*, **7**, 623–629 (2012)
- [17] Fei, Z., Hu, X., Choi, H., Wang, S., Farson, D. and Lee, L.J., "Micronozzle array enhanced sandwich electroporation of embryonic stem cells," *Analytical Chemistry*, **82**, 353–358 (2009)
- [18] Rajagopalan, K.K., Chen, J., Lu, B. and Wang, S., "Manufacturing DNA nanowires with air blowing assembly on micropatterned surface," *Nano LIFE*, **3**, 1350001 (2013)
- [19] Kürsten, D., Cao, J., Funfak, A., Müller, P. and Köhler, J.M., "Cultivation of *Chlorella vulgaris* in microfluid segments and microtoxicological determination of their sensitivity against  $\text{CuCl}_2$  in the nanoliter range," *Engineering in Life Sciences*, **11**, 580–587 (2011)
- [20] Jebrail, M.J., Assem, N., Mudrik, J.M., Dryden, M.D.M., Lin, K., Yudin, A.K. and Wheeler, A.R., "Combinatorial synthesis of peptidomimetics using digital microfluidics," *Journal of Flow Chemistry*, **2**, 103–107 (2012)
- [21] Jebrail, M.J., Ng, A.H.C., Rai, V., Hili, R., Yudin, A.K. and Wheeler, A.R., "Synchronized synthesis of peptide-based macrocycles by digital microfluidics," *Angewandte Chemie*, **122**, 8807–8811 (2010)
- [22] Wang, H., Liu, K., Chen, K.-J., Lu, Y., Wang, S., Lin, W.-Y., Guo, F., Kamei, K., Chen, Y.-C., Ohashi, M., Wang, M., Garcia, M.A., Zhao, X.-Z., Shen, C.K.F. and

- Tseng, H.-R., "A rapid pathway toward a superb gene delivery system: programming structural and functional diversity into a supramolecular nanoparticle library," *ACS Nano*, **4**, 6235–6243 (2010)
- [23] Liu, K., Wang, H., Chen, K.J., Guo, F., Lin, W.Y., Chen, Y.C., Phung, D.L., Tseng, H.R. and Shen, C.K., "A digital microfluidic droplet generator produces self-assembled supramolecular nanoparticles for targeted cell imaging," *Nanotechnology*, **21**, 445603 (2010)
- [24] Zeng, Q., Guo, F., Yao, L., Zhu, H.W., Zheng, L., Guo, Z.X., Liu, W., Chen, Y., Guo, S.S. and Zhao, X.Z., "Milliseconds mixing in microfluidic channel using focused surface acoustic wave," *Sensors and Actuators B: Chemical*, **160**, 1552–1556 (2011)
- [25] Ji, X.-H., Cheng, W., Guo, F., Liu, W., Guo, S.-S., He, Z.-K. and Zhao, X.-Z., "On-demand preparation of quantum dot-encoded microparticles using a droplet microfluidic system," *Lab on a Chip*, **11**, 2561-2568 (2011)
- [26] Ji, X.-H., Zhang, N.-G., Cheng, W., Guo, F., Liu, W., Guo, S.-S., He, Z.-K. and Zhao, X.-Z., "Integrated parallel microfluidic device for simultaneous preparation of multiplex optical-encoded microbeads with distinct quantum dot barcodes," *Journal of Materials Chemistry*, **21**, 13380–13387 (2011)
- [27] Yang, S., Guo, F., Kiraly, B., Mao, X., Lu, M., Leong, K.W. and Huang, T.J., "Microfluidic synthesis of multifunctional Janus particles for biomedical applications," *Lab on a Chip*, **12**, 2097–2102 (2012)
- [28] Debus, H., Beck-Broichsitter, M. and Kissel, T., "Optimized preparation of pDNA/poly(ethylene imine) polyplexes using a microfluidic system," *Lab on a Chip*, **12**, 2498–2506 (2012)
- [29] Kasper, J.C., Schaffert, D., Ogris, M., Wagner, E. and Friess, W., "The establishment of an up-scaled micro-mixer method allows the standardized and reproducible preparation of well-defined plasmid/LPEI polyplexes," *European Journal of Pharmaceutics and Biopharmaceutics*, **77**, 182–185 (2011)
- [30] Ho, Y.P., Chen, H.H., Puleo, C.M., Yeh, H.C., Leong, K.W. and Wang, T.H., "Quantitative kinetic analysis of DNA nanocomplex self-assembly with quantum dots FRET in a microfluidic device," *Proceedings of Micro Electro Mechanical Systems*, Jan 13-17, Tucson, USA, 30–33 (2008)
- [31] Ottino, J.M., *The Kinematics of Mixing: Stretching, Chaos, and Transport*, Cambridge University Press, Cambridge, UK (1989)

- [32] Song, H., Bringer, M.R., Tice, J.D., Gerds, C.J. and Ismagilov, R.F., "*Experimental test of scaling of mixing by chaotic advection in droplets moving through microfluidic channels,*" *Applied Physics Letters*, **83**, 4664–4666 (2003)
- [33] Song, H. and Ismagilov, R.F., "*Millisecond kinetics on a microfluidic chip using nanoliters of reagents,*" *Journal of the American Chemical Society*, **125**, 14613–14619 (2003)
- [34] Schönfeld, F., Hessel, V. and Hofmann, C., "*An optimised split-and-recombine micro-mixer with uniform ‘chaotic’ mixing,*" *Lab on a Chip*, **4**, 65–69 (2004)
- [35] Liu, R.H., Stremler, M.A., Sharp, K. V, Olsen, M.G., Santiago, J.G., Adrian, R.J., Aref, H. and Beebe, D.J., "*Passive mixing in a three-dimensional serpentine microchannel,*" *Microelectromechanical Systems*, **9**, 190–197 (2000)
- [36] Therriault, D., White, S.R. and Lewis, J.A., "*Chaotic mixing in three-dimensional microvascular networks fabricated by direct-write assembly,*" *Nature Materials*, **2**, 265–271 (2003)
- [37] Kang, T.G., Singh, M.K., Kwon, T.H. and Anderson, P.D., "*Chaotic mixing using periodic and aperiodic sequences of mixing protocols in a micromixer,*" *Microfluidics and Nanofluidics*, **4**, 589–599 (2008)
- [38] Floyd-Smith, T.M., Golden, J.P., Howell, P.B. and Ligler, F.S., "*Characterization of passive microfluidic mixers fabricated using soft lithography,*" *Microfluidics and Nanofluidics*, **2**, 180–183 (2006)
- [39] Yang, J.-T., Huang, K.-J. and Lin, Y.-C., "*Geometric effects on fluid mixing in passive grooved micromixers,*" *Lab on a Chip*, **5**, 1140–1147 (2005)
- [40] Zec, H., Rane, T.D. and Wang, T.-H., "*Microfluidic platform for on-demand generation of spatially indexed combinatorial droplets,*" *Lab on a Chip*, **12**, 3055–3062 (2012)
- [41] Mao, X., Lin, S.-C.S., Dong, C. and Huang, T.J., "*Single-layer planar on-chip flow cytometer using microfluidic drifting based three-dimensional (3D) hydrodynamic focusing,*" *Lab Chip*, **9**, 1583–1589 (2009)
- [42] Mao, X., Waldeisen, J.R. and Huang, T.J., "*“Microfluidic drifting”--- implementing three-dimensional hydrodynamic focusing with a single-layer planar microfluidic device,*" *Lab on a Chip*, **7**, 1260–1262 (2007)

- [43] Moghimi, S.M., Symonds, P., Murray, J.C., Hunter, A.C., Debska, G. and Szewczyk, A., "A two-stage poly(ethylenimine)-mediated cytotoxicity: Implications for gene transfer/therapy," *Molecular Therapy*, **11**, 990–995 (2005)
- [44] Garstecki, P., Fischbach, M.A. and Whitesides, G.M., "Design for mixing using bubbles in branched microfluidic channels," *Applied Physics Letters*, **86**, 244108 (2005)
- [45] Fuerstman, M. and Samuel, K., "Mixing with bubbles: a practical technology for use with portable microfluidic devices," *Lab on a Chip*, **6**, 207–212 (2006)
- [46] Zhu, X. and Kim, E.S., "Microfluidic motion generation with acoustic waves," *Sensors and Actuators A: Physical*, **66**, 355–360 (1998)
- [47] Hunter, R.J., *Introduction to Modern Colloid Science*, Oxford University Press, New York, NY (1994)

## Chapter 4 A Three-Dimensional Hydrodynamic Focusing Method for Polyplex Synthesis<sup>‡</sup>

This chapter presents the use of 3D-HF microfluidic reactor for polyplexes synthesis. Compared with the acoustic-assisted bubble based microfluidic reactor, this 3D hydrodynamic focusing device is easier to operate since no gas is involved. The polyplexes synthesized by this 3D hydrodynamic focusing device also show better biological performance.

### 4.1 Introduction

Successful intracellular delivery of nucleic acid relies on multi-aspect optimization, one of which is formulation. While there has been ample innovation on chemical design of polymeric gene carriers, the same cannot be said for physical processing of polymer-DNA nanocomplexes (polyplexes). In Chapter 3, synthesis of polyplexes by acoustic-assisted bubble based microfluidic reactor was demonstrated. The synthesized polyplexes show smaller size and better stability compared to those by bulk mixing method. However, one disadvantage of the bubble based microfluidic reactor is the introduction of gas phase, which makes it difficult to miniaturize the device for on-site and on-demand synthesis applications.

---

<sup>‡</sup>This chapter is based on: M. Lu, Y.-P. Ho, C. L. Grigsby, A. A. Nawaz, K. W. Leong, and T. J. Huang, "A three-dimensional hydrodynamic focusing method for polyplexes synthesis," ACS Nano, **8**, 332-339, (2014)

Another microfluidic mixing strategy, hydrodynamic focusing, has been used to enhance mixing and provide homogenous environment within the reaction zone [1–16]. As the central solution is focused by the sheath of outer fluids, the diffusion distance decreases, resulting in faster mixing [3,17]. Two-dimensional (2D) hydrodynamic focusing, which focuses the central solution in the horizontal plane only, has been used to prepare polyplexes [4] and lipoplexes [5]. However, transverse diffusive broadening observed in existing two-phase laminar flows [6] in the vertical direction compromises the quality of the synthesized polyplexes. A better design to ensure effective mixing in microfluidic devices is needed [7]. Compared with 2D hydrodynamic focusing, 3D hydrodynamic focusing (3D-HF) can further enhance mixing by squeezing the center stream in both horizontal and vertical direction.

In recent years, different designs with intrinsic 3D structures for 3D-HF have been proposed, which require complicated fabrication and are not suitable for mass fabrication [8,9,11]. Rhee *et al.* have demonstrated a single-layer 3D-HF device for polymer nanoparticles synthesis. In their design, three sequential inlets with precisely controlled size and alignment are used for vertical focusing, and a conventional cross junction is used for horizontal focusing [15]. Rhee's 3D-HF device show advantages in synthesis applications over 2D-HF devices, but the stringent control required for the inlet drilling and the low flow rate diminish the appeal of this design. Previously, a “microfluidic drifting” technique was developed to achieve 3D-HF in a single-layer, planar microfluidic structure for on-chip flow cytometry application [10,12,13]. This 3D-HF device can be fabricated through single-step standard soft lithography without multi-

layer assembly requirements, rendering it ideal for low-cost and large-scale production. However, this first generation of “microfluidic drifting” based 3D-HF device is not suitable for nanoparticle synthesis due to a relatively low ratio between central and total flow rate (~1:17), which may result in diluted concentration of the synthesized polyplexes.

I redesigned the “microfluidic drifting” based 3D-HF device for polyplexes synthesis application. The new device has an 180° curved channel section, and the ratio between central and total flow rate is 1:3, as shown in Fig. 4-1. In addition, external acoustic perturbation is introduced to further enhance the mixing in the focused stream [18–26].

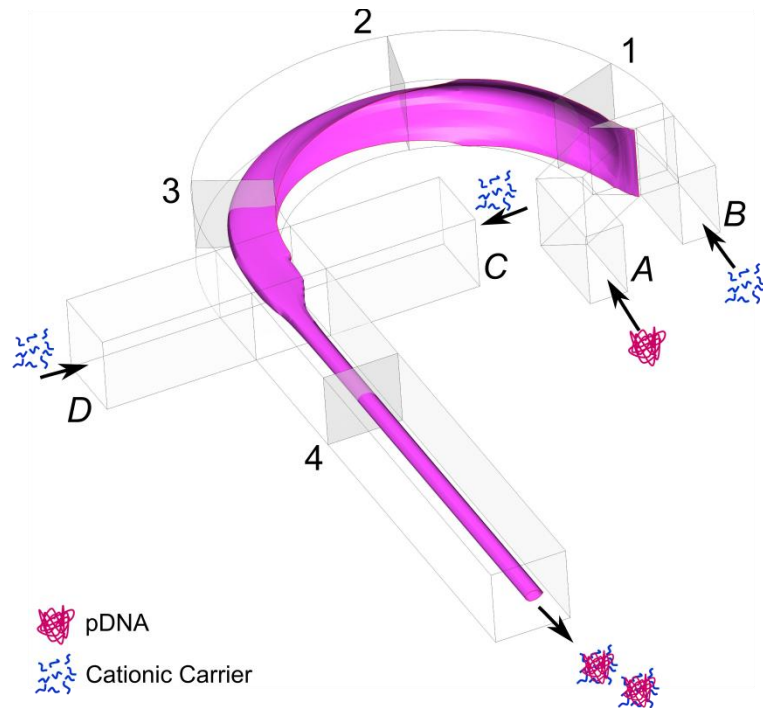


Figure 4-1 Schematic of the microfluidic device for polyplex synthesis by 3D-HF. The DNA solution is injected through inlet A, while the polymer solution is injected from the inlet B, C, and D.

## **4.2 Materials and Methods**

The materials information and details about device fabrication, bulk mixing synthesis, cell culture, transfection and characterization are the same as described in Sec 3.2. Here I will only present the details about polyplexes synthesis in the 3D-HF microfluidic reactor and computational simulation.

### **4.2.1 Polyplexes Synthesis in the 3D-HF Microfluidic Reactor**

To prepare the polyplexes by 3D-HF, the DNA stock solution and the turbofect transfection reagent were diluted in Opti-MEM Reduced-Serum Medium to 13.2  $\mu\text{g/mL}$  and 13.2  $\mu\text{L/mL}$ , respectively. As demonstrated in Fig. 4-1, the DNA solution was focused after injected through inlet A. The polymer solution was injected from inlets B, C, and D. Additionally, a very long channel length was used to allow a longer residence time and ensured completion of reaction within the microfluidic reactor. The polyplexes were collected at the outlet directly without any further purification or separation. Several flow rates were tested for optimization of operation parameters based on the size of the synthesized polyplexes, while keeping the flow rate ratio between inlets A:B:C:D as 3:4:1:1. The optimized flow rate was then used to synthesize polyplexes with the introduction of acoustic perturbation. The voltage and frequency applied to the piezoelectric transducer were 20 V<sub>pp</sub> and 55 Hz.

#### 4.2.2 Computational Simulation

The concentration distribution of DNA solution was simulated at different flow rates using a commercial CFD simulation software (CFD-ACE+, ESI-CFD), by assuming the diffusion coefficient of the 390 kD pGFP as  $0.5 \times 10^{-12} \text{ m}^2/\text{s}$  and the initial concentration as  $1.905 \times 10^{-9} \text{ M}$  [27]. The simulation did not consider the reaction between the DNA and polymer.

### 4.3 Results and Discussion

#### 4.3.1 Optimization of Operation Parameters

Several flow rates were tested for optimization based on the size of the synthesized polyplexes, while keeping the flow rate ratio between inlets A:B:C:D as 3:4:1:1. The computational fluid dynamics (CFD) simulation of the experimental parameters show the confinement of the DNA solution in both horizontal and vertical directions at various flow rates (Fig. 4-2). As the flow rate increases, the size of the highly concentrated DNA region decreases, and the region of lower DNA concentration increases, indicating the enhancement of mixing.

The size ( $Z$  average diameter,  $Z_{ave}$ ) and polydispersity index (PdI) of polyplexes synthesized with different flow rates were measured (Fig. 4-3). This experimental result shows the expected trend that the size of the polyplexes decreases with the increase in flow rate (Fig. 4-3 a). However, as the total flow rate increases from 270  $\mu\text{L}/\text{min}$  to 360  $\mu\text{L}/\text{min}$ , the decrease in particle size is less than 30 nm, and further increase in flow rate

might cause leakage of the microfluidic channel. Therefore, the total flow rate of 360  $\mu\text{L}/\text{min}$  was used as the optimized flow rate.

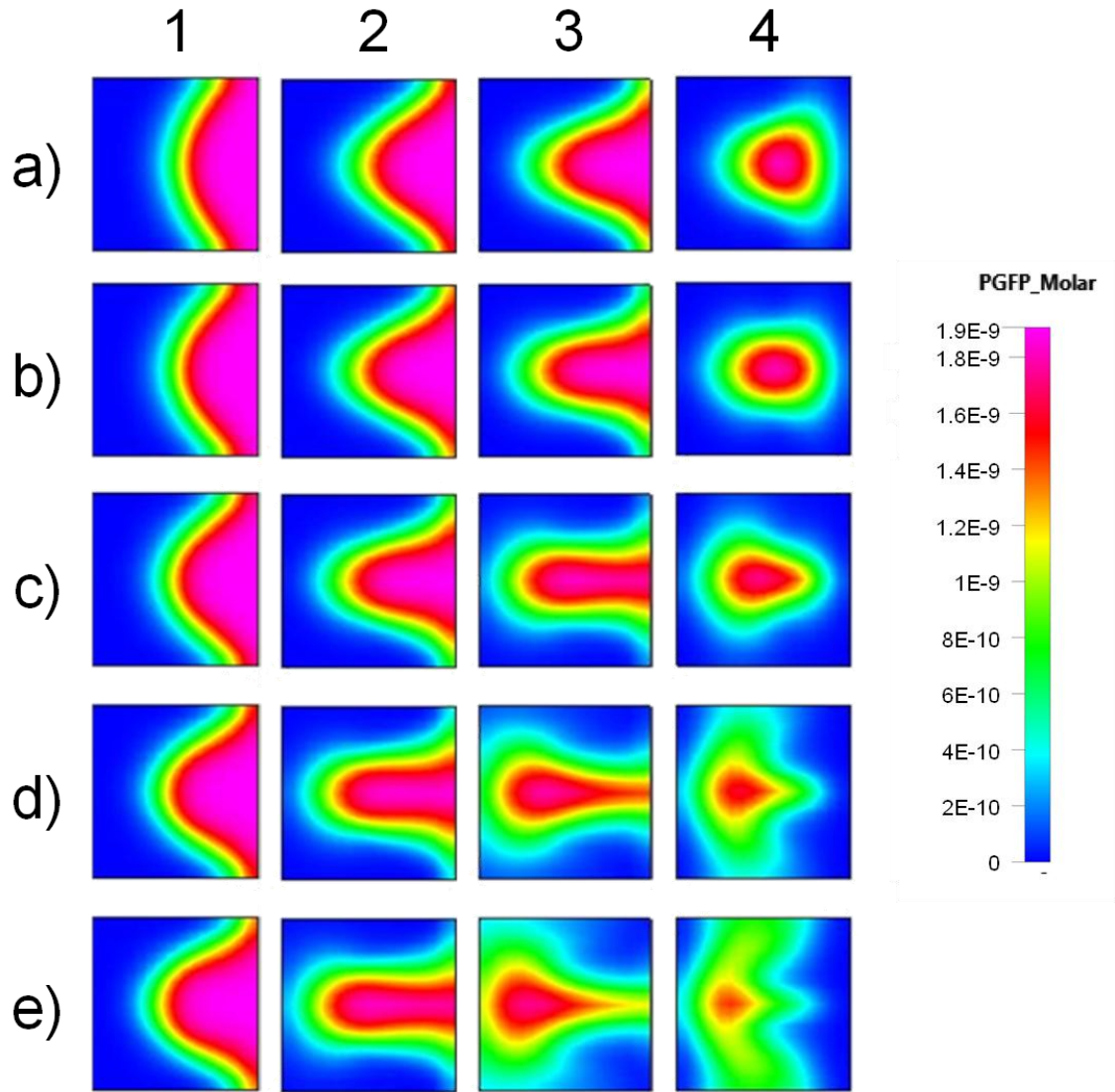


Figure 4-2 The DNA concentration distribution in cross-section areas at location 1, 2, 3, and 4 in Figure 1 at different flow rates. The total flow rate is (a) 90  $\mu\text{L}/\text{min}$ , (b) 120  $\mu\text{L}/\text{min}$ , (c) 180  $\mu\text{L}/\text{min}$ , (d) 270  $\mu\text{L}/\text{min}$ , and (e) 360  $\mu\text{L}/\text{min}$ .

### 4.3.2 Reducing Polyplex Size by 3D-HF and Acoustic Perturbation

At the total flow rate of 360  $\mu\text{L}/\text{min}$ , the 3D-HF-prepared polyplexes show smaller size compared to those prepared by the bulk mixing method ( $Z_{ave,3D} = 263.0 \text{ nm}$  versus  $Z_{ave,bulk} = 419.1 \text{ nm}$ ), while the size distribution is comparable in both conditions ( $PDI_{3D} = 0.131$  versus  $PDI_{bulk} = 0.142$ ,  $n = 3$ ,  $p = 0.789$ ). Besides 3D-HF, as discussed in Chapter 2, the acoustic streaming can further enhance the mixing performance [28]. Fig. 4-3 b shows the size distribution of polyplexes prepared by bulk mixing, 3D-HF, and acoustic-assisted 3D-HF. As expected, introduction of acoustic perturbation further decreases the particle size and polydispersity index ( $Z_{ave,3D,acoustic} = 200.0 \text{ nm}$ ,  $PDI_{3D,acoustic} = 0.067$ ).

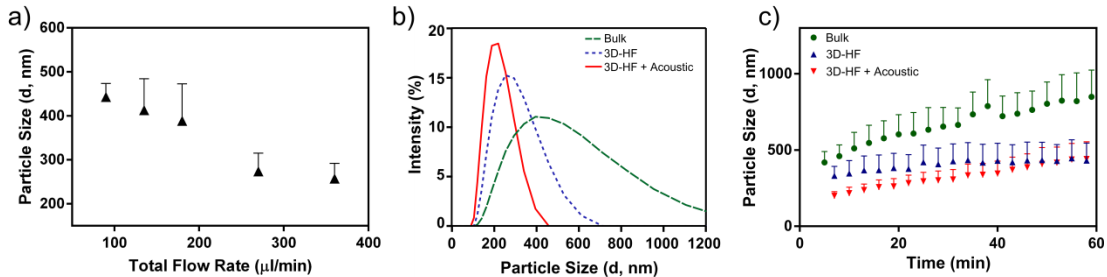


Figure 4-3 Comparison of polyplexes prepared by bulk mixing and 3D-HF. (a) Size of polyplexes as a function of flow rate. (b) Intensity-based size distribution ( $Z_{ave,3D,acoustic} = 200.0 \text{ nm}$ ,  $Z_{ave,3D} = 263.0 \text{ nm}$ ,  $Z_{ave,bulk} = 419.1 \text{ nm}$ ;  $PDI_{3D,acoustic} = 0.067$ ,  $PDI_{3D} = 0.131$ ,  $PDI_{bulk} = 0.142$ ); (c) aggregation kinetics.

### 4.3.3 Aggregation Kinetic Studies

As discussed in Chapter 3, aside from heterogeneity in size, significant aggregation is often observed in polyplexes synthesized by the bulk mixing method [29].

Fig. 4-3 c shows the comparison of the aggregation kinetics of polyplexes prepared by the bulk mixing method and 3D-HF with and without acoustic perturbation. This result suggests that 3D HF method can produce more stable particles without any post-processing. The aggregation kinetics over 4 hours (the time required for transfection) shows the same trend (Fig. 4-4). The improved size uniformity and slower aggregation rate exhibited by polyplexes prepared with 3D-HF, especially with acoustic perturbation, is most likely due to enhanced mixing.

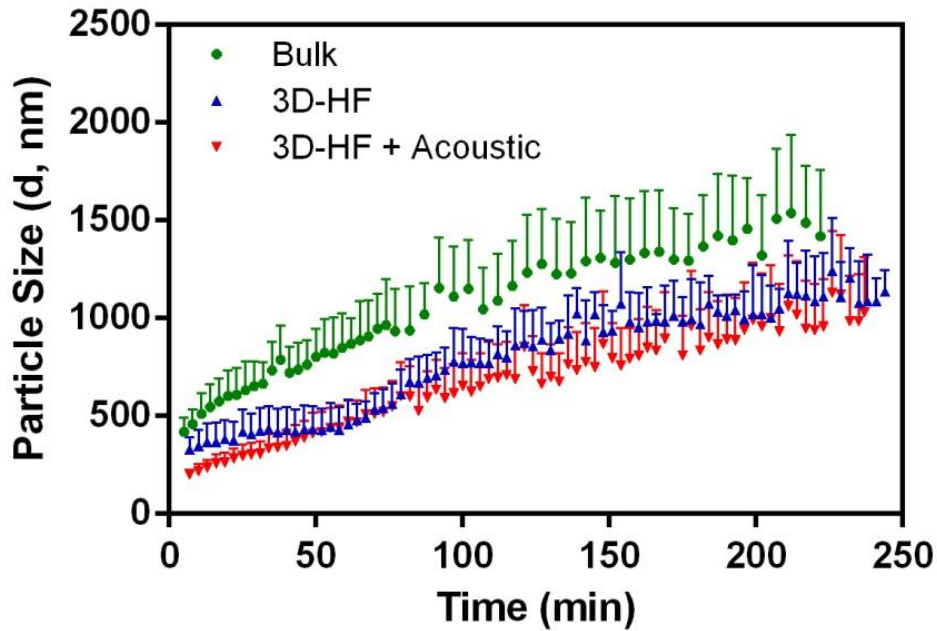


Figure 4-4 Aggregation kinetics over 4 hours after synthesis.

#### 4.3.4 Estimation of Shear Rate and Temperature Increment

Even though the mixing performance can be enhanced by increasing the flow rate and external acoustic field, the potential degradation of DNA becomes a concern due to

the increased shear stress and introduction of acoustic power. High shear rate (for example, 40 milliseconds of shear rate at  $3.5 \times 10^5/\text{s}$ ) [30] or long time of relatively low shear rate ( $\sim 100$  seconds of shear rate at  $2.1 \times 10^4/\text{s}$ ) [31] may break the phosphodiester backbone of DNA and physically fragment DNA into small pieces [30–32]. Ultrasound may also fragment DNA *via* mechanical or thermal degradation [33]. Degradation of DNA by these mechanisms will negate the benefits of the proposed acoustic-assisted 3D-HF method for polyplex synthesis.

I first evaluated the shear stress under this experimental setting, based on the applied flow rate and time of operation. At the highest flow rate of  $360 \mu\text{L}/\text{min}$ , the residence time of the DNA in the microfluidic channel is shorter than 400 milliseconds. The velocity distribution was simulated (Fig. 4-5). The shear rate ( $\dot{\gamma}$ ) is calculated as  $\dot{\gamma} = \partial v / \partial h$ , where  $v$  is the velocity of the fluid and  $h$  is the distance from the channel wall. The maximum shear rate is  $8.1 \times 10^4/\text{s}$  near the channel wall, and the shear rate decreases from the wall to the center of the channel, where the DNA condensation takes place. The relatively low shear rate [30] and the short time interval [31] suggest that DNA degradation due to shear stress is negligible in these experiments.

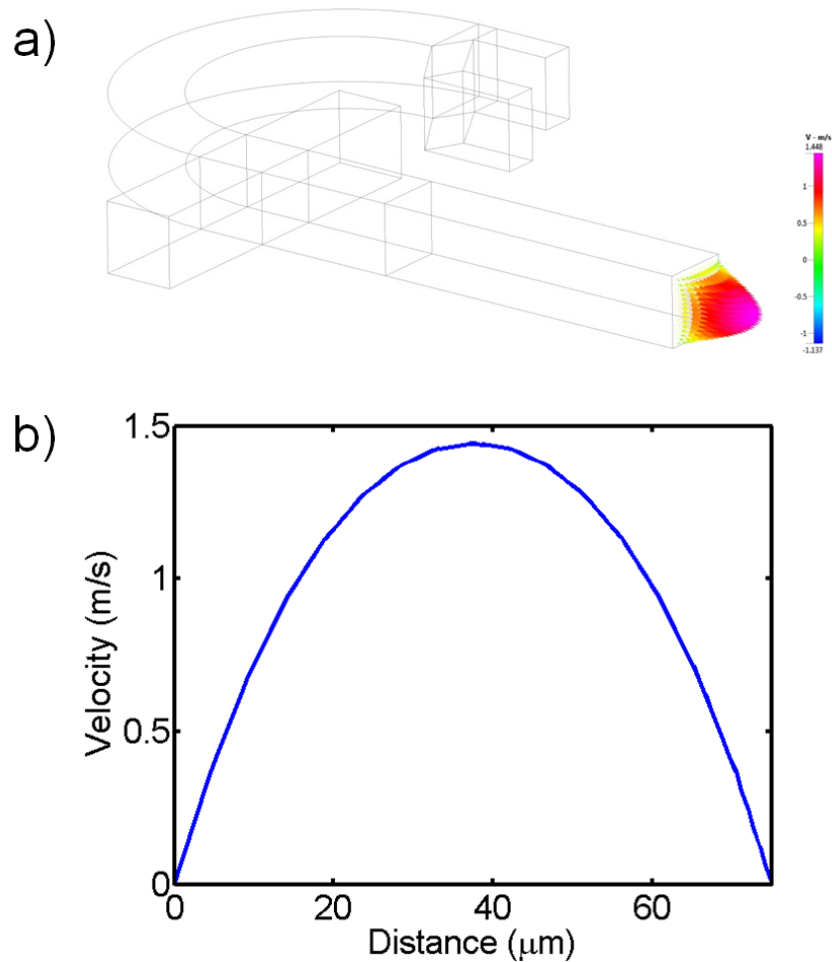


Figure 4-5 (a) The velocity distribution of fluid velocity in a cross-section at a total flow rate of 360  $\mu\text{L}/\text{min}$ . (b) The velocity distribution at the center line in the cross-section in (a).

The two main mechanisms of DNA degradation by an acoustic field are cavitation and direct mechanical or thermal degradation. When acoustic pressure is in the order of one atmosphere or higher, gas bubbles appear and oscillate vigorously, resulting in mechanical stress that can be several orders of magnitude higher than that in fluid without bubble [35]. However, acoustic cavitation is negligible in my experiments because no bubble was observed due to the extremely low acoustic pressure ( $< 100 \text{ Pa}$ ). Another

concern is the heat generated by the piezoelectric transducer, which was made of Lead zirconium titanate (PZT), and the absorption of acoustic energy in the fluid. This has been an issue extensively investigated in other ultrasound applications, and the relationship between heat generation in PZT materials and acoustic frequency is already known [36]. The low frequency (55 Hz) applied in my experiments produced temperature increase less than 1 °C. As an analogy, this low frequency is similar to the frequency of a normal bench-top shaker. It should not damage the pDNA, as confirmed through an agarose gel electrophoresis experiment (Fig. 4-6), which shows that 3D-HF with acoustic perturbation causes no significant DNA fragmentation or degradation. In summary, the external acoustic perturbation provided additional active mixing in the proposed 3D-HF mechanism, while maintaining the integrity of the DNA.

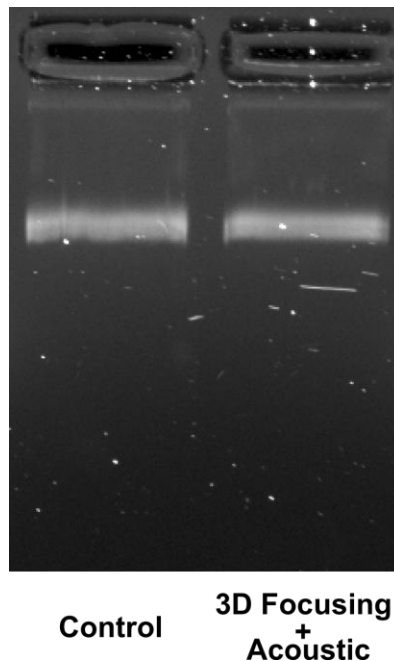


Figure 4-6 Gel electrophoresis experiment result. There is no noticeable difference between the control sample and the sample that experienced 3D-HF and acoustic perturbation, indicating the integrity of DNA after exposure to flow conditions in acoustic-assisted 3D-HF microfluidic reactors.

#### 4.3.5 Biological Performance of the Synthesized Polyplexes

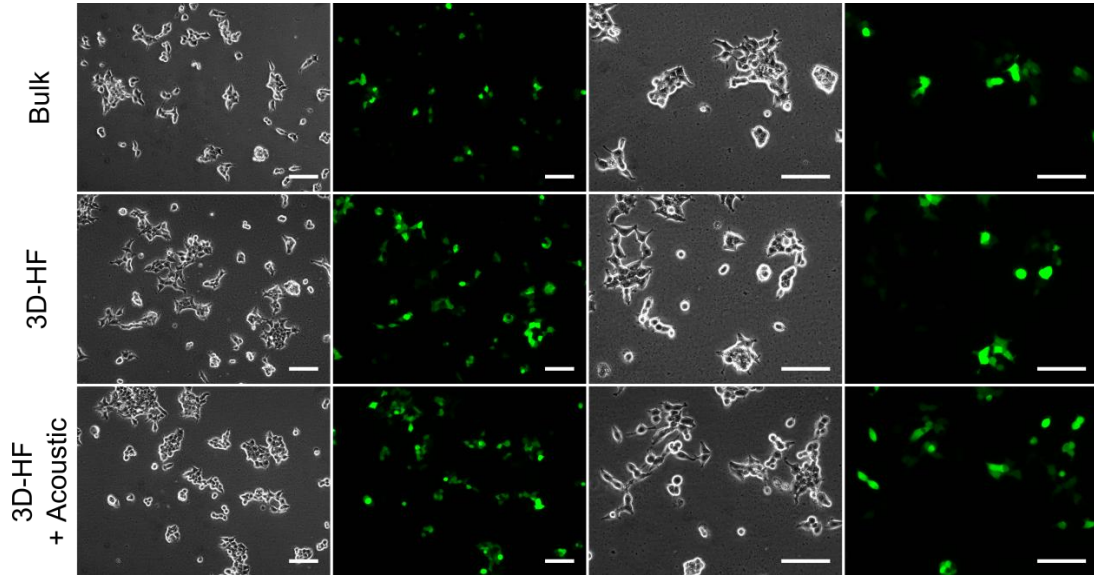


Figure 4-7 Microscopic observation of GFP transfection. At 24 h post-transfection, the human embryonic kidney (HEK293T) cells transfected by turbofect polyplexes were examined by fluorescence microscopy. Visually, the cells show comparable transfection efficiency in all cases. Scale bar = 100  $\mu$ m.

Fig. 4-7 and Fig. 4-8 compare the biological performance of the polyplexes prepared by the bulk mixing method and 3D-HF with and without acoustic perturbation. The reporter DNA vectors pmax-GFP encoding green fluorescent protein (GFP) was used for polyplexes synthesis. Qualitatively, the cells show comparable transfection efficiency in all cases (Fig. 4-7). Quantitatively, 3D-HF polyplexes prepared with or without acoustic perturbation achieve ~75% transfection compared to the 60% by bulk-mixed polyplexes (Fig. 4-8 g). The improvement in transfection efficiency again confirms that there is no obvious DNA damage during polyplexes synthesis by 3D-HF with and without acoustic perturbation.

Similar distributions in forward scatter/side scatter (FSC/SSC) plots (Fig. 4-8 a-c) suggest that the cells maintained comparable morphologies after transfection with polyplexes prepared in all cases. Further investigation show that polyplexes prepared by 3D-HF induce less cell death (PI+) and apoptosis (PI-, Annexin V+) [1] than polyplexes prepared by the bulk mixing method (Fig. 4-8 d-f), which is also shown in Fig. 4-8 h.

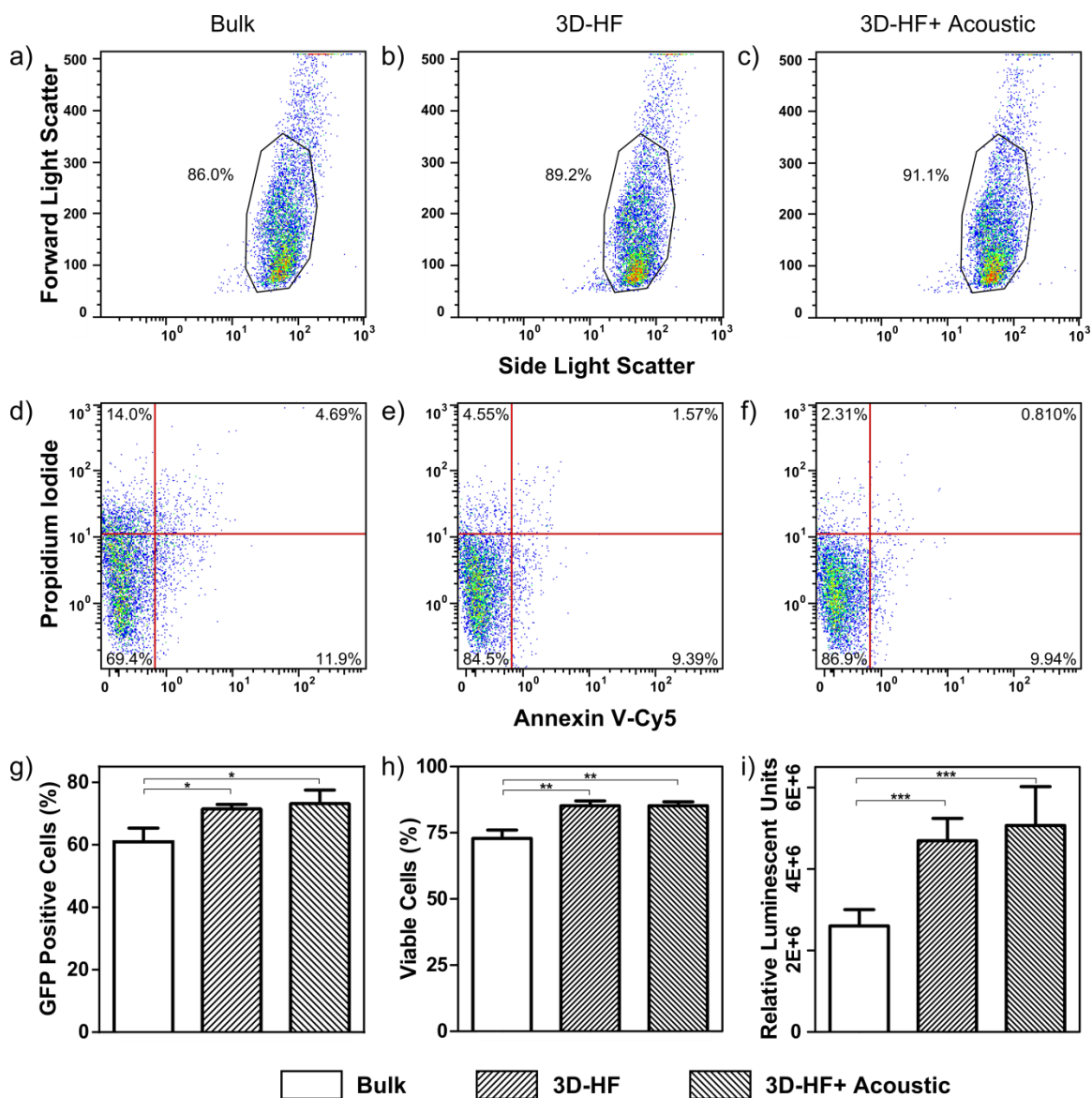


Figure 4-8 Quantification of transfection efficiency and cytotoxicity. (a-c) The FSC/SSC plots of the cells after transfected with polyplexes synthesized by bulk mixing method, and 3D-HF method without and with acoustic perturbation. (d-f) Bivariate plots to quantitatively evaluate cytotoxicity of polyplexes synthesized by bulk mixing method, and 3D-HF method without and with acoustic perturbation. (g) Quantification of GFP expression level ( $n = 3$ ).  $*p < 0.026$ . (h) Quantification of cell viability. ( $n = 3$ ).  $**p < 0.0042$  (i) Quantification of luciferase assay ( $n = 3$ ).  $***p < 0.0004$ . (Unpaired  $t$  test, CI 95%, two-tailed  $p$ -value).

To complement the transfection parameter of percent cells transfected, I also measured the total gene expression level using the firefly luciferase (pLuc) reporter gene. The results are shown in Fig. 4-8 i. Consistent with the GFP-transfection results, polyplexes prepared by 3D-HF show two-fold greater luminescence intensity as compared to the bulk mixing case. No statistical significance is found between the luminescence intensity in 3D-HF cases with or without acoustic perturbation.

The acoustic-assisted 3D-HF method shows the ability to synthesize polyplexes with better control of physical properties, such as size and colloidal stability, over the traditional bulk mixing method. The throughput of 3H-HF method can also be improved through optimization of the device and flow parameters, or at the very least through integration of multiple 3D-HF devices in parallel for mass production of polyplexes [36,37].

#### 4.4 Conclusion

Polyplex synthesis using a 3D-HF method is demonstrated, along with external acoustic perturbation. The polyplexes prepared by this 3D-HF method show smaller size, slower aggregation rate, higher transfection efficiency, and lower cytotoxicity compared to the ones prepared by the bulk mixing method. Furthermore, acoustic perturbation can

further decrease the particle size. The 3D-HF method can produce high-quality polyplexes in an operator-independent, simple, and scalable manner. Compared with the bubble based microfluidic reactor described in Chapter 3, 3D-HF method requires no gas injection during the synthesis, which simplifies and also miniaturizes the device, making it possible for on-site and on-demand biomedicine synthesis.

## References

- [1] Moghimi, S.M., Symonds, P., Murray, J.C., Hunter, A.C., Debska, G. and Szweczyk, A., "A two-stage poly(ethylenimine)-mediated cytotoxicity: Implications for gene transfer/therapy," *Molecular Therapy*, **11**, 990–995 (2005)
- [2] Chang, Z., Serra, C.A., Bouquey, M., Kraus, I., Li, S. and Köhler, J.M., "Multiscale materials from microcontinuous-flow synthesis: ZnO and Au nanoparticle-filled uniform and homogeneous polymer microbeads," *Nanotechnology*, **21**, 15605 (2010)
- [3] Chang, C.C., Huang, Z.X. and Yang, R.J., "Three-dimensional hydrodynamic focusing in two-layer polydimethylsiloxane (PDMS) microchannels," *Journal of Micromechanics and Microengineering*, **17**, 1479–1486 (2007)
- [4] Kim, J., Hwang, I., Britain, D., Chung, T.D., Sun, Y. and Kim, D.H., "Microfluidic approaches for gene delivery and gene therapy," *Lab on a Chip*, **11**, 3941–3948 (2011)
- [5] Koh, C.G., Zhang, X., Liu, S., Golan, S., Yu, B., Yang, X., Guan, J., Jin, Y., Talmon, Y., Muthusamy, N., Chan, K.K., Byrd, J.C., Lee, R.J., Marcucci, G. and Lee, L.J., "Delivery of antisense oligodeoxyribonucleotide lipopolyplex nanoparticles assembled by microfluidic hydrodynamic focusing," *Journal of Controlled Release*, **141**, 62–69 (2010)
- [6] Ismagilov, R.F., Stroock, A.D., Kenis, P.J.A., Whitesides, G. and Stone, H.A., "Experimental and theoretical scaling laws for transverse diffusive broadening in two-phase laminar flows in microchannels," *Applied Physics Letters*, **76**, 2376 (2000)
- [7] Zhao, C.-X., He, L., Qiao, S.Z. and Middelberg, A.P.J., "Nanoparticle synthesis in microreactors," *Chemical Engineering Science*, **66**, 1463–1479 (2011)
- [8] Sundararajan, N., Pio, M.S., Lee, L.P. and Berlin, A.A., "Three-dimensional hydrodynamic focusing in polydimethylsiloxane (PDMS) microchannels," *Microelectromechanical Systems*, **13**, 559–567 (2004)
- [9] Wolff, A., Perch-Nielsen, I.R., Larsen, U.D., Friis, P., Goranovic, G., Poulsen, C.R., Kutter, J.P. and Telleman, P., "Integrating advanced functionality in a microfabricated high-throughput fluorescent-activated cell sorter," *Lab on a Chip*, **3**, 22–27 (2003)

- [10] Mao, X., Nawaz, A.A., Lin, S.-C.S., Lapsley, M.I., Zhao, Y., McCoy, J.P., El-Deiry, W.S. and Huang, T.J., "*An integrated, multiparametric flow cytometry chip using "microfluidic drifting" based three-dimensional hydrodynamic focusing,*" *Biomicrofluidics*, **6**, 24113 (2012)
- [11] Huang, S.-H., Tan, W.-H., Tseng, F.-G. and Takeuchi, S., "*A monolithically three-dimensional flow-focusing device for formation of single/double emulsions in closed/open microfluidic systems,*" *Journal of Micromechanics and Microengineering*, **16**, 2336-2344 (2006)
- [12] Mao, X., Lin, S.-C.S., Dong, C. and Huang, T.J., "*Single-layer planar on-chip flow cytometer using microfluidic drifting based three-dimensional (3D) hydrodynamic focusing,*" *Lab on a Chip*, **9**, 1583–1589 (2009)
- [13] Mao, X., Waldeisen, J.R. and Huang, T.J., "*"Microfluidic drifting"---implementing three-dimensional hydrodynamic focusing with a single-layer planar microfluidic device,*" *Lab on a Chip*, **7**, 1260–1262 (2007)
- [14] Mao, X. and Huang, T.J., "*Microfluidic diagnostics for the developing world,*" *Lab on a Chip*, **12**, 1412–1416 (2012)
- [15] Rhee, M., Valencia, P.M., Rodriguez, M.I., Langer, R., Farokhzad, O.C. and Karnik, R., "*Synthesis of size-tunable polymeric nanoparticles enabled by 3D hydrodynamic flow focusing in single-layer microchannels.,*" *Advanced Materials*, **23**, H79–H83 (2011)
- [16] Scott, R., Sethu, P. and Harnett, C.K., "*Three-dimensional hydrodynamic focusing in a microfluidic Coulter counter,*" *Review of Scientific Instruments*, **79**, 046104 (2008)
- [17] Knight, J.B., Vishwanath, A., Brody, J.P. and Austin, R.H., "*Hydrodynamic focusing on a silicon chip : mixing nanoliters in microseconds,*" *Physical Review Letters*, **80**, 3863–3866 (1998)
- [18] Oberti, S., Neild, A. and Ng, T.W., "*Microfluidic mixing under low frequency vibration,*" *Lab on a Chip*, **9**, 1435–1438 (2009)
- [19] Ahmed, D., Mao, X.L., Juluri, B.K. and Huang, T.J., "*A fast microfluidic mixer based on acoustically driven sidewall-trapped microbubbles,*" *Microfluidics and Nanofluidics*, **7**, 727–731 (2009)
- [20] Ahmed, D., Mao, X.L., Shi, J.J., Juluri, B.K. and Huang, T.J., "*A millisecond micromixer via single-bubble-based acoustic streaming,*" *Lab on a Chip*, **9**, 2738–2741 (2009)

- [21] Huang, P.H., Lapsley, M.I., Ahmed, D., Chen, Y.C., Wang, L. and Huang, T.J., "A single-layer, planar, optofluidic switch powered by acoustically driven, oscillating microbubbles," *Applied Physics Letters*, **101**, 14 (2012)
- [22] Xie, Y.L., Ahmed, D., Lapsley, M.I., Lin, S.C.S., Nawaz, A.A., Wang, L. and Huang, T.J., "Single-shot characterization of enzymatic reaction constants  $K_m$  and  $k_{cat}$  by an acoustic-driven, bubble-based fast micromixer," *Analytical Chemistry*, **84**, 7495–7501 (2012)
- [23] Ahmed, D., Chan, C.Y., Lin, S.C.S., Muddana, H.S., Nama, N., Benkovic, S.J. and Huang, T.J., "Tunable, pulsatile chemical gradient generation via acoustically driven oscillating bubbles," *Lab on a Chip*, **13**, 328–331 (2013)
- [24] Ding, X., Lin, S.-C.S., Lapsley, M.I., Li, S., Guo, X., Chan, C.Y., Chiang, I.-K., Wang, L., McCoy, J.P. and Huang, T.J., "Standing surface acoustic wave (SSAW) based multichannel cell sorting," *Lab on a Chip*, **12**, 4228–4231 (2012)
- [25] Ding, X., Li, P., Lin, S.-C.S., Stratton, Z.S., Nama, N., Guo, F., Slotcavage, D., Mao, X., Shi, J. and Costanzo, F., "Surface acoustic wave microfluidics," *Lab on a Chip*, **13**, 3626–3649 (2013)
- [26] Shi, J., Mao, X., Ahmed, D., Colletti, A. and Huang, T.J., "Focusing microparticles in a microfluidic channel with standing surface acoustic waves (SSAW)," *Lab on a Chip*, **8**, 221–223 (2008)
- [27] Prazeres, D.M.F., "Prediction of diffusion coefficients of plasmids," *Biotechnology and Bioengineering*, **99**, 1040–1044 (2008)
- [28] Zhu, X. and Kim, E.S., "Microfluidic motion generation with acoustic waves," *Sensors and Actuators A: Physical*, **66**, 355–360 (1998)
- [29] Hunter, R.J., *Introduction to Modern Colloid Science*, Oxford University Press, New York, NY (1994)
- [30] Levy, M.S., Collins, I.J., Yim, S.S., Ward, J.M., Titchener-Hooker, N., Shamlou, P.A. and Dunnill, P., "Effect of shear on plasmid DNA in solution," *Bioprocess Engineering*, **20**, 7–13 (1999)
- [31] Zhang, H., Kong, S., Booth, A., Boushaba, R., Levy, M.S. and Hoare, M., "Prediction of shear damage of plasmid DNA in pump and centrifuge operations using an ultra scale-down device," *Biotechnology Progress*, **23**, 858–865 (2007)
- [32] Wu, M.L., Freitas, S.S., Monteiro, G.A., Prazeres, D.M.F. and Santos, J.A.L., "Stabilization of naked and condensed plasmid DNA against degradation induced

- by ultrasounds and high-shear vortices,"* Biotechnology and Applied Biochemistry, **53**, 237–246 (2009)
- [33] Elsner, H.I. and Lindblad, E.B., "*Ultrasonic degradation of DNA*," DNA, **8**, 697–701 (1989)
- [34] Carstensen, E.L., "*Acoustic cavitation and the safety of diagnostic ultrasound*," Ultrasound in Medicine and Biology, **13**, 597–606 (1987)
- [35] Zheng, J.H., Takahashi, S., Yoshikawa, S., Uchino, K. and deVries, J.W.C., "*Heat generation in multilayer piezoelectric actuators*," Journal of the American Ceramic Society, **79**, 3193–3198 (1996)
- [36] Kang, X., Luo, C., Wei, Q., Xiong, C., Chen, Q., Chen, Y. and Ouyang, Q., "*Mass production of highly monodisperse polymeric nanoparticles by parallel flow focusing system*," Microfluidics and Nanofluidics, **15**, 337-345 (2013)
- [37] Nisisako, T. and Torii, T., "*Microfluidic large-scale integration on a chip for mass production of monodisperse droplets and particles*," Lab on a Chip, **8**, 287–293 (2008)

## **Chapter 5 Shape Tunable Synthesis of Hybrid Nanomaterials by Three Dimensional Hydrodynamic Focusing Method**

Previous chapters presented two designs to enhance mixing in microfluidic reactors and the polyplexes synthesis by using these two designs. Compared with the bubble based microfluidic reactor, it is easier to operate the 3D-HF microfluidic reactors since no gas is involved, which enables the simplification of operation and miniaturization of the device.

The chemical concentration distribution in the bubble based microfluidic mixer is uniform since it enhances mixing in the whole channel, so it is easy to predict the reaction conditions. In contrast, the chemical concentration distributions in the 3D-HF microfluidic reactors are dependent on the flow conditions (*e.g.*, flow rate and flow rate ratio). The variation of the chemical concentration distribution requires more effort to understand the reaction condition within the 3D-HF microfluidic reactors. At the same time, it also provides a new way to precisely control the reaction condition. This chapter presents the study on the chemical concentration distribution within the 3D-HF microfluidic reactor via the synthesis of tetrathiafulvalene-Au (TTF-Au) hybrid materials. The TTF-Au hybrid material synthesis process is sensitive to the feed molar ratio between the reagents. As a result, while the flow condition changes, the synthesized materials show different morphologies. Therefore, the chemical concentration distribution within the microfluidic device can be understood by studying the morphology changes of the synthesized materials.

## 5.1 Introduction

Nanomaterials have attracted great research interests for their special chemical and physical properties and applications in catalysis [1], photonics [2,3], imaging [2,3], nanoelectronics [4], sensors and biomedicine [5]. Their intrinsic properties are strongly influenced by the elemental composition, size and the shape [1,3,6–8]. Therefore, significant effort has been devoted to synthesize nanomaterials with well-controlled shapes. For example, noble metal nanostructures in the shape of rods [9], wires [10], belts [11], cubes [12], polyhedral [13], plates [14,15], stars [16] and dendrites [17,18] have been produced recently. Various synthetic methods have been proposed for fabricating nanomaterials with well-defined shapes, such as wet chemical methods [2], nanolithographic techniques [19] and template based synthesis [20]. For practical applications, it is of great importance to synthesize nanomaterials in large quantities and at reasonably low cost. Solution synthetic methods have been used broadly because of their simplicity and high throughput. Recently, microfluidic devices amenable to automated operation have attracted increasing interest due to their ability to minimize human factors. The laminar flow conditions in microfluidic reactors can confine the reaction zone (the region where reaction occurs) to the interface between two reagent flows [21]. Therefore, the reaction conditions (*e.g.*, reagent ratio, flow rate, ionic concentration) can be finely tuned, leading to highly controllable parameterization throughout the synthesis process.

Hydrodynamic focusing has been used to enhance mixing within the reaction zone in microfluidic reactors. Two-dimensional hydrodynamic focusing (2D-HF)

method, which focuses the central solution in the horizontal plane only, has been used to synthesize nanomaterials [22]. However, in the case of 2D-HF, the profiles of the reagent streams still show 3D distributions, which can be influenced by the channel shape and flow conditions [23]. Compared with 2D-HF, 3D-HF can further reduce the reaction volume and compress the center stream in both horizontal and vertical directions, enabling better control of the reaction conditions within the reaction zone.

While most reported nanomaterials synthesis by hydrodynamic focusing methods has centered on the improved uniformity of products, the possibility of size and shape tenability has received limited attention. Due to the great influence of shape in nanomaterials properties and behavior, synthesis of nanomaterials with tunable morphologies is of critical importance to the field of functional nanomaterials.

Tetrathiafulvalene (TTF) has been widely used for synthesizing organic conductors [24,25]. Different TTF-based complexes have been synthesized by conventional bulk mixing and microfluidic synthesis methods. This chapter presents an investigation on how the flow conditions modulate the shape of TTF-Au hybrid nanomaterials within a 3D-HF device.

The 3D-HF device for TTF-Au hybrid materials synthesis is shown in Fig. 5-1. The microfluidic device consists of four inlet channels and one outlet channel. Fluid injected from inlet A is firstly focused vertically by the vertical sheath flow from inlet B. Then the horizontal sheath flow from inlet C and D finally compress the fluid from inlet A to the center of the channel.

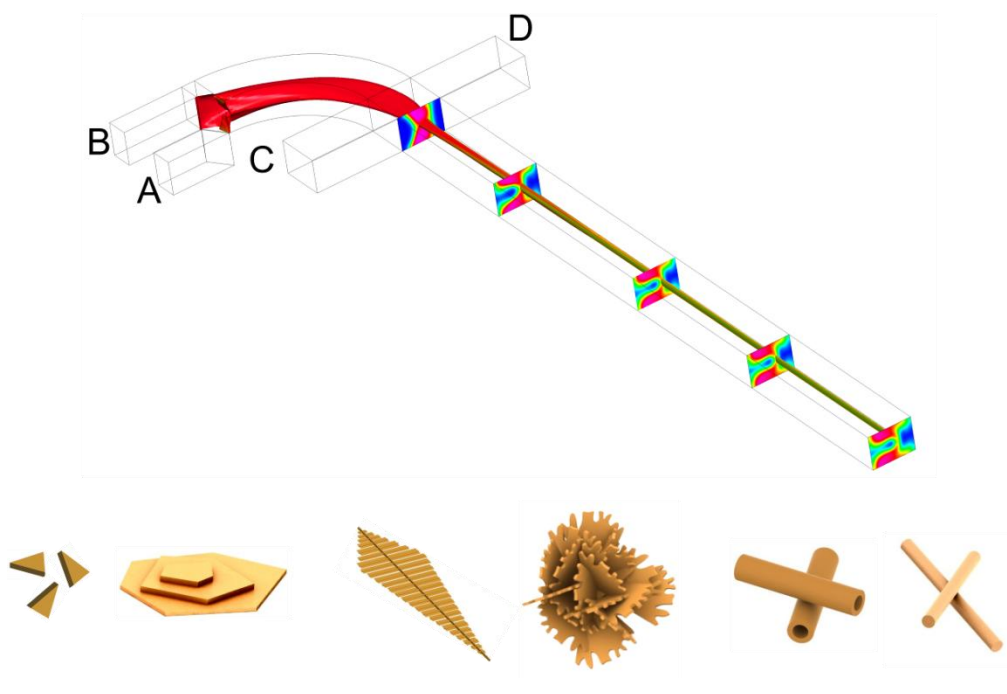


Figure 5-1 Schematic of the microfluidic device for hybrid nanomaterials synthesis by 3D-HF. The iso-curve shows the focusing of reagent A and the slices show the concentration distribution of reagent B. While keeping the flow rate of reagent A and B the same and changing the flow rate of buffer C and D, nanomaterials with different shapes can be synthesized.

## 5.2 Materials and Methods

The details about the device fabrication are the same as described in Sec 3.2. Therefore, only the information about materials and details about experiments are presented here.

### 5.2.1 Materials

Tetrathiafulvalene (TTF) and hydrogen tetrachloroaurate ( $\text{HAuCl}_4$ ) were purchased from Sigma-Aldrich. The reagent solutions were prepared by dissolving TTF

in acetonitrile at the concentration of 1.1 mM and  $\text{HAuCl}_4$  in acetonitrile at the concentration of 0.27 mM. All materials were used directly without any further treatment.

### **5.2.2 Synthesis of TTF-Au Hybrid Materials in 3D-HF Microfluidic Reactors**

The 3D-HF microfluidic reactor was connected to syringes *via* tubing, and the flow rate was controlled by the neMESYS syringe pump system (Cetoni GmbH). Two groups of experiments were carried out. In the first group of experiments, TTF solution was injected from inlet A at flow rate of 30  $\mu\text{L}/\text{min}$ , and  $\text{HAuCl}_4$  solution was injected from inlet B at flow rates of 370  $\mu\text{L}/\text{min}$ . Acetonitrile was injected from inlet C and D as buffer solutions. In the second group of experiments,  $\text{HAuCl}_4$  solution was injected from inlet A and TTF solution from inlet B at flow rates of 30  $\mu\text{L}/\text{min}$  and 370  $\mu\text{L}/\text{min}$ , respectively. The resultant solution was collected at the outlet into a centrifuge tube containing 1 mL acetonitrile solution. For each experiment, 0.3 mL of the resultant solution was collected.

### **5.2.3 Synthesis of TTF-Au Hybrid Materials by Bulk Mixing Method**

To prepare TTF-Au Materials by the bulk Mixing method, TTF solution at 1.1 mM and  $\text{HAuCl}_4$  solution at 0.27 mM were mixed at different molar ratio, while keeping the total volume as 0.5 mL. Vortexing was performed for 60 seconds after the reagents were added.

#### **5.2.4 Computational Simulation**

The concentration distributions of reagents were simulated at different flow conditions using commercial CFD simulation software (CFD-ACE+, ESI-CFD). The simulation did not consider the reaction between TTF and  $\text{HAuCl}_4$ .

#### **5.2.5 Characterization of the Synthesized Materials**

The transmission properties of the resultant solutions were measured immediately after collection using a spectrometer.

For SEM imaging, a droplet of each collected solution was dropped on a silicon wafer. After evaporation, the samples were observed by a field emission scanning electron microscope (FESEM).

For XRD sample preparation, silicon wafers were placed in a 50 mm diameter petridish containing 2 mL of resultant solution of each sample from bulk mixing experiments. The amount of solution was chosen to obtain enough powder after evaporation for XRD characterization.

### **5.3 Results and Discussion**

#### **5.3.1 Different Morphologies of TTF-Au Materials Prepared by 3D-HF method**

The flow rate ratio (FRR) is defined as the ratio between the total flow rate from inlets A and B to the total flow rate from inlets C and D, or  $\text{FRR} = (A+B):(C+D)$ . For the

first group of experiments, as shown in Fig. 5-2, as the FRR varies from 20 to 0.2, the morphologies of the synthesized materials experience changes through (a) branching aggregates consisting of irregularly aligned polyhedral crystals, (b) triangle or hexagonal shape, (c) multi-layered structures consisting of thin and flat layers, (d) two dimensional dendritic nanostructures, (e) flower-like aggregates consisting of thin, flat petals with holes and (f) coral-like aggregates consisting of fibers. In general, the size of the synthesized materials increases and the morphologies become more complex with the decrease in FRR.

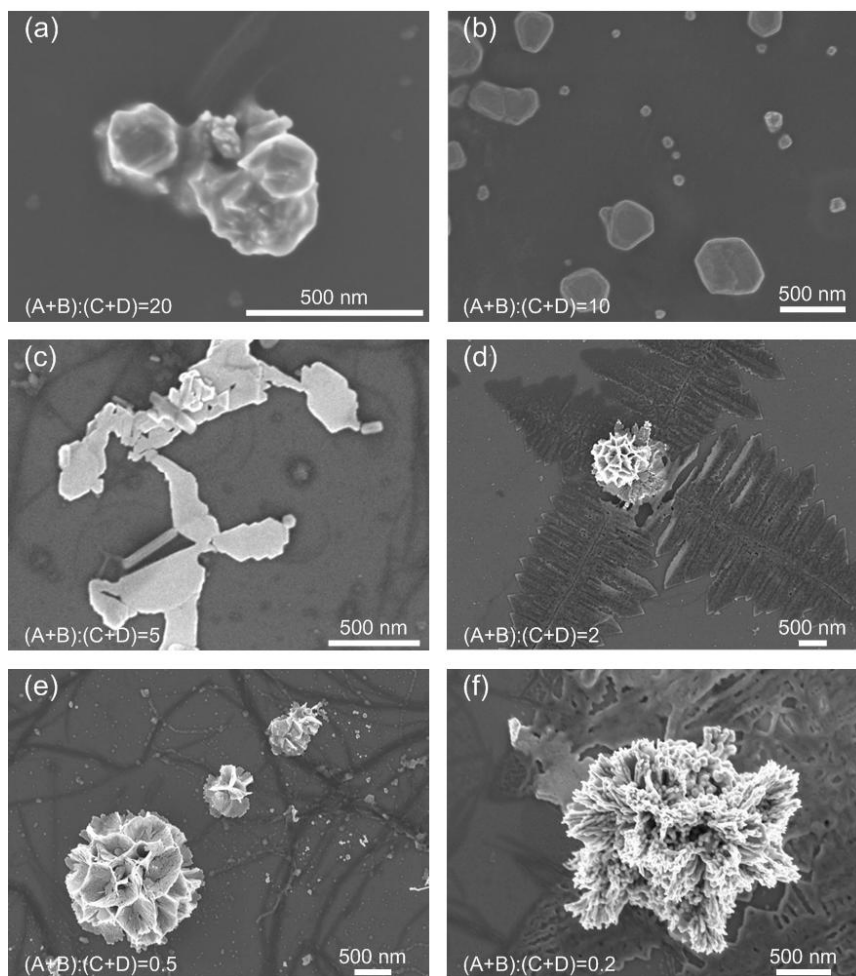


Figure 5-2 SEM images of nanomaterials prepared while using 1.1 mM TTF solution as reagent A and 0.27 mM H<sub>AuCl</sub><sub>4</sub> solution as reagent B. The flow rates were set to 30  $\mu\text{L}/\text{min}$  for TTF solution and 370  $\mu\text{L}/\text{min}$  for H<sub>AuCl</sub><sub>4</sub> solution, while the flow rate of buffer (ACN) was changed. As the  $\text{FRR} = (\text{A}+\text{B}):(\text{C}+\text{D})$  decreased, the morphologies of the synthesized nanomaterials experienced changes through (a) branching aggregates consisting of irregularly aligned polyhedral crystals, (b) triangle or hexagonal shape, (c) multi-layered structures consisting of thin and flat layers, (d) two dimensional dendritic nanostructures, (e) flower-like aggregates consisting of thin, flat petals and (f) coral-like aggregates consisting of fibers.

For the second group of experiments, as shown in Fig. 5-3, as the FRR increases from 0.2 to 20, the morphologies of the synthesized materials experience changes through (a) diamond shapes with apex angle of  $58^\circ$ , (b) long and hollow wires of several tens of micrometers, (c) wires of  $\sim 10$  micrometers and (d) wires of 3-5 micrometers. In general, the products show one-dimensional structures, whose sizes first increase and then decrease with the increase in FRR.

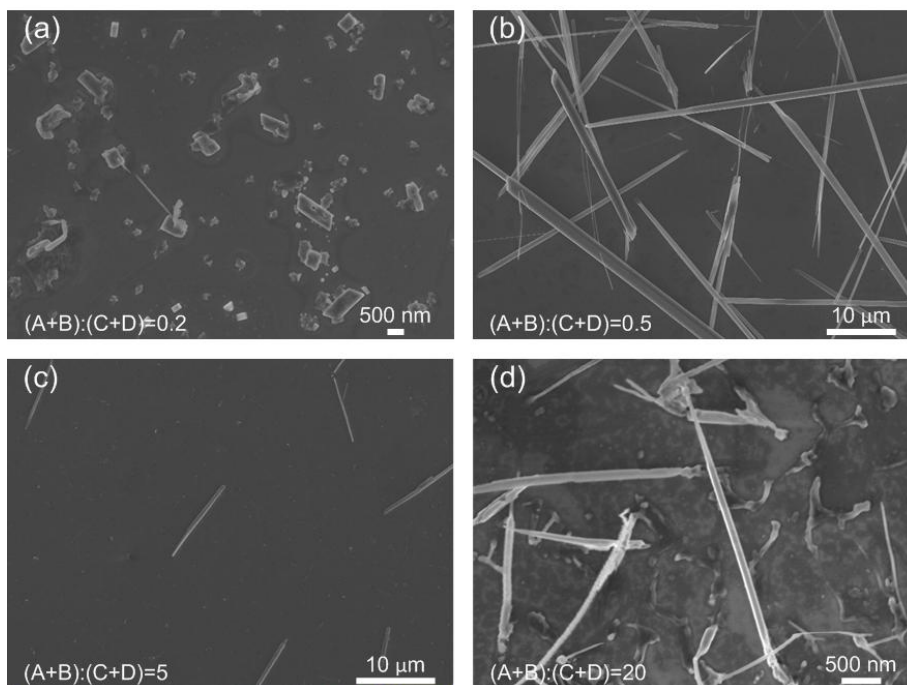


Figure 5-3 SEM images of nanomaterials prepared while using 0.27 mM H<sub>AuCl</sub><sub>4</sub> solution as reagent A and 1.1 mM TTF solution as reagent B. The flow rates were set to 30  $\mu\text{L}/\text{min}$  for H<sub>AuCl</sub><sub>4</sub> solution and 370  $\mu\text{L}/\text{min}$  for TTF solution, while the flow rate of buffer (ACN) was changed. As the  $\text{FRR} = (\text{A}+\text{B}):(\text{C}+\text{D})$  increased, the morphologies of the synthesized

nanomaterials experienced changes through (a) diamond shapes with apex angle of 58°; (b) long and hollow wires of several tens of micro meters, (c) wires of ~10 micrometers and (d) wires of 3-5 micrometers.

### **5.3.2 Possible Mechanism of Morphology Variation**

At the first glance, it is surprising that, variation of the buffer solution flow rate alone can lead to significant changes in morphologies of the synthesized materials. Here, the reactions are considered to have reached completion due to dilution as the product solution is ejected from the outlet channel into the acetonitrile solution. Thus the entire reaction takes place within the microfluidic channel, at the interface between the two reagent streams. One of the reagents is focused at the center of the channel, so the reaction zone is near the outer profile of the focused reagent stream. The change in FRR by varying the buffer solution flow rate affects both mechanical and chemical conditions within the microfluidic channel.

With the increase in FRR, the shear force at the interfaces of the co-flowing streams increases. Since it is known that shear force can affect the crystallization process by aligning or rotating molecules along the flow direction, increased shear force may lead to orientation-induced structures [26]. One might attribute the morphological changes in the experiments to the shear force changes. However, as shown in Fig. 5-2, the materials synthesized from the first group of experiments show dendritic and aggregates features without any directionality or alignment. This phenomenon suggests that the change in the mechanical conditions is not the main reason for the change in morphologies.

Change in FRR can also affect the chemical conditions, or the concentration distribution within the channel. Fig. 5-4 shows the computational fluid dynamic (CFD) simulation of the concentration distribution of the reagents after the introduction of buffer flows. As described in previous work [27,28], the reagent injected from inlet A drifts laterally to the opposite side of channel by the virtue of the Dean vortices caused by the high flow rate of the reagent injected from inlet B, resulting in vertical focusing. Reagent A becomes wrapped within reagent B. The introduction of the buffer solution from inlet C and D compresses the combined streams of reagents A and B horizontally and further focuses reagent A to the center of the channel. The reaction zone, as defined above, exists at the outer profile of the focused reagent A. There are two effects of FRR change on the chemical condition within the reaction zone. First, as the flow rate of the buffer solution increases, FRR decreases, and the reagent B is diluted due to diffusion at the interface between reagent B and buffer streams. The concentration distribution of reagent A, in this case, only shows a slight variation, since it is “wrapped” inside reagent B and shares no interface with the buffer streams. Second, as the flow rate of the buffer solution increases, the stream of reagent B is further focused to the center of channel. The outer profile of reagent B, where the concentration of reagent B is lower, is “pushed” towards the reaction zone. As a result, the molar ratio of A:B decreases as the FRR increases.

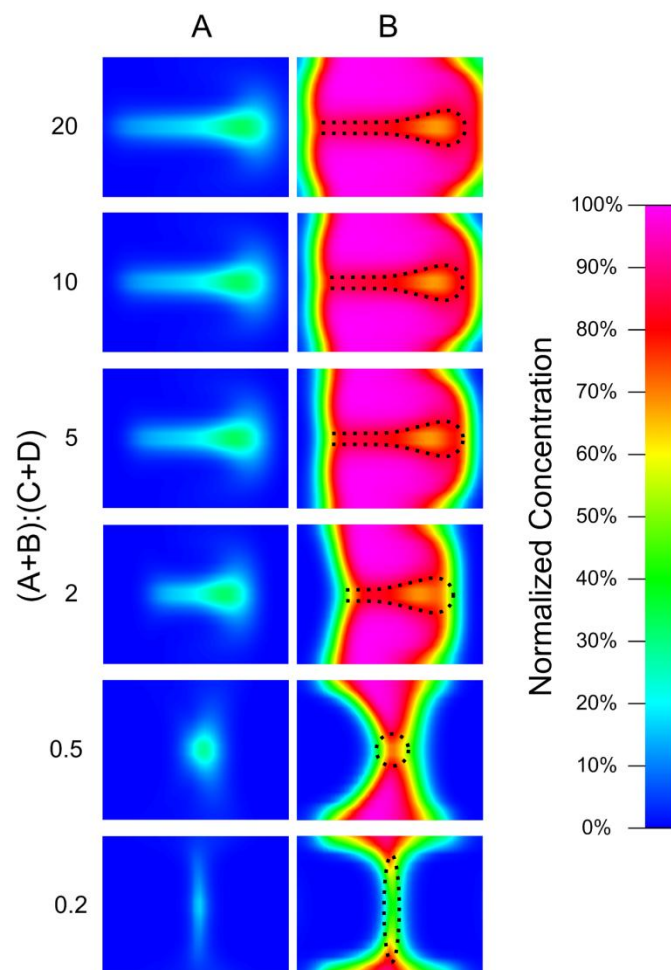


Figure 5-4 The concentration distribution of reagent A and B in cross-section at the location just after the inlets of buffer. The flow rate of reagent A and B are kept as 30  $\mu\text{L}/\text{min}$  and 370  $\mu\text{L}/\text{min}$ , respectively, and the flow rate of buffer C and D are changed. The reaction zone (at the interface between reagent A and B) are of interest. As the flow rate ratio  $(A+B):(C+D)$  decreases, the concentration of reagent A at the reaction zone almost stayed the same, while the concentration of reagent B at the reaction zone decreases. As a result, as the FRR =  $(A+B):(C+D)$  decreases, the molar ratio of A:B at the reaction zone increases.

Therefore, the morphological changes in the synthesized materials may be primarily due to molar ratio changes between reagents A and B within the reaction zone. According to the experimental details, the products shown in Fig. 5-2 a were synthesized with the lowest molar ratio of TTF/ $\text{HAuCl}_4$ , and products shown in Fig. 5-3 d were synthesized with the highest molar ratio of TTF/ $\text{HAuCl}_4$ .

### 5.3.3 Mechanism of Structure Formation

To determine the effects of molar ratio on the synthesized materials, the formation mechanism of TTF-Au hybrid materials must be understood. TTF is a well-known electron donor unit. As shown in Fig. 5-5 a, electron-rich TTF can reversibly lose one or two electrons to form cation  $\text{TTF}^{+\bullet}$  and dication  $\text{TTF}^{2+}$  [29–34]. At the same time, this electron transfer reaction from TTF to gold cations leads to the formation of zero valent gold (Au) [35]. Fig. 5-5 b shows the 1D crystallization by the interaction between cation  $\text{TTF}^{+\bullet}$  and the neutral TTF along the *c*-axis, which results in 1D structures [36–38].

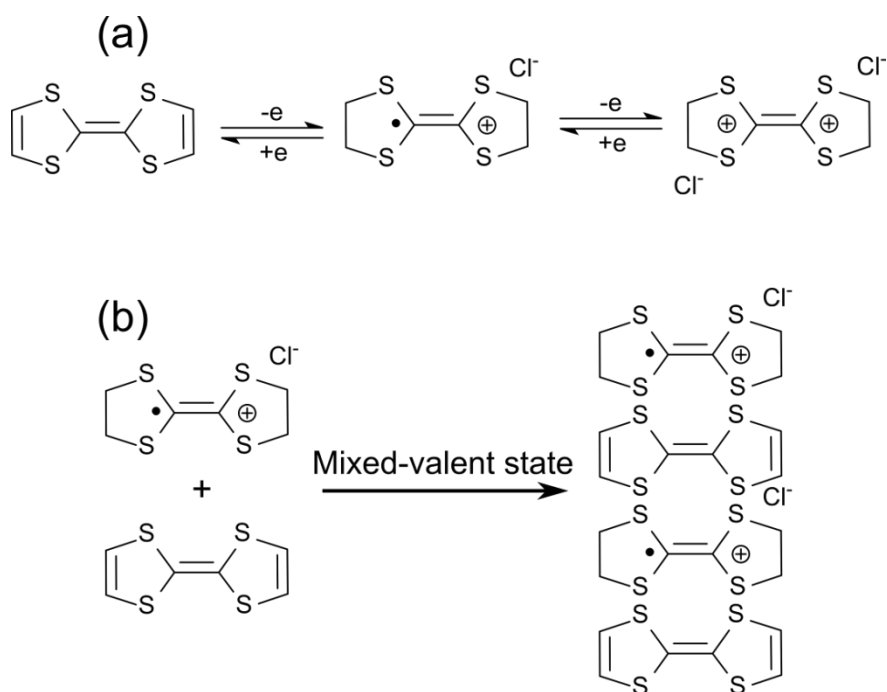


Figure 5-5 Schemes illustrating (a) the oxidation of TTF and (b) the 1D crystallization through the interaction between the neutral and oxidized TTF.

When the molar ratio of TTF/ $\text{HAuCl}_4$  is very low, the concentration of  $\text{HAuCl}_4$  is much higher than TTF, so the major products are gold crystals. TTF acts as a capping

agent by being absorbed on the (111) plane of gold crystals [35]. Due to the stabilization and inhibition of further growth on this plane, gold crystals with top face of the (111) plane are formed. Therefore, the materials in Fig. 5-2 a-c should be gold structures. In the case of Fig. 5-2 a, the molar ratio of TTF/HAuCl<sub>4</sub> was so low that only very few gold cations were reduced to Au, and the low concentration of Au resulted in small gold structures. From Fig. 5-2 a to c, as FRR decreases, the molar ratio of TTF/HAuCl<sub>4</sub> increases and the concentration of Au increases, resulting in concomitant increase in size. Simultaneously, due to the capping agent effect of TTF, the gold structures appear in thin layers with top face of the (111) plane.

Further increase in molar ratio of TTF/HAuCl<sub>4</sub> results in structures showing features dramatically different from gold crystals, which may be caused by the interaction of gold and TTF crystallization process. In this case, it becomes difficult to get pure structures, as shown in Fig. 5-2 d-f. Fig. 5-2 d shows two dimensional dendritic fractal structures, which are generally associated with nonequilibrium growth phenomena [39,40]. As the particles travel through Brownian trajectories to the growing cluster, they stick to cluster arms and growth preferentially takes place at exterior sites, resulting in fractal structures. However, the branches of structures in Fig. 5-2 d are straight, which is different from random fractal structures [41], indicating that the 1D crystallization of the neutral and oxidized TTF may have played a role during structure formation. Fig. 5-2 e shows flower-like aggregates consisting of thin and flat petals with holes. The formation of this type of structures may be due to the fast crystallization process. The molar ratio of TTF/HAuCl<sub>4</sub> is high enough to cause large amount of TTF molecules to be quickly

wrapped within the gold crystals. Later in the acetonitrile, the wrapped TTF can be dissolved gradually, leaving the observed holes on the gold disks [35]. Fig. 5-2 f shows coral-like aggregates consisting of fibers, which indicates features of 1D TTF crystallization.

In the synthesis illustrated in Fig. 5-3, the higher molar ratio of TTF/HAuCl<sub>4</sub> results in TTF-based crystal structures, with gold clusters acting as a capping agent by bonding to the S site of the TTF crystals through the Au-S bonds [42]. The Au-S bond can inhibit the lateral or multidimensional growth of TTF nanocrystals [42]. As a result, all the products in Fig. 5-3 show 1D features. From Fig. 5-3 a to b, increase in molar ratio of TTF/HAuCl<sub>4</sub> results in higher concentrations of both neutral and oxidized TTF, leading to the increase in size. However, further increase in the molar ratio from Fig. 5-3 c to d decreases the HAuCl<sub>4</sub> available to oxidize TTF. The lack of oxidized TTF results in decrease in size.

#### **5.3.4 Optical Properties of the Resultant Solutions**

The UV-vis absorption spectra of the freshly made solutions collected from the outlet channel are shown in Fig. 5-6. All of the samples show absorption peaks at 442 and 587 nm, which are the absorption bands derived from the  $\pi$ - $\pi^*$  transition of the TTF cation [36,43]. This indicates the existence of cation TTF<sup>+</sup>.

The top group of data corresponds to samples shown in Fig. 5-2. The absorption peak around 510 nm is enhanced with increase in FRR. This 510 nm peak is caused by the surface plasmon resonance absorption of gold nanoparticles, evidencing the formation

of gold nanocrystals (Fig. 5-2 a-c) [44]. When  $FRR \leq 5$ , the absorption at 510 nm diminishes, indicating the change in synthesized structures (Fig. 5-2 d-f). This top group of curves also show small absorption peaks at 402 nm, which may be the absorption peak of the TTF cation dimerization,  $(TTF^+)_2$  [45,46].

The spectra in the second group show no absorption peak at 510 nm, indicating the absence of discernible gold nanocrystals. The UV-vis absorption spectra detect the neutral and oxidized TTF in the resultant solution, including chemicals both within and outside the reaction zone. Since flow rates of TTF and  $HAuCl_4$  solutions are constants within this group of experiments, the molar ratio of TTF/ $HAuCl_4$  in the whole resultant solution are identical. Therefore, the UV-vis absorption spectra in this group are similar.

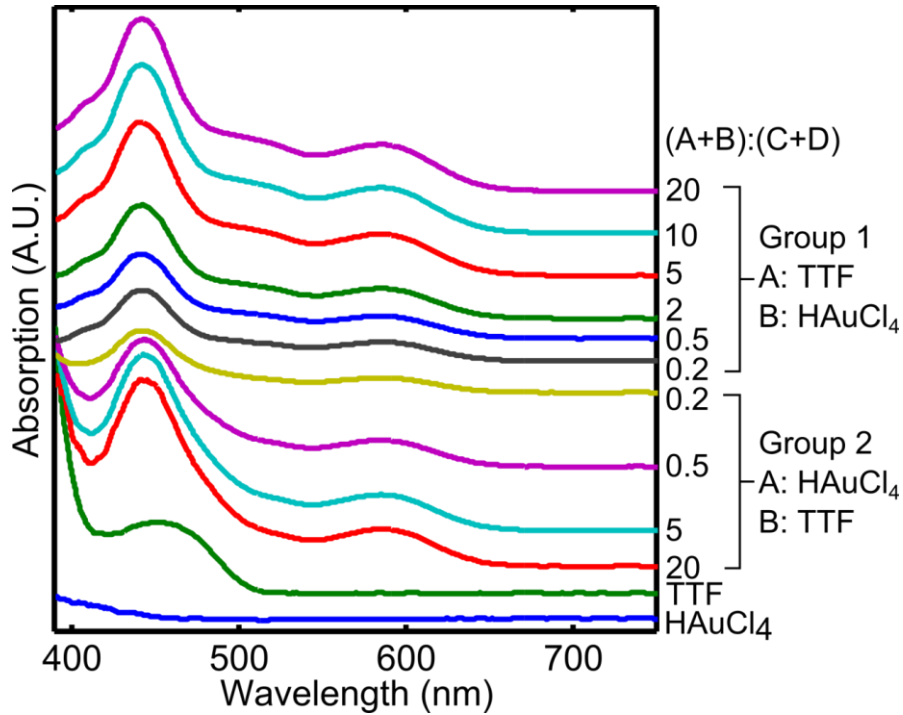


Figure 5-6 Absorption spectra of the solution collected from the outlet of the microfluidic channel. Two evident absorption bands derived from the  $\pi\text{-}\pi^*$  transition of the  $TTF^+$  appear at 442 and

587 nm in all the cases, indicating the electron-transfer reaction and formation of  $\text{TTF}^+$ . For the group of samples using TTF solution as reagent A and  $\text{HAuCl}_4$  solution as reagent B, as the flow rate ratio of (A+B):(C+D) increases, the absorption at wavelength around 406 nm and 510 nm increases. The absorption at 510 nm indicates the formation of gold nanoparticles. This absorption band is significantly damped because of small particle size and the organic capping by TTF. The absorption at 406 nm may be due to the coupling effect between gold nanoparticles and the  $\text{TTF}^{2+}$ .

### **5.3.5 Examination of the Possible Mechanism of FRR Effect by Bulk Mixing Synthesis**

The morphological changes caused by FRR variation may be explained by the molar ratio change within the reaction zone. If this explanation is correct, similar structures should be able to be synthesized by conventional bulk mixing methods with different feed molar ratios. Therefore, bulk synthesis experiments were carried out with a series of feed molar ratio of TTF/ $\text{HAuCl}_4$ . As expected, structures similar to Fig. 5-2 and Fig. 5-3 were obtained, as shown in Fig. 5-7 and Fig. 5-8. The morphologies of samples synthesized by bulk mixing with different feed molar ratios follow the hypothesis about structures formation discussed in Sec 5.3.4.

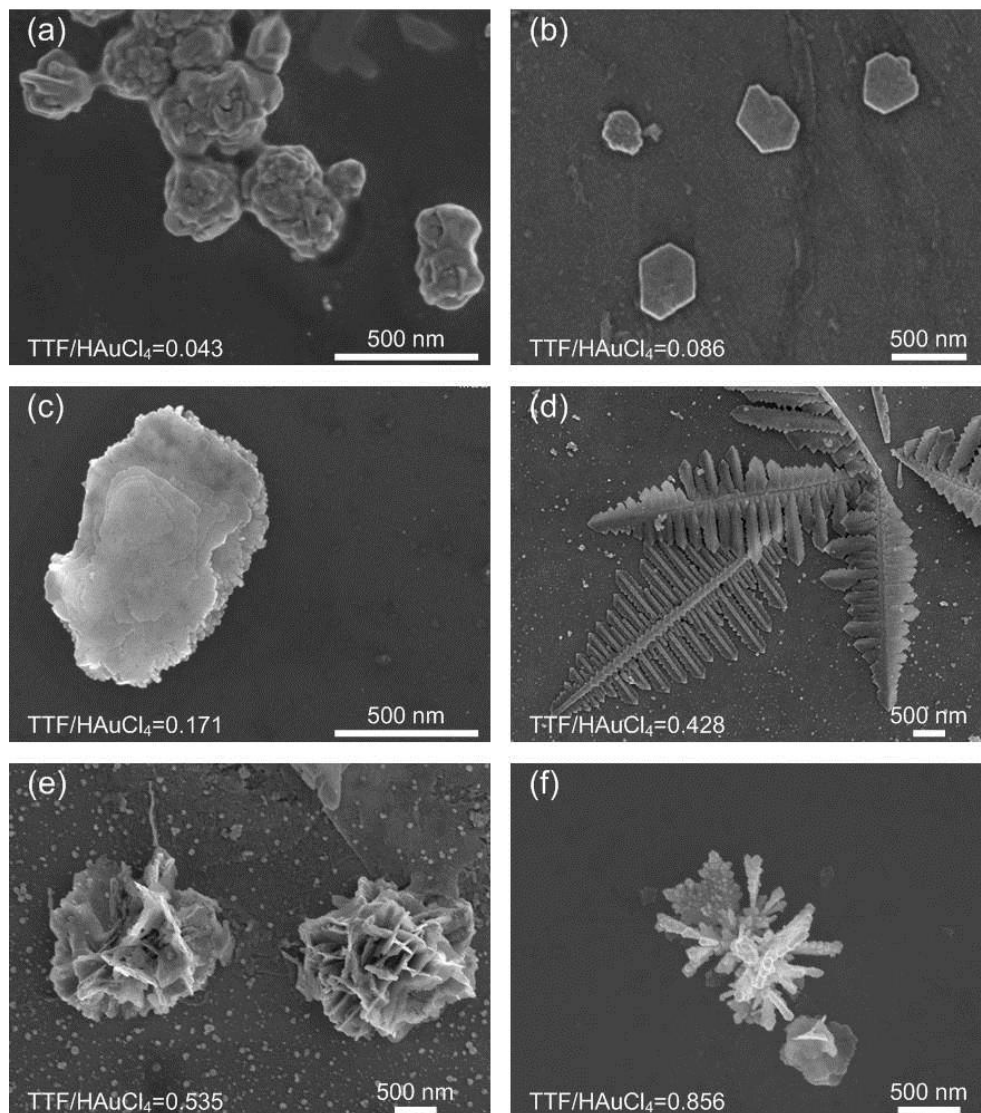


Figure 5-7 SEM images of nanomaterials prepared using bulk mixing method. As the feed molar ratio TTF/HAuCl<sub>4</sub> increases, the morphologies of the synthesized nanomaterials experience changes through (a) branching aggregates consisting of irregularly aligned polyhedral crystals, (b) triangle or hexagonal shapes, (c) multi-layered structures consisting of thin and flat layers, (d) two dimensional dendritic nanostructures, (e) flower-like aggregates consisting of thin, flat petals and (f) coral-like aggregates consisting of fibers.

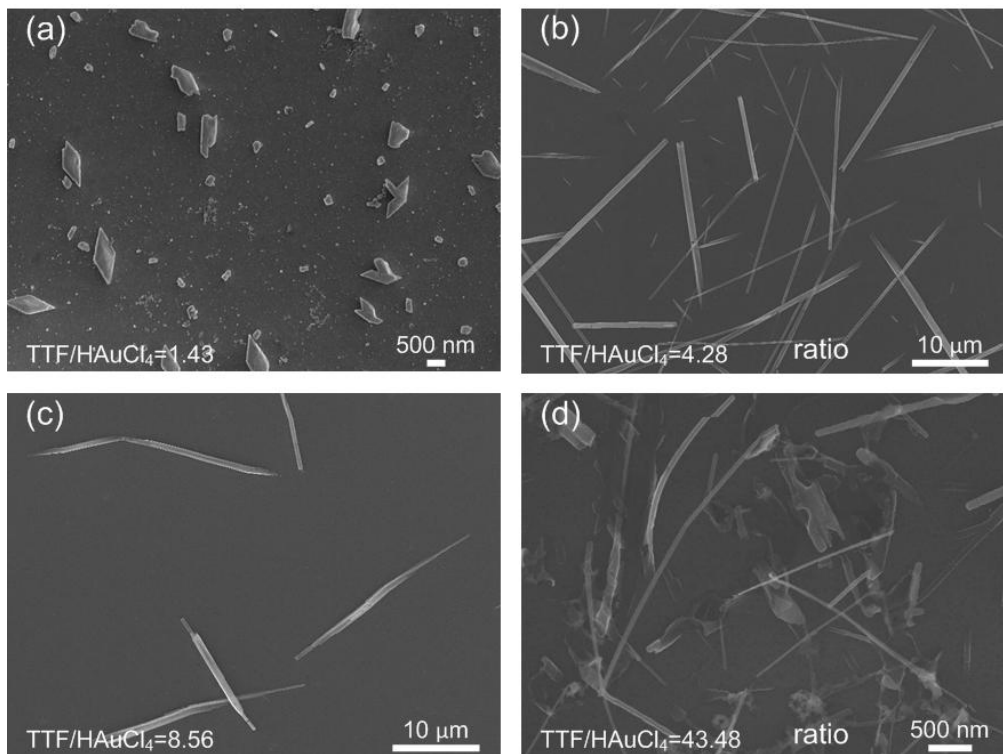


Figure 5-8 SEM images of nanomaterials prepared using bulk mixing method. As the feed molar ratio of TTF/HAuCl<sub>4</sub> increases, the morphologies of the synthesized nanomaterials experience changes through (a) diamond shape with apex angle of 58 °, (b) long and hollow wires of several tens of micro meters, (c) short wires of several micro meters and (d) nano-sized needles. .

The UV-vis absorption spectra of the bulk mixing samples are also similar to the 3D-HF samples, with only slight differences. As shown in Fig. 5-9, the UV-vis absorption spectra of bulk mixing samples can be divided into two groups. The first group of samples have molar ratio of TTF/HAuCl<sub>4</sub> less than 0.171. The absorption spectra of this group of samples show small peaks at 510 nm, and the absorption at 510 nm increases as the molar ratio increases, indicating the formation of gold nanoparticles. In contrast to the 3D-HF samples, no obvious peaks of the TTF cation (442 nm and 587 nm) can be observed in this group of data, due to the lack of TTF in the solution. The second group in Fig. 5-9 are the samples with molar ratio higher than 0.43. When

TTF/HAuCl<sub>4</sub> equals to 0.43, the absorption curve exhibits a new peak around 402 nm. This absorption spectrum is similar to that of samples shown in Fig. 5-2 d, indicating the existence of similar compounds. Further increase in TTF/HAuCl<sub>4</sub> decreases the intensity of the absorption peak at 442nm and 587 nm. When TTF/HAuCl<sub>4</sub> ≥ 82.64, the peak at 587 nm almost disappears, underlying the decrease of TTF<sup>+</sup>.

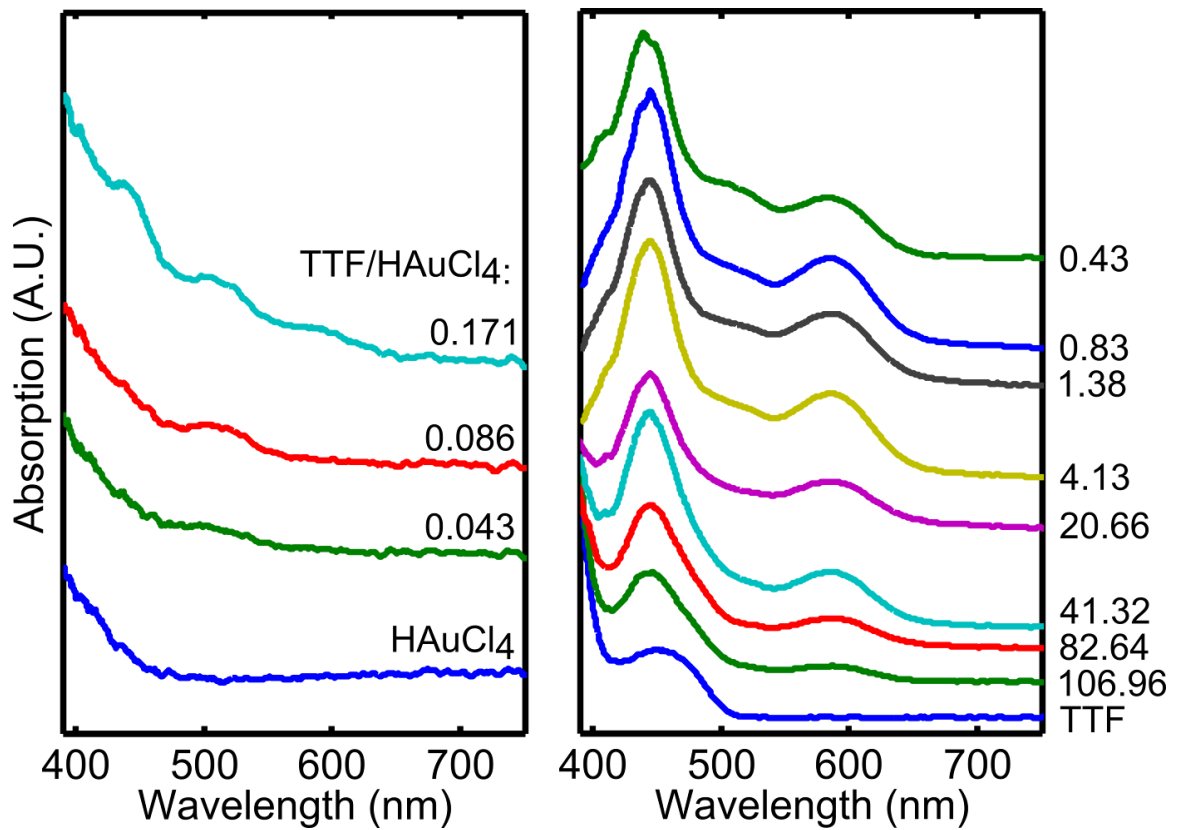


Figure 5-9 Absorption spectra of the solution after bulk mixing. When the feed molar ratio  $TTF/HAuCl_4 \leq 0.171$ , the absorption band at 510 nm increases as the  $TTF/HAuCl_4$  increases, indicating formation of more gold nanoparticles. The absorption bands at 442 nm and 587 nm are weak, indicating almost no formation of  $TTF^+$ . When the feed molar ratio  $TTF/HAuCl_4 \geq 0.43$ , the absorption band at 510 nm decreases as the  $TTF/HAuCl_4$  increases, indicating less gold nanoparticle formation. The strong bands at 442 nm and 587 nm show the presence of  $TTF^+$ . In the case of  $TTF/HAuCl_4 = 0.43$ , the absorption band at 406 nm appears, may be due to the coupling effect between gold nanoparticles and the  $TTF^{2+}$ .

The nanostructures synthesized by the bulk mixing method were further characterized by X-ray diffraction (XRD) to determine their crystal direction. The results are shown in Fig. 5-10. According to the unit cell data for the TTF-chlorides in Table 5-1[47], different crystal structures can be recognized.

Table 5-1. Unit Cell Data for the TTF-Chlorides\*

Dication salts	a=13.56 c=10.10 N=8; $I4_1/acd$
Monocation salts	a=11.073 b=11.218 c=13.95 N=8; $PbCa$
Ordered mixed valence salts	a=10.77 b=3.56 c=22.10
Disordered mixed valence salts	a=11.12 c=3.595

\* In Å units, maximum standard deviation  $\pm 0.05\%$ . N is the number of formula units/cell.

Table 5-1 Unit cell data for the TTF-chlorides

When the initial feed molar ratio  $TTF/HAuCl_4 \leq 0.18$ , the XRD patterns show sharp reflections corresponding to the face-centered cubic (fcc) structure of metallic gold with the (111) top planes, indicating that the disks are made of pure gold and their top face planes are the (111) planes. This is a very common structural configuration in plate-like gold crystals such as gold nanoprisms or nanodisks [48]. As the molar ratio of

TTF/HAuCl<sub>4</sub> increased to 0.43, the XRD result indicates (313) plane of the (TTF)Cl<sub>2</sub> crystals. When TTF/HAuCl<sub>4</sub> = 0.87, no diffraction peak can be observed.

When the molar ratio of TTF/HAuCl<sub>4</sub> is in the range between 1.09 and 1.64, the diffraction peaks show a pure plane in direction of (101) of the ordered mixed valence salts of TTF. According to Table 5-1, the (101) plane is at 29° to the *c*-axis, which agrees well with the 58° apex angle of samples in Fig. 5-8 a. As the molar ratio of TTF/HAuCl<sub>4</sub> further increases, the diffraction peak from (102) plane becomes dominant in the ordered mixed valence salts of TTF. When TTF/HAuCl<sub>4</sub> > 8.7, another diffraction peak (004) emerges. Finally, when TTF/HAuCl<sub>4</sub> increases to 43.49, the (102) diffraction peak becomes sharper, indicating it is the dominant plane of the sample.

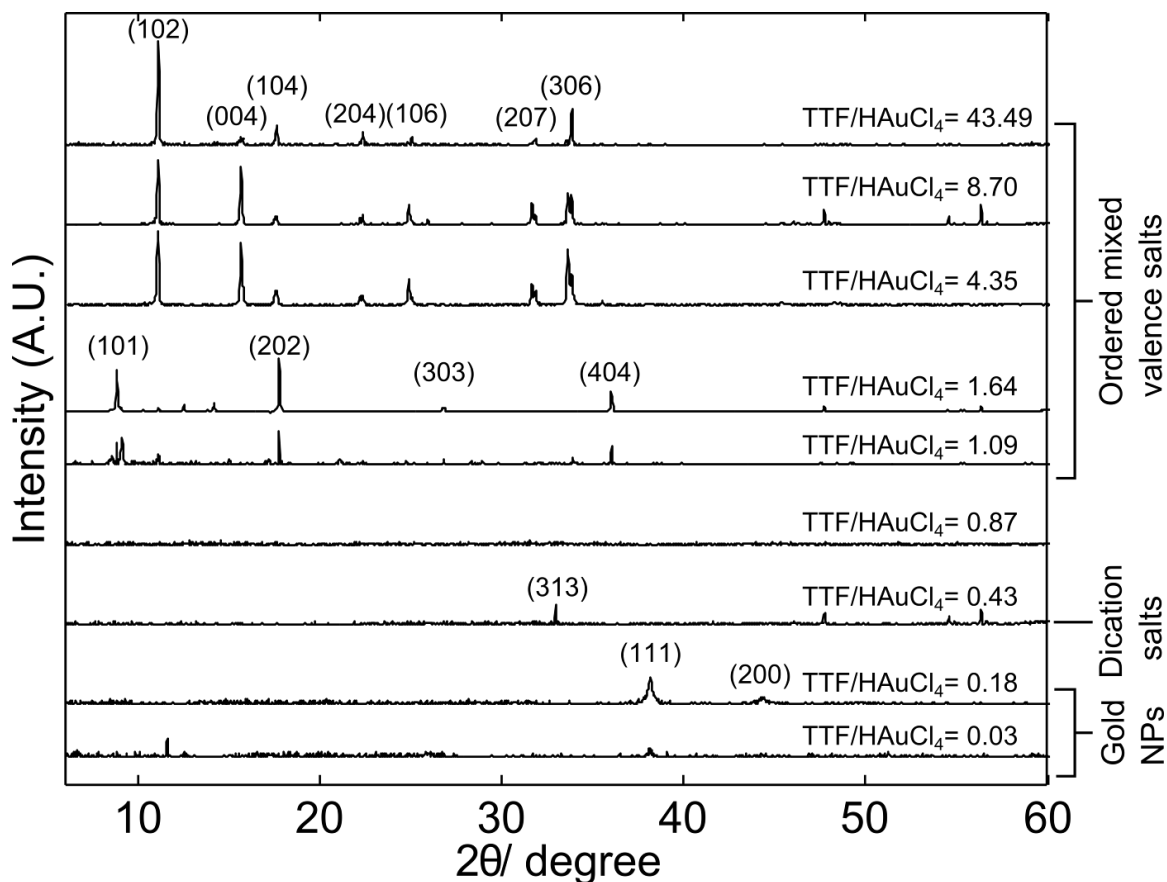


Figure 5-10 The XRD pattern of the samples synthesized by bulk mixing method. The samples can be divided into 4 groups. (1) When the feed molar ratio  $\text{TTF}/\text{HAuCl}_4 \leq 0.18$ , the samples show a primary peak corresponding to the face-centered cubic (fcc) structure of metallic gold with the (111) diffraction intensified considerably. (2) When  $\text{TTF}/\text{HAuCl}_4 = 0.43$ , the (313) structure of  $(\text{TTF})\text{Cl}_2$  appears, indicating the presence of  $\text{TTF}^{2+}$ . (3) When  $\text{TTF}/\text{HAuCl}_4 = 0.87$ , no obvious peaks can be observed. (4) When  $\text{TTF}/\text{HAuCl}_4 \geq 1.09$ , multiple peaks showing the crystal structures of ordered mixed valence salt, indicating the presence of both  $\text{TTF}^+$  and TTF. When  $1.09 \leq \text{TTF}/\text{HAuCl}_4 \leq 1.64$ , the (101) plane is the major crystal structure. With the further increase in  $\text{TTF}/\text{HAuCl}_4$ , the (102) plane becomes the primary structure.

Overall, the morphologies, optical properties, and crystalline structures of the materials synthesized by the bulk mixing method agree well with the hypothesis of the structure formation mechanism, validating the assumption about the FRR effect on morphologies in 3D-HF experiments.

Even though similar structures can be obtained by either 3D-HF or the bulk mixing method, the samples fabricated by 3D-HF method show better uniformity (Fig. 5-11).

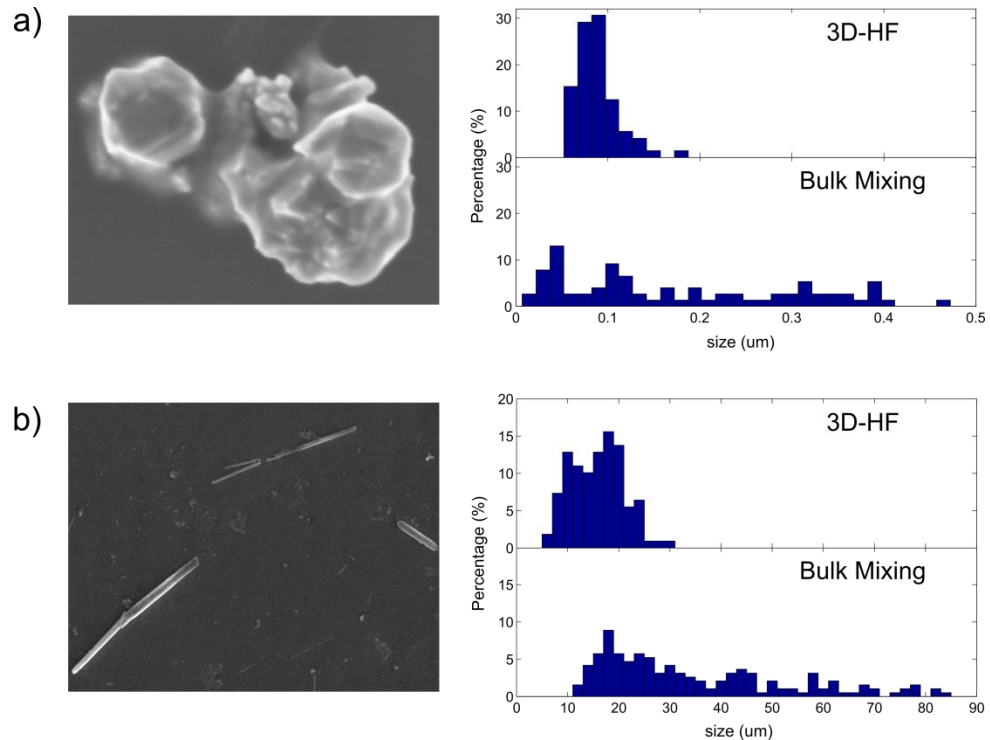


Figure 5-11 Size distribution of selected TTF-Au hybrid structures synthesized by 3D-HF and bulk mixing method.

## 5.4 Conclusion

The TTF-Au hybrid materials, which are sensitive to the reagent molar ratios, have been synthesized in 3D-HF microfluidic reactors. Interestingly, while keeping the flow rate of reagents the same, and changing only the flow rate of buffer, materials with different morphologies can be synthesized. This experimental result is explained by changes in the molar ratio of TTF/HAuCl<sub>4</sub> within the reaction zone. This explanation is supported by the fact that similar structures can be synthesized by the conventional bulk mixing method with different molar ratios. The morphologies, optical properties and crystalline structures of the bulk mixing samples agree well with the predictions. Therefore, the chemical distribution within 3D-HF microfluidic reactors can be finely controlled by changing the buffer flow rate, which can be used to control the properties of synthesized nanomaterials.

## References

- [1] Burda, C., Chen, X., Narayanan, R. and El-Sayed, M.A., "*Chemistry and properties of nanocrystals of different shapes*," Chemical Reviews, **105**, 1025–1102 (2005)
- [2] Xia, Y., Xiong, Y., Lim, B. and Skrabalak, S.E., "*Shape-controlled synthesis of metal nanocrystals: simple chemistry meets complex physics?*," Angewandte Chemie International Edition, **48**, 60–103 (2009)
- [3] Xia, Y. and Halas, N.J., "*Shape-controlled synthesis and surface plasmonic properties of metallic nanostructures*," MRS Bulletin, **30**, 338–348 (2005)
- [4] Kimura, G. and Yamada, K., "*Electrochromism of poly(3,4-ethylenedioxythiophene) films on Au nano-brush electrode*," Synthetic Metals, **159**, 914–918 (2009)
- [5] Sperling, R.A., Rivera Gil, P., Zhang, F., Zanella, M. and Parak, W.J., "*Biological applications of gold nanoparticles*," Chemical Society Reviews, **37**, 1896–1908 (2008)
- [6] Lindman, S., Lynch, I., Thulin, E., Nilsson, H., Dawson, K.A. and Linse, S., "*Systematic investigation of the thermodynamics of HSA adsorption to N-isopropylacrylamide/N-tert-Butylacrylamide copolymer nanoparticles. Effects of particle size and hydrophobicity*," Nano Letters, **7**, 914–920 (2007)
- [7] Mann, S., "*The chemistry of form*," Angewandte Chemie International Edition, **39**, 3392–3406 (2000)
- [8] Sun, Y. and Xia, Y., "*Shape-controlled synthesis of gold and silver nanoparticles*," Science, **298**, 2176–2179 (2002)
- [9] Jana, N.R., Gearheart, L. and Murphy, C.J., "*Wet chemical synthesis of silver nanorods and nanowires of controllable aspect ratio*," Chemical Communications, 617–618 (2001)
- [10] Sun, Y. and Xia, Y., "*Large-scale synthesis of uniform silver nanowires through a soft, self-seeding, polyol process*," Advanced Materials, **14**, 833–837 (2002)
- [11] Zhao, N., Wei, Y., Sun, N., Chen, Q., Bai, J., Zhou, L., Qin, Y., Li, M. and Qi, L., "*Controlled synthesis of gold nanobelts and nanocombs in aqueous mixed surfactant solutions*," Langmuir, **24**, 991–998 (2008)

- [12] Wu, H.-L., Kuo, C.-H. and Huang, M.H., "*Seed-mediated synthesis of gold nanocrystals with systematic shape evolution from cubic to trisoctahedral and rhombic dodecahedral structures*," *Langmuir*, **26**, 12307–12313 (2010)
- [13] Lee, J.-H., Kamada, K., Enomoto, N. and Hojo, J., "*Morphology-selective synthesis of polyhedral gold nanoparticles: what factors control the size and morphology of gold nanoparticles in a wet-chemical process*," *Journal of Colloid and Interface Science*, **316**, 887–892 (2007)
- [14] Hao, E., Kelly, K.L., Hupp, J.T. and Schatz, G.C., "*Synthesis of silver nanodisks using polystyrene mesospheres as templates*," *Journal of the American Chemical Society*, **124**, 15182–15183 (2002)
- [15] Chen, S., Fan, Z. and Carroll, D.L., "*Silver nanodisks: synthesis, characterization, and self-assembly*," *Journal of Physical Chemistry B*, **106**, 10777–10781 (2002)
- [16] Liz-Marzán, P.S.K. and I.P.-S. and B.R.-G. and F.J.G. de A. and L.M., "*High-yield synthesis and optical response of gold nanostars*," *Nanotechnology*, **19**, 015606 (2008)
- [17] Ding, J.F. and X.M. and H.C. and X.S. and B., "*Nanoparticle-aggregated 3D monocrystalline gold dendritic nanostructures*," *Nanotechnology*, **17**, 5841-5845 (2006)
- [18] Xiao, J.P., Xie, Y., Tang, R., Chen, M. and Tian, X.B., "*Novel ultrasonically assisted templated synthesis of palladium and silver dendritic nanostructures*," *Advanced Materials*, **13**, 1887–1891 (2001)
- [19] Gomar-Nadal, E., Puigmarti-Luis, J. and Amabilino, D.B., "*Assembly of functional molecular nanostructures on surfaces*," *Chemical Society Reviews*, **37**, 490–504 (2008)
- [20] Xia, Y., Yang, P., Sun, Y., Wu, Y., Mayers, B., Gates, B., Yin, Y., Kim, F. and Yan, H., "*One-dimensional nanostructures: synthesis, characterization, and applications*," *Advanced Materials*, **15**, 353–389 (2003)
- [21] Salmon, J.-B., Dubrocq, C., Tabeling, P., Charier, S., Alcor, D., Jullien, L. and Ferrage, F., "*An approach to extract rate constants from reaction–diffusion dynamics in a microchannel*," *Analytical Chemistry*, **77**, 3417–3424 (2005)
- [22] Karnik, R., Gu, F., Basto, P., Cannizzaro, C., Dean, L., Kyei-Manu, W., Langer, R. and Farokhzad, O.C., "*Microfluidic platform for controlled synthesis of polymeric nanoparticles*," *Nano Letters*, **8**, 2906–2912 (2008)

- [23] Ismagilov, R.F., Stroock, A.D., Kenis, P.J.A., Whitesides, G. and Stone, H.A., "*Experimental and theoretical scaling laws for transverse diffusive broadening in two-phase laminar flows in microchannels*," Applied Physics Letters, **76**, 2376 (2000)
- [24] Williams, J.M., Schultz, A.J., Geiser, U.R.S., Carlson, K.D., Kini, A.M., Wang, H.H., Kwok, W.-K., Whangbo, M.-H. and Schirber, J.E., "*Organic superconductors—new benchmarks*," Science , **252** , 1501–1508 (1991)
- [25] Coronado, E., Galan-Mascaros, J.R., Gomez-Garcia, C.J. and Laukhin, V., "*Coexistence of ferromagnetism and metallic conductivity in a molecule-based layered compound*," Nature, **408**, 447–449 (2000)
- [26] Somani, R.H., Hsiao, B.S., Nogales, A., Srinivas, S., Tsou, A.H., Sics, I., Balta-Calleja, F.J. and Ezquerro, T.A., "*Structure development during shear flow-induced crystallization of i-PP: in-situ small-angle X-ray scattering study*," Macromolecules, **33**, 9385–9394 (2000)
- [27] Mao, X., Waldeisen, J.R. and Huang, T.J., "*“Microfluidic drifting”--implementing three-dimensional hydrodynamic focusing with a single-layer planar microfluidic device*," Lab on a Chip, **7**, 1260–1262 (2007)
- [28] Mao, X., Nawaz, A.A., Lin, S.-C.S., Lapsley, M.I., Zhao, Y., McCoy, J.P., El-Deiry, W.S. and Huang, T.J., "*An integrated, multiparametric flow cytometry chip using “microfluidic drifting” based three-dimensional hydrodynamic focusing*," Biomicrofluidics, **6**, 24113 (2012)
- [29] Yamada, J. -i. and Sugimoto, T., TTF Chemistry: Fundamentals and Applications of Tetrathiafulvalene, Kodansha and Springer, New York, NY (2004)
- [30] Batail, P., "*Introduction: molecular conductors*," Chemical Reviews, **104**, 4887–4890 (2004)
- [31] Williams, J.M., Ferraro, J.R., Thorn, R.J., Carlson, K.D., Geiser, U., Wang, H.H., Kini, A.M. and Whangbo, M.H., Organic Superconductors (Including Fullerenes). Synthesis, Structure, Properties, and Theory, Prentice Hall, Englewood Cliffs, NJ, (1992)
- [32] Saito, G. and Yoshida, Y., "*Development of conductive organic molecular assemblies: organic metals, superconductors, and exotic functional materials*," Bulletin of the Chemical Society of Japan, **80**, 1–137 (2007)
- [33] Hasegawa, M., Daigoku, K., Hashimoto, K., Nishikawa, H. and Iyoda, M., "*Face-to-face dimeric tetrathiafulvalenes and their cation radical and dication species as*

- models of mixed valence and  $\pi$ -dimer states,*" Bulletin of the Chemical Society of Japan, **85**, 51–60 (2012)
- [34] Pop, F., Ding, J., Daku, L.M.L., Hauser, A. and Avarvari, N., "*Tetrathiafulvalene-s-tetrazine: versatile platform for donor-acceptor systems and multifunctional ligands,*" RSC Advances, **3**, 3218–3221 (2013)
- [35] Yang, J., Qi, L., Zhang, D., Ma, J. and Cheng, H., "*Dextran-controlled crystallization of silver microcrystals with novel morphologies,*" Crystal Growth & Design, **4**, 1371–1375 (2004)
- [36] Torrance, J.B., Scott, B.A., Welber, B., Kaufman, F.B. and Seiden, P.E., "*Optical properties of the radical cation tetrathiafulvalenium (TTF<sup>+</sup>) in its mixed-valence and monovalence halid salts,*" Physical Review B, **19**, 730–741 (1979)
- [37] Naka, K., Ando, D., Wang, X. and Chujo, Y., "*Synthesis of organic-metal hybrid nanowires by cooperative self-organization of tetrathiafulvalene and metallic gold via charge-transfer,*" Langmuir, **23**, 3450–3454 (2007)
- [38] Iyoda, M., Hasegawa, M., Kuwatani, Y., Nishikawa, H., Fukami, K., Nagase, S. and Yamamoto, G., "*Effects of molecular association in the radical-cations of 1,8-Bis(ethylenedithiotetrathiafulvalenyl)naphthalene,*" Chemistry Letters, **30**, 1146–1147 (2001)
- [39] Meakin, P., "*Formation of fractal clusters and networks by irreversible diffusion-limited aggregation,*" Physical Review Letters, **51**, 1119–1122 (1983)
- [40] Witten, T.A. and Sander, L.M., "*Diffusion-limited aggregation, a kinetic critical phenomenon,*" Physical Review Letters, **47**, 1400–1403 (1981)
- [41] Wang, X., Naka, K., Itoh, H., Park, S. and Chujo, Y., "*Synthesis of silver dendritic nanostructures protected by tetrathiafulvalene,*" Chemical Communications, 1300–1301 (2002)
- [42] Naka, K., Ando, D. and Chujo, Y., "*Effect of substituent groups for formation of organic-metal hybrid nanowires by charge-transfer of tetrathiafulvalene derivatives with metal ion,*" Synthetic Metals, **159**, 931–934 (2009)
- [43] Tanaka, K., Kunita, T., Ishiguro, F., Naka, K. and Chujo, Y., "*Modulation of morphology and conductivity of mixed-valence tetrathiafulvalene nanofibers by coexisting organic acid anions,*" Langmuir, **25**, 6929–6933 (2009)

- [44] Link, S. and El-Sayed, M.A., "*Size and temperature dependence of the plasmon absorption of colloidal gold nanoparticles*," *Journal of Physical Chemistry B*, **103**, 4212–4217 (1999)
- [45] Craig, D.P. and Walmsley, S.H., *Excitons in Molecular Crystals: Theory and Applications*, Benjamin, New York, NY (1968)
- [46] Davydov, A.S., *Theory of Molecular Excitons*, Plenum, New York, NY (1971)
- [47] Scott, B.A., La Placa, S.J., Torrance, J.B., Silverman, B.D. and Welber, B., "*The crystal chemistry of organic metals. Composition, structure, and stability in the tetrathiafulvalinium-halide systems*," *Journal of the American Chemical Society*, **99**, 6631–6639 (1977)
- [48] Shankar, S.S., Rai, A., Ankamwar, B., Singh, A., Ahmad, A. and Sastry, M., "*Biological synthesis of triangular gold nanoprisms*," *Nature Materials*, **3**, 482–488 (2004)

## Chapter 6 Conclusions and Future Research

### 6.1 Conclusion

In Chapter 1, a hypothesis was made that within microfluidic reactors diffusion-limit reactions occur during materials synthesis, and enhancement in mixing can improve the uniformity of the synthesized product. The central aim of the research reported in this dissertation was to examine this hypothesis and to push the microfluidic reactors towards real industrial and biomedical application by developing miniaturized microfluidic reactors suitable for mass fabrication. To achieve this aim, I firstly compared different types of microfluidic mixing strategies, and designed two microfluidic reactors, the acoustic-assisted bubble based microfluidic reactor and the acoustic-assisted 3D-HF microfluidic reactor, for the studies on nanomaterials synthesis. Both reactors can enhance mixing. These two reactors were used for polyplexes synthesis. The uniformity of the polyplexes were characterized and compared with those synthesized by the conventional bulk mixing method. As the polyplexes synthesized by these two reactors showed high uniformity, the biological performance of the polyplexes were also enhanced, confirmed by the DNA transfection experiments. Compared with the acoustic-assisted bubble based microfluidic reactor, the acoustic-assisted 3D-HF microfluidic reactor is more attractive due to its portability. At the end, I studied how the mixing conditions can affect the local chemical ratio within the 3D-HF device by synthesizing TTF-Au hybrid materials. The morphologies of the synthesized materials varied with the change of mixing conditions. Computational simulation of the chemical concentration

distribution and study of formation mechanism of the hybrid materials provided a good understanding of the effect of mixing condition. Therefore 3D-HF device can provide precise control over the shape and element composition of the synthesized products.

The scientific consequences of these results can be summarized as follows:

1. Microfluidic reactors with simple configuration and good mixing performance were designed. These microfluidic reactors are suitable for massive fabrication for industrial applications. Additionally, the 3D-HF microfluidic reactor can be miniaturized for on-site and on-demand synthesis for biomedical applications.
2. The hypothesis was proved that generally diffusion-limit reactions occur within microfluidic reactors, and enhancement in mixing can improve the uniformity of the synthesized product.
3. It was proved that, polyplexes with improved uniformity show better biological performance, which again confirms the importance of mixing in microfluidic devices.
4. Within the “microfluidic-drifting” based 3D hydrodynamic focusing device, the mixing conditions can affect the local chemical ratio, providing precise control over the shape and element composition of the synthesized products. The morphologies, optical properties, and crystalline structures of the materials synthesized by control experiments agreed well with the hypothesis of the structure formation mechanism, which validated the assumption about the mixing condition effect on local chemical ratio in 3D-HF devices.

## 6.2 Future Research

One important direction for future work is to study the variation of the physical properties of polyplexes synthesized by microfluidic reactors with different flow conditions. Chapter 3 showed the mixing performance varies with the nitrogen pressure change. Chapter 4 showed the size of polyplexes changes with the flow rate. As in the field of gene therapy, the best transfection efficiency occurs with the optimized size of polyplexes, which is not necessarily the smallest size. Thus, microfluidic reactor can be a versatile tool to control the size of polyplexes for the best biological performance while using various types of DNA and polymers.

Another direction of future work could be design of scaled-up microfluidic devices for high throughput synthesis. To achieve the aim of translation the research achievement to industrial applications, the synthesis device should meet the requirements including high throughput synthesis, small number of flow controls, ease to replace parts of the device (or local problem such as clogging will not affect the performance of the whole device) and low-cost. Therefore, additional efforts are needed to push the reported microfluidic devices for real industrial applications. In the future, the mature high throughput scaled-up microfluidic reactors with low cost will be superior to current synthetic technologies and fulfill significant unmet needs in the market.

## **Appendix Single-Step Holographic Fabrication of Large-Area Patterned Corrugated Metal Films for Potential Application as Microfluidic Sensor<sup>‡</sup>**

This appendix introduces a new and simple method to fabricate patterned corrugated silver thin films, which can be easily integrated to on-chip devices. A dip in the transmission spectra of these silver films is observed due to certain visible wavelengths coupling to surface plasmon polaritons (SPPs) and the wavelength of this dip has a linear relationship with the surrounding material's refractive index (RI) with a sensitivity of 553.4 nm/RIU. The sensitivity of the silver thin films and the ease of integration to on-chip device make it promising candidates as on-chip sensors. This low-cost fabrication method also enables the applications as disposable sensors.

### **A.1 Introduction**

Surface plasmon polaritons (SPPs) are electromagnetic waves travelling along a metal-dielectric or metal-air interface. The excitation wavelength of SPPs greatly depends on the refractive index (RI) of surrounding materials [1–3]. Therefore, SPPs have been widely used for label-free and real-time biological and chemical sensing applications [2,4–8]. Integration of SPPs and microfluidic on-chip system enables the miniaturized biosensing platform for rapid analysis with low cost [9–13]. Recently, fabrication of portable, fast, and disposable sensors based on SPPs has become an active area of research in order to fulfil the end users' requirement [14–17].

---

<sup>‡</sup>This appendix is based on: Lu, M., Juluri, B.K., Liu, Y.J., Bunning, T.J. and Huang, T.J., “*Single-step holographic fabrication of large-area periodically corrugated metal films,*” *Journal of Applied Physics*, **112**, 113101 (2012)

SPPs cannot be directly excited by illumination on a flat metal surface because the momentum of light in free space is not sufficient to match the momentum of the SPPs. A traditional solution is the Turbadar-Kretschmann-Raether configuration<sup>†</sup> (*i.e.*, the prism-coupling technique) [18–20]. Even though sensors based on this technique show great sensitivity up to 13800 nm/RIU (refractive index unit) [4], they are not applicable for disposable and multi-analyte sensing because of the requirement of expensive optical prisms and tedious optical alignment.

An alternative technique is to use sub-wavelength, periodically structured metal films to excite SPPs through direct illumination [21–25]. By measuring the normal incidence transmission or reflection, the excitation wavelength can be determined from the peak wavelength of the spectra, and only simple optical setup is required for this method. Miniaturized sensors have been developed based on this technique. The high surface area and strong local confinement of surface plasmon fields on the structured metal films can enhance the interaction with the analyte layer [26,27], resulting in high sensitivity and low detection limit. For most applications, the analytes are in aqueous solutions which have strong absorption at 970 nm and 1160 nm [17]. Therefore, to avoid these absorption wavelengths, the periodicities of such structures are typically designed

---

<sup>†</sup>Turbadar-Kretschmann-Raether configuration is often called Kretschmann configuration or Kretschmann-Raether configuration after the authors of a 1968 paper [18]. However, Turbadar had anticipated the work of Kretschmann and Raether completely in 1959 [19,20]. Turbadar showed that, by using a thin aluminum film deposited on a glass prism, the reflectance showed a sharp dip as the angle of incidence exceeded the critical angle for a glass/air interface. He also showed that the reflectance can be lowered down to zero with the proper choice of the thickness of the metal film. Although Turbadar had not used the word “plasmon”, propriety demands that Turbadar’s contribution be adequately acknowledges.

so that the resonance wavelength of SPPs is in the visible region. Sensors using periodic metal structures have shown sensitivity in the range of  $\sim 70$  to  $\sim 800$  nm/RIU [6]. To further improve the sensitivity and accuracy of this type of sensor, one key step is to fabricate uniform structures over the whole detection area [17]. In addition, in order to achieve multi-analyte sensing through multichannel sensors, uniform structures over a large area are needed.

To date, it remains a challenge to fabricate uniform, sub-micron periodic metal structures over a large area with low cost. Electron-beam lithography (EBL) [28] and focused ion beam (FIB) milling [29] can fabricate most desired patterns with high yield and outstanding resolution, but they are limited by their low processing speeds, high capital cost, and difficulty in accessing the facilities. Nanosphere lithography (NSL) was reported as a more practical method, but it suffers from the low sensitivity ( $\sim 150$  nm/RIU) because it is difficult to fabricate defect-free patterns over large areas [30].

Nanoimprint lithography (NIL) is a low-cost process with high resolution and high throughput which has produced sensitive sensors (800 nm/RIU) based on metal nanostructures [6]. Massively parallel nanofabrication using NIL is ideal for low-cost sensor fabrication. However, in the NIL approach, EBL or FIB is still needed for molds fabrication with sub-wavelength structures [31], and multiple steps are required to transfer the pattern to the metal surface [32]. Direct nano-imprinting of metal has been reported recently [33–35]. However, it requires either high-temperature and high-pressure control [34], or multi-step preparations including spin-coating of polymer and metal

deposition by sputtering or thermal deposition [35]. Therefore, capital cost is still high for sensor fabrication by the NIL method.

Holographic lithography transfers a multi-beam interference pattern into a photosensitive material which enables large-scale fabrication at low cost with high uniformity [36]. It has been implemented to fabricate two-dimensional (2D) [37–39] and three-dimensional (3D) micro/nanostructures [40–44]. Direct patterning of metals by lasers has mainly focused on the generation of surface structures based on high-power-laser-induced ablation, melting, evaporation, phase transformations, or thermal decomposition of metal ions [45–49]. These methods require expensive femtosecond lasers [45], nanosecond lasers [46,47], or CW lasers with high power density (*e.g.*, 8,000,000 W/cm<sup>2</sup>) [48,49]; furthermore, they rely on laser irradiation and melting-induced mass transfer, making it difficult to generate patterns with sub-micron resolution.

I developed a single-step, high-throughput method to fabricate one-dimensional (1D) and 2D, sub-wavelength patterned silver structures over centimeter scale areas by direct deposition of silver from solutions using holographic patterning at room temperature. This setup uses only a low-power (157 mW) green laser and a simple prism. Each sample uses only a standard glass slide, 1 mL of ammonia, 0.02 gram of silver oxide, and 0.5 gram of glucose. The fabricated silver structures show a periodicity of 570 nm. The patterned structures enable the excitation of SPPs. The 1D patterned corrugated silver films show a high sensitivity of 553.4 nm/RIU to the change in the surrounding RI. The figure of merit (FoM) is calculated by dividing the sensitivity by the full width at half maximum (FWHM) of the transmission dip. The FoM of the 1D patterned

corrugated silver film is in the range of 12–23. The sensitivity of this system is comparable to other disposable SPP sensors; however, it does not require the high capital cost of nanofabrication equipment such as EBL or FIB, a cost inherent in most existing techniques. With its simplicity, low cost, and competitive sensitivity, this method is promising for disposable sensing applications.

## A.2 Experimental

The experimental setups are shown in Fig. A-1 a and b. The patterning experiment was carried out in a dark ambient environment at room temperature. Standard glass slides were cleaned with acetone, methanol, isopropyl alcohol (IPA), and DI water in ultrasonic baths for 15 min each. Then, a reusable polydimethylsiloxane (PDMS) well, with the dimensions of approximately 30 mm × 10 mm × 5 mm, was placed on top of a glass slide. Next, the glass slide with the PDMS well was placed on top of a prism. A collimated laser beam with a wavelength of 514 nm and a power of 157 mW impinged upon the bottom of the prism, and was divided into two beams by the right-angle prism (Fig. A-1 a) or four beams by the square pyramid prism (tilting angle of the facet,  $\theta_t = 45^\circ$ ) (Fig. A-1 b). The beam size was 1.5 cm in diameter, so the intensity of the laser beam was 88.8 mW/cm<sup>2</sup>. In both cases, the prisms are made of BK7 glass with a RI of 1.517, and the separated light beams interfere at an angle of 34.43°. The periodicity of the interference patterns can be calculated according to the following equation.

$$a = \lambda / (2 \sin\theta). \quad (\text{A-1})$$

The periodicity of the interference light pattern  $a$  is determined by the wavelength  $\lambda$  of the incident laser beams and the half angle  $\theta$  between two laser beams. According to this equation, the periodicities in both the 1D and 2D cases should be 572 nm.

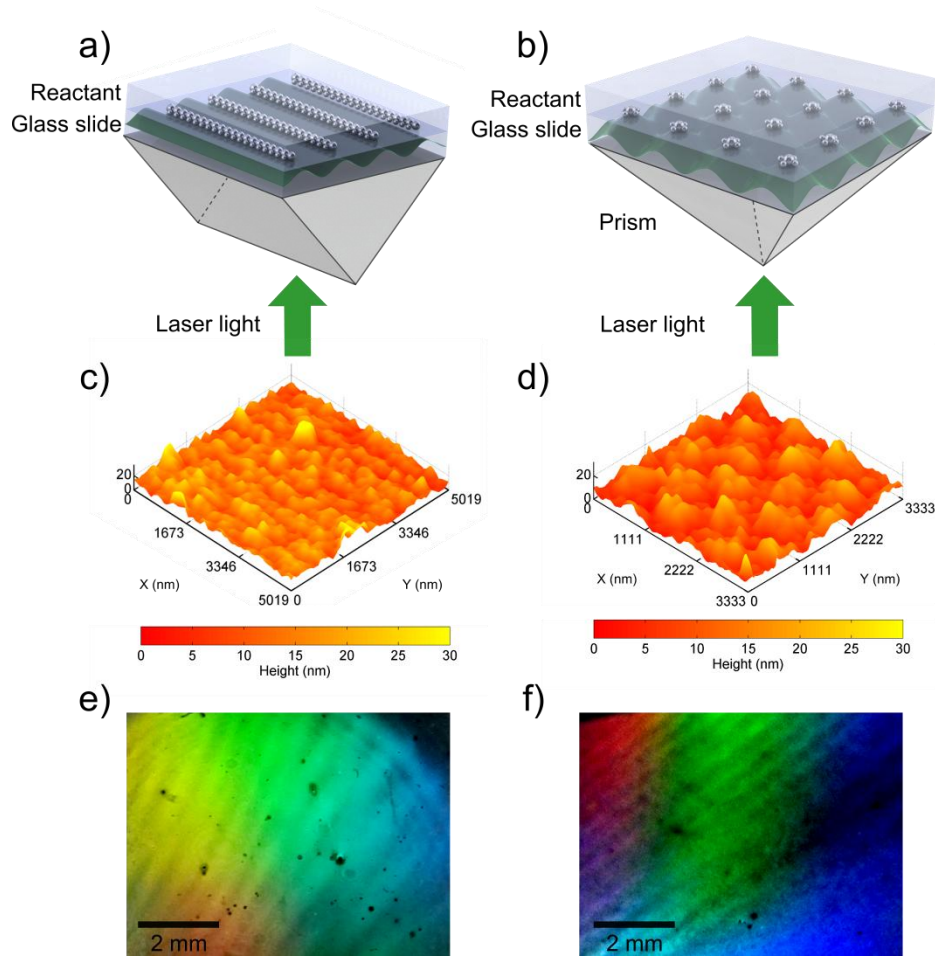


Figure A-1 Schematics of the experiment setup for fabrication of (a) 1D and (b) 2D patterned corrugated silver films. The incident laser beam from the bottom of the prism is split at the prism surface to form interference patterns on the reservoir containing  $\text{Ag}(\text{NH}_3)_2^+$  and glucose mixture. A visualization of the interference patterns are shown in the glass slides. Silver is generated faster at positions with high light intensity, resulting in a silver film with surface profile that mimics the interference pattern. (c) and (d) are the AFM images showing the surface profile of the 1D and 2D patterned corrugated silver film, respectively. Both (e) 1D and (f) 2D patterned corrugated silver films show diffraction colors under illumination with white light.

The solution containing silver-ammonia complex ions,  $\text{Ag}(\text{NH}_3)_2^+$ , was made by adding 5 mL ammonia drop-by-drop into 0.1 gram silver oxide. The reaction at this step can be described as  $\text{Ag}_2\text{O} + 4 \text{NH}_3 + \text{H}_2\text{O} \rightarrow 2 \text{Ag}(\text{NH}_3)_2^+ + 2 \text{OH}^-$ . After centrifugation, 1 mL of the purified solution was mixed with 1 mL 50% (w/v) glucose solution by vortex mixing. The mixture was then immediately injected into the PDMS well and exposed to the interference laser pattern. The exposure time was optimized to be 20 min to obtain the highest transmitted diffraction efficiency (Fig. A-2). This silver deposition method is known as the Tollens' reaction:  $\text{Ag}(\text{NH}_3)_2^+(\text{aq}) + \text{RCHO}(\text{aq}) \rightarrow \text{Ag}(\text{s}) + \text{RCOOH}(\text{aq})$ . Finally, the glass slide was removed from the prism, detached from the PDMS well, rinsed with DI water, and dried with nitrogen.

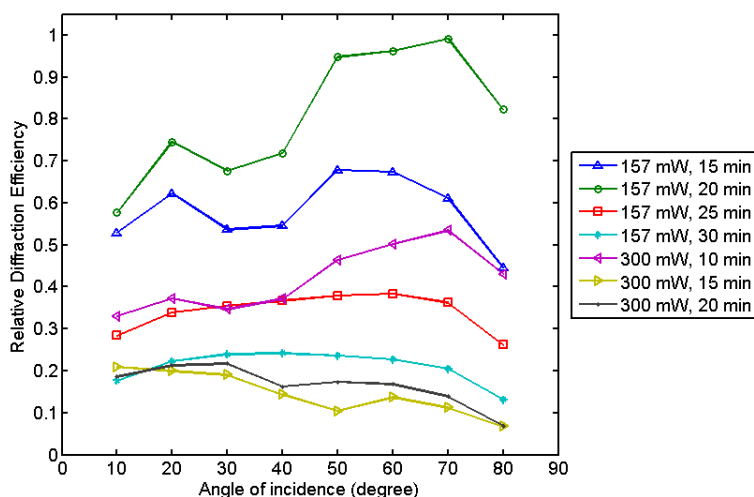


Figure A-2 The relative first-order transmitted diffraction efficiency of the one dimensional patterned corrugated silver films as a function of incident angle of a 633 nm laser. The fabrication parameters of 157 mW laser power and 20 min exposure time were chosen to maximize the diffraction efficiency.

The fabricated silver films were examined by measuring the transmission spectra. The dependence of the transmission spectra on incident angle was measured by rotating the sample slides while fixing the position of the light source and detection fiber. The RI sensitivity of the 1D pattern was evaluated by recording the transmission spectra at a normal incident angle while fluids with various RIs, such as air ( $n=1$ ), deionized (DI) water ( $n=1.333$ ), and several  $\text{CaCl}_2$  solutions at different concentrations ( $n=1.3343\text{--}1.437$ ), were subsequently sandwiched in between the sample slide and a glass slide.

### **A.3 Results and Discussion**

The surface profiles for both 1D and 2D periodic corrugated silver films were characterized by atomic force microscopy (AFM) and the results are shown in Fig. A-1 c and d. The periodicities measured by AFM (570 nm) agree well with the theoretical calculation (572 nm). The surface roughness is caused by the grain size of the silver particles during deposition. The 1D and 2D patterns have a total size of 10 mm  $\times$  8 mm and 10 mm  $\times$  10 mm, respectively.

The formation of the patterns is also indicated by the “rainbow” colors on both samples under general room lighting, as shown in Fig. A-1 e and f. The “rainbow” colors are caused by light diffracted into different directions on patterned surface. To show the diffraction color more clearly, a UV-vis light source from an optical fiber was used. As shown in Fig. A-3, the 1D pattern sample shows different color as the incident angle changes.

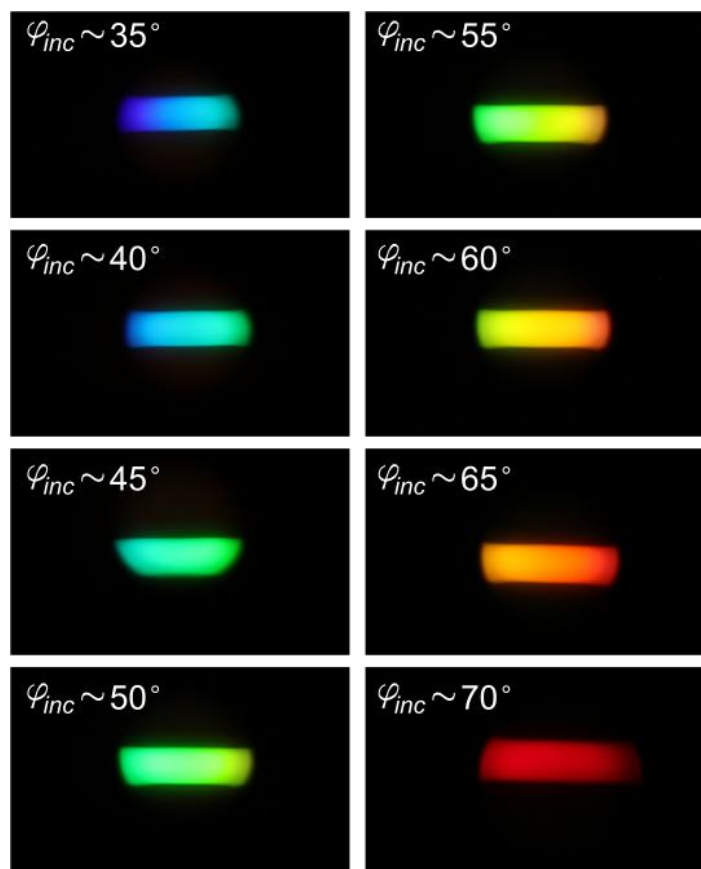


Figure A-3 The diffraction color of the one dimensional patterned corrugated silver films. Incident angle of the UV-vis light source was changed while the detection angle was fixed at around  $10^\circ$ . The wavelength of the diffraction light red-shifted as the incident angle increased.

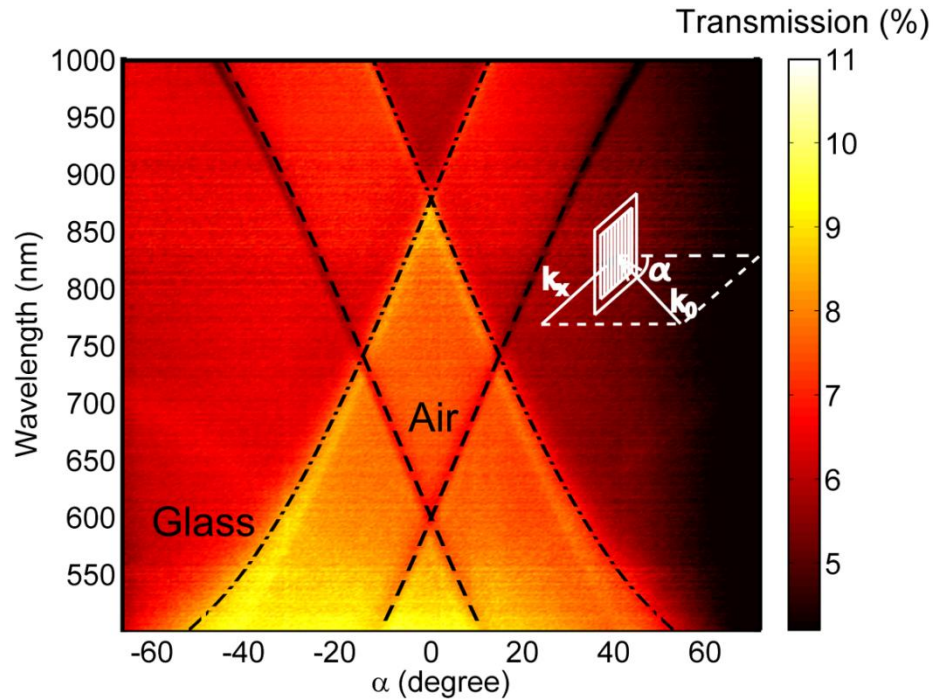


Figure A-4 Experimental transmission intensity of the 1D patterned corrugated silver film as a function of wavelength and incident angle  $\alpha$ , with theoretical calculations for the surface plasmons at silver/air interface (dashed line) and silver/glass interface (dashed dotted line). The inset shows the geometry of the experiment.

Analysis of the transmission as a function of the incident angle,  $\alpha$ , verifies that the transmission loss is consistent with the SPP theory [50]. As  $\alpha$  varies, the minimum and maximum transmission wavelengths of the 1D silver pattern change (as shown by the abrupt color changes in Fig. A-4). The patterned corrugated silver films can be considered as arrays of nanoparticle cluster, since the surface roughness is caused by the grain size of silver particles. In this case, the interparticle distance is small and near-field coupling is dominant, and the SPP wavelength will not shift with the particle size [51]. Therefore, for SPP wavelength calculations, I can model the 1D silver patterned films as 1D silver gratings without any surface roughness. A calculation based on SPP theory [50] shows that the surface plasmons excited at the silver/air interface cause minimums in the

transmission, while the surface plasmons at the silver/glass interface enhance the transmission. Surface plasmons are excited when their momentum matches the momentum of the incident photon and the grating, as follows [29]:

$$Re(k_{sp}) = k_x \pm mG_x. \quad (\text{A-2})$$

The component of the incident light's wave vector in the plane of the pattern is calculated as  $k_x = (2\pi/\lambda) \times \sin \alpha$ . The free-space wavelength of the incident light is  $\lambda$ . The expression  $G_x = 2\pi/a$  is used to calculate the grating momentum wave vector, and  $m$  is an integer [29]. The real part of the surface plasmon wave vector,  $Re(k_{sp})$ , can be expressed as [52]:

$$Re(k_{sp}) = Re \left\{ \frac{2\pi}{\lambda} \times \sqrt{\varepsilon_m \varepsilon_d / (\varepsilon_m + \varepsilon_d)} \right\}, \quad (\text{A-3})$$

with  $\varepsilon_m$  and  $\varepsilon_d$  as the dielectric constants of silver and the adjacent dielectrics ( $\varepsilon_{air} = 1$  or  $\varepsilon_{glass} = 2.3$  in this case).

At a certain incident angle, the free-space wavelength which excites surface plasmons can be theoretically calculated at silver/air ( $\varepsilon_d = \varepsilon_{air}$ ) and silver/glass ( $\varepsilon_d = \varepsilon_{glass}$ ) interfaces by using Eq. (A-2). The dashed line in Fig. A-4 is the theoretical calculation of the surface plasmons on a silver/air interface, which fits well with the minimum transmission from the experimental results. The dashed-dotted line is the calculation of the surface plasmons on silver/glass interface and it fits well with the maximum transmission.

At normal incidence, as the RI of surrounding media increases, the transmission minimum ( $\lambda_{res}$ ) red-shifts, while the transmission maximum ( $\lambda_{res,glass}$ ) remains unchanged,

as shown in Fig. A-5 a. This is expected because the fluid in contact with the silver film is altered while the glass remains the same. A linear function,  $\lambda_{res} = 553.4 n + 56.43$ , is used to fit the experimental results by using a least-squares regression. The slope, 553.4 nm/RIU, can be taken as the sensitivity factor. This value is comparable to sensors fabricated by FIB milling (400 nm/RIU) [53] and much better than the substrates prepared by NSL (150 nm/RIU) [30].

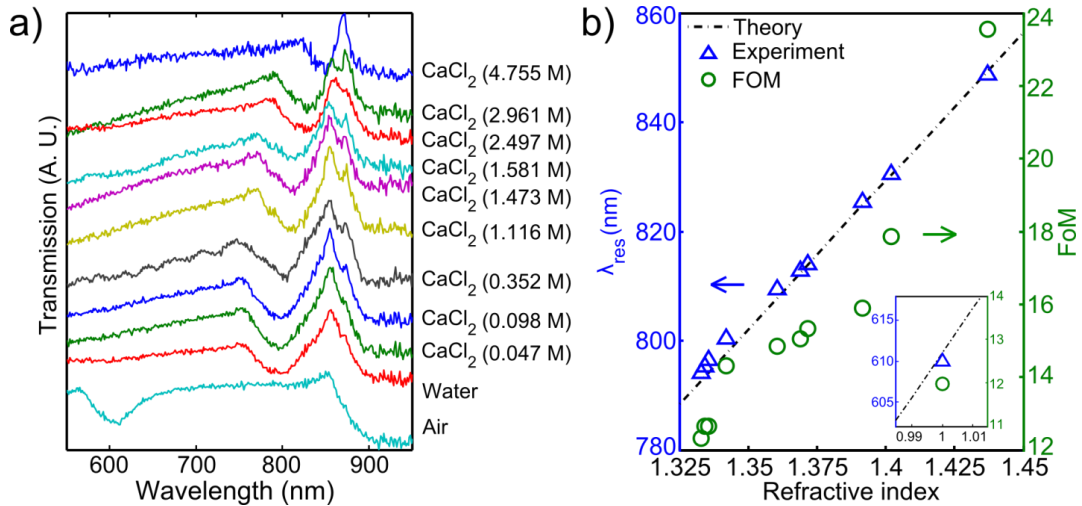


Figure A-5 (a) At normal incidence, the transmission spectra of the 1D patterned corrugate silver film immersed into air, DI water, and several solutions of CaCl<sub>2</sub> at different concentrations. The spectra have been displaced along the ordinate for clarity and corresponding materials information is indicated by the side of each curve. (b) Dependence of the lowest transmission wavelength and the RI of surrounding materials and the figure of merit (FoM) calculated from (a). The inset shows the data point when the surrounding material is air.

The linear relationship between  $\lambda_{res}$  and  $n$  can be predicted using SPP theory as expressed in Eq. (A-2) and (A-3), with the assumption that  $\epsilon = n^2$  for the fluid in contact with the silver film. This relationship is shown as the dashed line in Fig. A-6 b and the theoretical sensitivity (slope) is 573 nm/RIU. As discussed,  $\lambda_{res,glass}$  remains constant. The

calculated wavelength of  $\lambda_{res, glass}$  using  $\epsilon_{glass} = 2.3$  is 887 nm, and the experimental value ranges from 860 to 870 nm. The differences between the theoretical prediction and the experimental results could be caused by the uncertainty in the experimental incident light angle and/or tarnishing of silver due to the presence of atmospheric sulphur [54]. As the RI of surrounding material becomes close to the RI of glass slide,  $\lambda_{res}$  approaches  $\lambda_{res, glass}$ , making the dip narrower. Therefore, the FoM increases with the increase of RI, as shown in Fig. A-6 b.

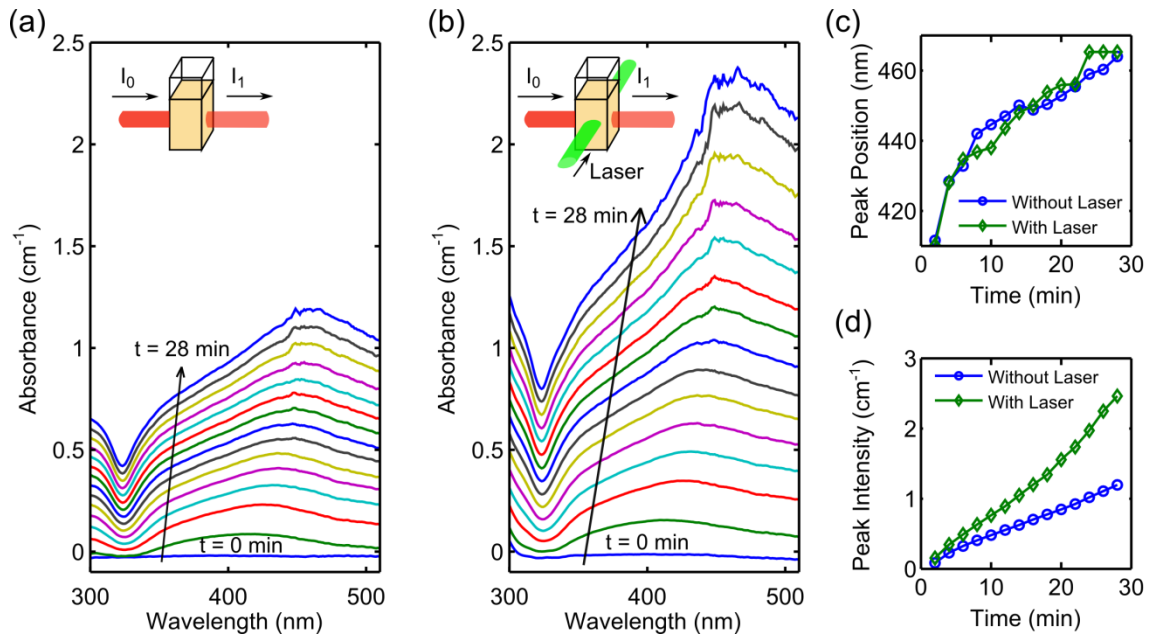


Figure A-6 The absorbance of the mixture of  $Ag(NH_3)_2^+$  and glucose solution (a) without and (b) with 514 nm laser exposure. The insets show the schematic of the experimental setup. (c) The peak position and (d) the peak intensity of the absorbance of the mixture as a function of time without and with laser exposure. The data of (c) and (d) are extracted from (a) and (b).

The pattern formation should mainly be attributed to the photo-enhanced chemical reaction [55–57]. To confirm this hypothesis, a control experiment was carried out. In the

control experiment, the absorbance spectra of the reaction between  $\text{Ag}(\text{NH}_3)_2^+$  and glucose was measured in real-time with and without laser exposure, as shown in Fig. A-6 a and b. A peak in the absorbance spectra and continuous red-shift of that peak indicates the nucleation and growth of silver nanoparticles, respectively, owing to the localized surface plasmon resonances (LSPR) of the nanoparticles [30,58]. Fig. A-6 c and d show the peak position and intensity as a function of time with and without laser exposure. In Fig. A-6 c, there is no significant difference in the peak positions with or without laser exposure, indicating that the laser irradiation does not affect the nanoparticles' shape or size during the growing process. However, the absorbance peak value of the sample under laser exposure grows much faster than that without laser exposure (Fig. A-6 d). Therefore, when the  $\text{Ag}(\text{NH}_3)_2^+$  and glucose mixture is subjected to holographic exposure, the rate of silver nanoparticle formation is much faster in the regions of high light intensity, thus a pattern is formed in accordance with the interference pattern of the light.

Studies that examine photo-induced silver deposition in liquid phase are generally based on two main mechanisms: photoreduction [59,60] and thermally induced decomposition [48,55,59]. Usually, pure photoreduction of silver occurs only under UV irradiation [55], while thermally induced decomposition takes place in the presence of significantly elevated temperatures ( $>80\text{ }^\circ\text{C}$ ) [48]. In this case, however, the incident photons at 514 nm do not have sufficient energy to break the chemical bonds in  $\text{Ag}(\text{NH}_3)_2^+$ , and the low laser intensity ( $88.8\text{ mW/cm}^2$ ) cannot produce discernible increase in the bulk fluid temperature. Therefore, I explain the enhancement in silver

production in a different way. In this experiment, small silver nanoparticles are first nucleated based on the Tollens' reaction. Afterwards, the rise in local temperature due to the light-to-heat conversion related to LSPR [61–65] induces decomposition of  $\text{Ag}(\text{NH}_3)_2^+$  [57], increasing the reaction rate in the immediate vicinity of the silver particles [66]. As a result, with laser exposure, LSPRs can significantly enhance the photochemical reaction, leading to a significant increase in nanoparticle nucleation [55,56].

#### **A.4 Conclusion**

Here, a simple and cost-effective method to holographically fabricate 1D and 2D patterned corrugated silver films over large areas is demonstrated. The fabrication consists of a single-step process and only requires laser with power density as low as  $88.8 \text{ mW/cm}^2$ . The silver films have high sensitivities ( $553.4 \text{ nm/RIU}$ ) to their surroundings' refractive indices, which makes them promising for disposable chemical/biological sensing applications. By simply confining the reagents within microfluidic channel, the silver films can be easily integrated into microfluidic devices as on-chip sensors, which may contribute to microfluidic reactors with feedback systems.

## References

- [1] Lu, D., Kan, J., Fullerton, E.E. and Liu, Z., "*Tunable surface plasmon polaritons in Ag composite films by adding dielectrics or semiconductors*," Applied Physics Letters, **98**, 243114 (2011)
- [2] Homola, J., "*Surface plasmon resonance sensors for detection of chemical and biological species*," Chemical Reviews, **108**, 462–493 (2008)
- [3] Liu, Y.J., Hao, Q., Smalley, J.S.T., Liou, J., Khoo, I.C. and Huang, T.J., "*A frequency-addressed plasmonic switch based on dual-frequency liquid crystals*," Applied Physics Letters, **97**, 091101 (2010)
- [4] Homola, J., Yee, S.S. and Gauglitz, G., "*Surface plasmon resonance sensors: review*," Sensor Actual. B: Chemical, **54**, 3–15 (1999)
- [5] Yao, J., Le, A.-P., Gray, S.K., Moore, J.S., Rogers, J.A. and Nuzzo, R.G., "*Functional nanostructured plasmonic materials*," Advanced Materials, **22**, 1102–1110 (2010)
- [6] Stewart, M.E., Anderton, C.R., Thompson, L.B., Maria, J., Gray, S.K., Rogers, J.A. and Nuzzo, R.G., "*Nanostructured plasmonic sensors*," Chemical Reviews, **108**, 494–521 (2008)
- [7] Sun, C., Su, K.-H., Valentine, J., Rosa-Bauza, Y.T., Ellman, J. a, Elboudwarej, O., Mukherjee, B., Craik, C.S., Shuman, M. a, Chen, F.F. and Zhang, X., "*Time-resolved single-step protease activity quantification using nanoplasmonic resonator sensors*," ACS Nano, **4**, 978–984 (2010)
- [8] Li, D., Paxton, W.F., Baughman, R.H., Huang, T.J., Stoddart, J.F. and Weiss, P.S., "*Molecular, supra molecular, and macromolecular motors and artificial muscles*," MRS Bulletin, **34**, 671–681 (2009)
- [9] Mao, X. and Huang, T.J., "*Microfluidic diagnostics for the developing world*," Lab on a Chip, **12**, 1412–1416 (2012)
- [10] Shi, J., Mao, X., Ahmed, D., Colletti, A. and Huang, T.J., "*Focusing microparticles in a microfluidic channel with standing surface acoustic waves (SSAW)*," Lab on a Chip, **8**, 221–223 (2008)
- [11] Shi, J., Ahmed, D., Mao, X., Lin, S.-C.S., Lawit, A. and Huang, T.J., "*Acoustic tweezers: patterning cells and microparticles using standing surface acoustic waves (SSAW)*," Lab on a Chip, **9**, 2890–2895 (2009)

- [12] Mao, X., Juluri, B.K., Lapsley, M.I., Stratton, Z.S. and Huang, T.J., "*Milliseconds microfluidic chaotic bubble mixer*," *Microfluidics and Nanofluidics*, **8**, 139–144 (2010)
- [13] Shi, J., Yazdi, S., Lin, S.-C.S., Ding, X., Chiang, I.-K., Sharp, K. and Huang, T.J., "*Three-dimensional continuous particle focusing in a microfluidic channel via standing surface acoustic waves (SSAW)*," *Lab on a Chip*, **11**, 2319–2324 (2011)
- [14] Brennan, D., Justice, J., Corbett, B., McCarthy, T. and Galvin, P., "*Emerging optofluidic technologies for point-of-care genetic analysis systems: a review*," *Analytical and Bioanalytical Chemistry*, **395**, 621–636 (2009)
- [15] Piliarik, M., Vala, M., Tichý, I. and Homola, J., "*Compact and low-cost biosensor based on novel approach to spectroscopy of surface plasmons*," *Biosensors and Bioelectronics*, **24**, 3430–3435 (2009)
- [16] Kwon, M.-S., "*Disposable and compact integrated plasmonic sensor using a long-period grating*," *Optics Letters*, **35**, 3835–3837 (2010)
- [17] Nakamoto, K., Kurita, R., Niwa, O., Fujii, T. and Nishida, M., "*Development of a mass-producible on-chip plasmonic nanohole array biosensor*," *Nanoscale*, **3**, 5067–5075 (2011)
- [18] Kretschmann, E. and Raether, H., "*Radiative decay of non radiative surface plasmons excited by light (surface plasma waves excitation by light and decay into photons applied to nonradiative modes)*," *Zeitschrift für Naturforschung A*, **23**, 2135 (1968)
- [19] Turbadar, T., "*Complete absorption of plane polarized light by thin metallic films*," *Optica Acta: International Journal of Optics*, **11**, 207–210 (1964)
- [20] Turbadar, T., "*Complete absorption of light by thin metal films*," *Proceedings of the Physical Society*, **73**, 40–44 (1958)
- [21] Goldenberg, L.M., Sakhno, O. V., Smirnova, T.N., Helliwell, P., Chechik, V. and Stumpe, J., "*Holographic composites with gold nanoparticles: nanoparticles promote polymer segregation*," *Chemistry of Materials*, **20**, 4619–4627 (2008)
- [22] Zhang, X., Liu, H. and Feng, S., "*Solution-processible fabrication of large-area patterned and unpatterned gold nanostructures*," *Nanotechnology*, **20**, 425303 (2009)

- [23] Zhang, X., Liu, H., Tian, J., Song, Y., Wang, L., Song, J. and Zhang, G., "*Optical polarizers based on gold nanowires fabricated using colloidal gold nanoparticles*," *Nanotechnology*, **19**, 285202 (2008)
- [24] Liu, Z., Wang, Y., Yao, J., Lee, H., Srituravanich, W. and Zhang, X., "*Broad band two-dimensional manipulation of surface plasmons*," *Nano Letters*, **9**, 462–466 (2009)
- [25] Feng, L., Liu, Z. and Fainman, Y., "*Direct observation of plasmonic index ellipsoids on a deep-subwavelength metallic grating*," *Applied Optics*, **50**, G1–G6 (2011)
- [26] Galush, W.J., Shelby, S. a, Mulvihill, M.J., Tao, A., Yang, P. and Groves, J.T., "*A nanocube plasmonic sensor for molecular binding on membrane surfaces*," *Nano Letters*, **9**, 2077–2082 (2009)
- [27] Wang, S., Pile, D.F.P., Sun, C. and Zhang, X., "*Nanopin plasmonic resonator array and its optical properties*," *Nano Letters*, **7**, 1076–1080 (2007)
- [28] Hao, Q., Zeng, Y., Wang, X., Zhao, Y., Wang, B., Chiang, I.-K., Werner, D.H., Crespi, V. and Huang, T.J., "*Characterization of complementary patterned metallic membranes produced simultaneously by a dual fabrication process*," *Applied Physics Letters*, **97**, 193101 (2010)
- [29] Ebbesen, T.W., Lezec, H.J., Ghaemi, H.F., Thio, T. and Wolff, P.A., "*Extraordinary optical transmission through sub-wavelength hole arrays*," *Nature*, **391**, 667–669 (1998)
- [30] Zheng, Y.B., Juluri, B.K., Mao, X., Walker, T.R. and Huang, T.J., "*Systematic investigation of localized surface plasmon resonance of long-range ordered Au nanodisk arrays*," *Journal of Applied Physcis*, **103**, 014308 (2008)
- [31] Guo, L.J., "*Nanoimprint lithography: methods and material requirements*," *Advanced Materials*, **19**, 495–513 (2007)
- [32] Childs, W.R. and Nuzzo, R.G., "*Large-area patterning of coinage-metal thin films using decal transfer lithography*," *Langmuir*, **21**, 195–202 (2005)
- [33] Yu, C.-C., Ho, K.-H., Chen, H.-L., Chuang, S.-Y., Tseng, S.-C. and Su, W.-F., "*Using the nanoimprint-in-metal method to prepare corrugated metal structures for plasmonic biosensors through both surface plasmon resonance and index-matching effects*," *Biosensors and Bioelectronics*, **33**, 267–273 (2012)

- [34] Ko, S.H., Park, I., Pan, H., Grigoropoulos, C.P., Pisano, A.P., Luscombe, C.K. and Fréchet, J.M.J., "*Direct nanoimprinting of metal nanoparticles for nanoscale electronics fabrication*," *Nano Letters*, **7**, 1869–1877 (2007)
- [35] Chen, H.L., Chuang, S.Y., Cheng, H.C., Lin, C.H. and Chu, T.C., "*Directly patterning metal films by nanoimprint lithography with low-temperature and low-pressure*," *Microelectronic Engineering*, **83**, 893–896 (2006)
- [36] Zhu, X., Liang, G., Xu, Y., Cheng, S. and Yang, S., "*Fabrication of size scalable three-dimensional photonic structures via dual-beam multiple exposure and its robustness study*," *Journal of the Optical Society of America B*, **27**, 2534–2541 (2010)
- [37] Zhang, X., Sun, B., Friend, R.H., Guo, H., Nau, D. and Giessen, H., "*Metallic photonic crystals based on solution-processible gold nanoparticles*," *Nano Letters*, **6**, 651–655 (2006)
- [38] Mao, W., Wathuthanthri, I. and Choi, C.-H., "*Tunable two-mirror interference lithography system for wafer-scale nanopatterning*," *Optics Letters*, **36**, 3176–3178 (2011)
- [39] Du, K., Wathuthanthri, I., Mao, W., Xu, W. and Choi, C.-H., "*Large-area pattern transfer of metallic nanostructures on glass substrates via interference lithography*," *Nanotechnology*, **22**, 285306 (2011)
- [40] Moon, J.H., Seo, J.S., Xu, Y. and Yang, S., "*Direct fabrication of 3D silica-like microstructures from epoxy-functionalized polyhedral oligomeric silsesquioxane (POSS)*," *Journal of Materials Chemistry*, **19**, 4687–4691 (2009)
- [41] Miyake, M., Chen, Y.-C., Braun, P. V. and Wiltzius, P., "*Fabrication of three-dimensional photonic crystals using multibeam interference lithography and electrodeposition*," *Advanced Materials*, **21**, 3012–3015 (2009)
- [42] Liang, G., Zhu, X., Xu, Y., Li, J. and Yang, S., "*Holographic design and fabrication of diamond symmetry photonic crystals via dual-beam quadruple exposure*," *Advanced Materials*, **22**, 4524–4529 (2010)
- [43] Choi, C.-H. and Kim, C.-J., "*Fabrication of a dense array of tall nanostructures over a large sample area with sidewall profile and tip sharpness control*," *Nanotechnology*, **17**, 5326–5333 (2006)
- [44] Li, J., Liang, G., Zhu, X. and Yang, S., "*Exploiting nanoroughness on holographically patterned three-dimensional photonic crystals*," *Advanced Functional Materials*, **22**, 2980–2986 (2012)

- [45] Nakata, Y., Okada, T. and Maeda, M., "*Fabrication of dot matrix, comb, and nanowire structures using laser ablation by interfered femtosecond laser beams,*" Applied Physics Letters, **81**, 4239 (2002)
- [46] Lasagni, A., Dalessandria, M., Giovanelli, R. and Mucklich, F., "*Advanced design of periodical architectures in bulk metals by means of Laser Interference Metallurgy,*" Applied Surface Science, **254**, 930–936 (2007)
- [47] Shin, H., Yoo, H. and Lee, M., "*Fabrication of Au thin film gratings by pulsed laser interference,*" Applied Surface Science, **256**, 2944–2947 (2010)
- [48] Lachish-Zalait, A., Zbaida, D., Klein, E. and Elbaum, M., "*Direct surface patterning from solutions: localized microchemistry using a focused laser,*" Advanced Functional Materials, **11**, 218–223 (2001)
- [49] Kaneko, S., Ito, T., Yasui, M., Kato, C., Tanaka, S., Ozawa, T., Hirabayashi, Y., Matsuno, A., Nire, T. and Yoshimoto, M., "*Periodic nano trench structure fabricated by high-speed scanning CW laser,*" Proceedings of the SPIE: Laser Applications in Microelectronic and Optoelectronic Manufacturing (LAMOM) XVII, **8243**, 82430U (2012)
- [50] Vengurlekar, A.S., "*Extraordinary optical transmission through metal films with subwavelength holes and slits,*" Current Science, **98**, 1020–1032 (2010)
- [51] Yang, L., Yan, B., Premasiri, W.R., Ziegler, L.D., Negro, L.D. and Reinhard, B.M., "*Engineering nanoparticle cluster arrays for bacterial biosensing: the role of the building block in multiscale SERS substrates,*" Advanced Functional Materials, **20**, 2619–2628 (2010)
- [52] Wang, Y., Srituravanich, W., Sun, C. and Zhang, X., "*Plasmonic nearfield scanning probe with high transmission,*" Nano Letters, **8**, 3041–3045 (2008)
- [53] Brolo, A.G., Gordon, R., Leathem, B. and Kavanagh, K.L., "*Surface plasmon sensor based on the enhanced light transmission through arrays of nanoholes in gold films,*" Langmuir, **20**, 4813–4815 (2004)
- [54] Mehfuz, R., Maqsood, M.W. and Chau, K.J., "*Enhancing the efficiency of slit-coupling to surface-plasmon-polaritons via dispersion engineering,*" Optics Express, **18**, 18206–18216 (2010)
- [55] Maillard, M., Huang, P. and Brus, L., "*Silver nanodisk growth by surface plasmon enhanced photoreduction of adsorbed  $[Ag^+]$ ,*" Nano Letters, **3**, 1611–1615 (2003)

- [56] Rycenga, M., Cobley, C.M., Zeng, J., Li, W., Moran, C.H., Zhang, Q., Qin, D. and Xia, Y., "Controlling the synthesis and assembly of silver nanostructures for plasmonic applications," *Chemical Reviews*, **111**, 3669–3712 (2011)
- [57] Cao, L., Barsic, D.N., Guichard, A.R. and Brongersma, M.L., "Plasmon-assisted local temperature control to pattern individual semiconductor nanowires and carbon nanotubes," *Nano Letters*, **7**, 3523–3527 (2007)
- [58] Juluri, B.K., Zheng, Y.B., Ahmed, D., Jensen, L. and Huang, T.J., "Effects of geometry and composition on charge-induced plasmonic shifts in gold," *Journal of Physical Chemistry C*, **112**, 7309–7317 (2008)
- [59] Smirnova, T.N., Kokhtych, L.M., Kutsenko, A.S., Sakhno, O. V and Stumpe, J., "The fabrication of periodic polymer/silver nanoparticle structures: in situ reduction of silver nanoparticles from precursor spatially distributed in polymer using holographic exposure," *Nanotechnology*, **20**, 405301 (2009)
- [60] Jin, R., Cao, Y., Mirkin, C. a, Kelly, K.L., Schatz, G.C. and Zheng, J.G., "Photoinduced conversion of silver nanospheres to nanoprisms," *Science*, **294**, 1901–1903 (2001)
- [61] Akchurin, G., Khlebtsov, B., Akchurin, G., Tuchin, V., Zharov, V. and Khlebtsov, N., "Gold nanoshell photomodification under a single-nanosecond laser pulse accompanied by color-shifting and bubble formation phenomena," *Nanotechnology*, **19**, 015701 (2008)
- [62] Richardson, H.H., Hickman, Z.N., Govorov, A.O., Thomas, A.C., Zhang, W. and Kordesch, M.E., "Thermooptical properties of gold nanoparticles embedded in ice: characterization of heat generation and melting," *Nano Letters*, **6**, 783–788 (2006)
- [63] An, W., Zhu, Q., Zhu, T. and Gao, N., "Radiative properties of gold nanorod solutions and its temperature distribution under laser irradiation: experimental investigation," *Experimental Thermal and Fluid Science*, **44**, 409–418 (2013)
- [64] Rycenga, M., Wang, Z., Gordon, E., Cobley, C.M., Schwartz, A.G., Lo, C.S. and Xia, Y., "Probing the photothermal effect of gold-based nanocages with surface-enhanced Raman scattering (SERS)," *Angewandte Chemie*, **48**, 9924–9927 (2009)
- [65] Baffou, G., Kreuzer, M.P., Kulzer, F. and Quidant, R., "Temperature mapping near plasmonic nanostructures using fluorescence polarization anisotropy," *Optics Express*, **17**, 3291–3298 (2009)

- [66] Cobley, C.M., Chen, J., Cho, E.C., Wang, L. V and Xia, Y., "*Gold nanostructures: a class of multifunctional materials for biomedical applications.*", *Chemical Society Reviews*, **40**, 44–56 (2011)

**VITA**  
**Mengqian Lu**

Mengqian Lu was born on February 24, 1986 in Jiangsu, China. She received her Bachelor in Theoretical and Applied Mechanics and Bachelor in Economics from Peking University in China in 2008.

Mengqian joined the Department of Engineering Science and Mechanics at Pennsylvania State University as a Ph. D. student in August 2008. She was advised by Professor Tony Jun Huang. The following is her list of journal publications.

- [1] Lu, M., Ho, Y.-P., Grigsby, C.L. Nawaz, A.A. Nawaz, Leong, K.W. and Huang, T.J., “*A three-dimensional hydrodynamic focusing method for polyplexes synthesis*,” ACS Nano, **8**, 332-339 (2014)
- [2] Si, G., Zhao, Y., Lv, J., Lu, M. Lu, Wang, F., Liu, H., Xiang, N., Huang, T.J., Danner, A.J., Teng, J. and Liu, Y. J., “*Reflective plasmonic color filters based on lithographically patterned silver nanorod arrays*,” Nanoscale, **5**, 6243-6248 (2013)
- [3] Xie, Y., Ahmed, D., Lapsley, M.I., Lu, M., Li, S. and Huang, T.J., “*Acoustofluidic relay: sequential trapping and transporting of microparticles via acoustically excited oscillating bubbles*,” Journal of Laboratory Automation, **19**, 137-143 (2013)
- [4] Liu, Y.J., Lu, M., Ding, X., Leong, E.S.P., Lin, S.-C.S., Shi, J., Teng, J.H., Wang, L., Bunning, T.J. and Huang, T.J., “*Holographically formed, acoustically switchable gratings based on polymer-dispersed liquid crystals*,” Journal of Laboratory Automation, **18**, 291-295 (2013)
- [5] Lu, M., Juluri, B.K., Liu, Y.J., Bunning, T.J. and Huang, T.J., “*Single-step holographic fabrication of large-area periodically corrugated metal films*,” Journal of Applied Physics, **112**, 113101 (2012)
- [6] Yang, S., Guo, F., Kiraly, B., Mao, X., Lu, M. and Huang, T.J., “*Microfluidic synthesis of multifunctional janus particles for biomedical applications*,” Lab On a Chip, **12**, 2097-2102 (2012)
- [7] Zhao, Y., Hao, Q., Ma, Y., Lu, M., Zhang, B., Lapsley, M., Khoo, I.-C. and Huang, T. J., “*Light-driven tunable dual-band plasmonic absorber using liquid-crystal-coated asymmetric nanodisk array*,” Applied Physics Letters, **100**, 053119 (2012)
- [8] Lapsley, M.I., Shahravan, A., Hao, Q., Juluri, B. K., Giardinelli, S., Lu, M., Zhao, Y., Chiang, I.-K., Matsoukas, T. and Huang, T.J., “*Shifts in plasmon resonance due to charging of a nanodisk array in argon plasma*,” Applied Physics Letters, **100**, 101903 (2012)
- [9] Juluri, B.K., Chatuvedi, N., Hao, Q., Lu, M., Velego, D., Jensen, L. and Huang, T.J., “*Scalable manufacturing of plasmonic nanodisk dimers and cusp nanostructures using salting-out quenching method and colloidal lithography*,” ACS Nano, **5**, 5838-5847 (2011)
- [10] Lu, M., Juluri, B.K., Lin, S.-C.S. and Huang, T.J., “*Aperture modification and beam deflection using parabolic gradient-index photonic crystals*,” Journal of Applied Physics, **108**, 103505 (2010)
- [11] Shi, J., Juluri, B.K., Lin, S.-C.S., Lu, M. and Huang, T.J., “*Photonic crystal composites-based wide-band optical collimator*,” Journal of Applied Physics, **108**, 043514 (2010)
- [12] Zheng, Y.B., Juluri, B.K., Jensen, L.L., Ahmed, D., Lu, M., Jensen, L. and Huang, T.J., “*Dynamically tuning plasmon-exciton coupling in arrays of nanodisk-J-aggregate complexes*,” Advanced Materials, **22**, 3603-3607 (2010)
- [13] Juluri, B.K., Lu, M., Zheng, Y.B., Jensen, L. and Huang, T.J., “*Coupling between molecular and plasmonic resonances: effect of molecular absorbance*,” Journal of Physical Chemistry C, **113**, 18499 (2009)